

Doctoral Dissertation

博士論文

Effects of Replicated N-body Simulation Boxes in Simulating Weak Lensing Observables

弱重力レンズ統計量の模擬データ生成における
有限体積のN体シミュレーションの影響の研究

A Dissertation Submitted for the Degree of Doctor of Philosophy

December 2024

令和6年12月博士（理学）申請

Department of Physics, Graduate School of Science,

The University of Tokyo

東京大学大学院理学系研究科
物理学専攻

Akira Tokiwa

常盤 晟

Contents

1	Introduction	1
1.1	Historical Overview	1
1.2	Astronomical Surveys and Observations	2
1.3	Constraint from Weak Lensing	4
1.4	Aim of this Thesis	6
1.5	Structure of the Thesis	7
2	Cosmology	9
2.1	Einstein Field Equations	9
2.2	FLRW Metric and the Friedmann Equations	11
2.3	Cosmological Distances	14
2.3.1	Luminosity Distance	14
2.3.2	Angular Diameter Distance	15
2.4	Initial Conditions	15
2.4.1	Primordial Power Spectrum	15
2.4.2	Baryon Acoustic Oscillations	17
2.5	The linear evolution of density fluctuations	18
2.6	Spherical Collapse	20
2.7	Dark Matter Halo	22
2.7.1	Halo Mass Function	22
2.7.2	Halo Bias	23
2.7.3	Halo Density Profile	24
3	Weak Lensing	25
3.1	Lens Equation	25
3.1.1	Derivation	25
3.1.2	Lensing Matrix	27
3.2	Convergence	29
3.2.1	Definition	29

3.2.2	Convergence from Density Contrast	29
3.3	Shear	30
3.3.1	Definition	30
3.3.2	E-mode and B-mode	30
3.4	Estimation of Lensing Fields	31
3.4.1	Ellipticity and Reduced Shear	31
3.4.2	From Shear to Convergence	32
4	Statistics	34
4.1	Convergence Power Spectrum	34
4.1.1	Halofit Model	36
4.2	Convergence Bispectrum	37
4.2.1	BiHalofit Model	37
4.3	Probability Density Functions	38
4.3.1	hmpdf Model	39
4.4	Peak and Minimum Counts	39
4.5	Minkowski Functionals	41
5	Covariance	43
5.1	Role of the Covariance Matrix	43
5.2	Covariance of the Matter Power Spectrum	45
5.3	Covariance of the Angular Power Spectrum	46
5.4	Covariance of Higher-Order Statistics	48
6	Simulations	49
6.1	Initial Condition Generation	50
6.1.1	Initial Density Field	50
6.1.2	Initial Displacement Field	51
6.1.3	Initial Velocities	51
6.2	Simulation Basics	52
6.2.1	Direct Summation	52
6.2.2	Particle-Mesh (PM) Method	52
6.2.3	Particle-Particle Particle-Mesh (P3M) Method	53
6.2.4	Tree-Particle-Mesh (Tree-PM) Method	53
6.3	Tools for Fast Computation	54
6.3.1	Fast Fourier Transform	54
6.3.2	Mass Assignment Schemes	54

6.3.3	Parallelization Techniques	55
6.3.4	Adaptive Mesh Refinement	56
6.3.5	Tree Construction	56
6.4	FASTPM	57
6.4.1	Modified Kick and Drift Factors	57
6.4.2	Algorithm Steps	59
6.5	Weak Lensing Map Generation	59
6.5.1	Conventional Ray-Tracing Algorithm	60
6.5.2	Born-approximated Ray-tracing	61
7	Methods	63
7.1	N-body Simulations	63
7.2	Generating Convergence Maps	66
7.3	Incorporating Noise	66
7.4	Patch Extraction for Analysis	67
7.5	Gaussian Smoothing	69
7.6	Measurements	70
7.6.1	Angular Power Spectrum	71
7.6.2	Bispectrum	72
7.6.3	PDF	72
7.6.4	Peak/Mimima Counts	72
7.6.5	Minkowski Functionals	72
7.6.6	Covariance Matrix Estimation	73
8	Results	75
8.1	Overview	75
8.2	Effects of Noise	76
8.3	Effects of Smoothing Scale	76
9	Discussion	90
9.1	Source of Systematics	90
9.1.1	Box Replication Effect	90
9.2	flat-sky vs. full-sky	91
10	Conclusions and Future Work	93

List of Figures

2.1	Angular Power Spectrum of Cosmic Microwave Background Temperature Fluctuations as a function of the multipole moment (ℓ) and the corresponding angular scale. The observational data are depicted by red markers with associated error bars, whereas the theoretical prediction derived from the Λ CDM cosmological model is represented by the green curve (Planck Collaboration et al., 2014). The primordial fluctuations imprinted at large angular scales ($\ell \lesssim 30$).	16
2.2	The linear matter power spectrum as a function of the wavenumber k computed using the CLASS code. The transition from the radiation-dominated to the matter-dominated era is evident around $k_{\text{eq}} = 0.0104 h/\text{Mpc}$ (Planck Collaboration et al., 2020). . . .	17
3.1	Schematic representation of the lensing geometry. The source is located at β , while the observed image is at θ . The deflection angle α is the difference between the observed and true angular positions.	27
3.2	Illustration of the distortion of background sources due to gravitational lensing. The left panel depict the effect of the convergence κ and the middle and right panels show the components of the shear $\gamma = \gamma_1 + i\gamma_2$ on circular background sources. Positive and negative values of κ cause isotropic magnification or demagnification, while γ_1 and γ_2 introduce anisotropic distortions, stretching the sources along or at an angle to the principal axes.	28
4.1	Identification of peaks and minima in a smoothed convergence map. The left panel shows the smoothed convergence field $\kappa_{\text{smooth}}(\hat{\mathbf{n}})$ with peaks (red circles) satisfying the peak condition (Equation (4.27)), and the right panel highlights the minima (blue circles) satisfying the minimum condition (Equation (4.28)).	40
4.2	Excursion sets $\Sigma(\nu) = \{\kappa > \nu\sigma_0\}$ for increasing thresholds ($\nu = 0.5, 1, 1.5, 2$). Black regions indicate areas where κ exceeds $\nu\sigma_0$, showing reduced size and connectivity as ν increases.	41

6.1	Evolution of the number of particles used in N -body simulations as a function of the year of publication (Leclercq, 2020). The symbols and colors indicate the gravitational solver employed: P ³ M and adaptive P ³ M (AP ³ M); parallel or vectorized P ³ M; Tree codes; TreePM; and particle-mesh methods with adaptive mesh refinement (PM AMR). Hydrodynamic simulations are represented by black squares.	50
6.2	Illustration of three mass assignment schemes—Nearest Grid Point (NGP), Cloud-In-Cell (CIC), and Triangular-Shaped Cloud (TSC)—used to map a particle’s mass onto a 1D grid.	55
6.3	Illustration of adaptive mesh refinement (AMR) applied to a 2D image with two Gaussian kernels. The left panel shows the initial coarse grid structure over the image. The middle and right panels demonstrate progressively finer levels of mesh refinement in regions of higher intensity, where the Gaussian kernels are located. The red grid outlines indicate the adaptively refined mesh hierarchy, ensuring higher resolution where needed while maintaining computational efficiency in lower-intensity regions.	56
6.4	Illustration of an Octree decomposition for a 3D volume containing four particles. The left panel showcases the spatial subdivision of the volume into hierarchical grid cells, with color-coding indicating different levels of refinement. The right panel presents the corresponding Octree data structure, highlighting the hierarchical relationships between nodes. Credit by Powell et al. (2023)	57
7.1	Spatial and redshift setup for the BIGBOX and TILED simulations. Dashed blue grids partition the overall simulation volume into smaller, manageable tiling regions where each tile is a replication of the TILED simulation. The lower horizontal axis represents the line-of-sight distance measured in Mpc/ h , with the corresponding redshift values displayed on the top axis.	64
7.2	Illustration of a 5×5 patch around $(\theta, \phi) = (\pi/2, 0)$ extracted from the TILED and BIGBOX simulations. The TILED simulation exhibits a distinct Kaleidoscope pattern due to box replication, resulting in heavily tiled regions along the line of sight and near the equator.	65
7.3	Normalized lensing efficiency as a function of comoving distance for multiple source redshifts. The lensing efficiency peaks at intermediate comoving distances, indicating regions where the distribution of matter enhances the gravitational lensing signal.	66
7.4	Convergence maps generated from the BIGBOX and TILED simulations for source redshift $z_s = 1.5$. The yellow regions represent positive convergence, while the blue regions indicate negative convergence. The convergence maps exhibit similar large-scale structures.	67

7.5	Visualization of the Fibonacci grid with $N_{\text{patches}} = 273$ patches, each covering approximately $10 \times 10 \text{ deg}^2$. After the optimization and masking, the number of patches is reduced to $N_{\text{patches}} = 194$, effectively covering 47% of the sky. Each panel shows the patches distribution on the Front, Top view and the final patches from the front.	68
7.6	Extraction of a patch from the full-sky convergence map using a Fibonacci grid. The patch covers an area of $10^\circ \times 10^\circ$ and is centered at the vertices of the Fibonacci grid. From the left to the right, the panels show the original extracted patch, patch rotated 45° around the center and the final patch after the second rotation. The red shaded region represents the final patch we used for analysis.	69
7.7	Effect of Gaussian smoothing on a noisy convergence map. Each panel shows the result of applying a Gaussian filter with a different smoothing scale $\theta_G = 2', 5', 8',$ and $10'$. As the smoothing scale increases, small-scale noise is progressively suppressed, and large-scale structures become more prominent. This demonstrates how Gaussian smoothing effectively reduces shape noise while enhancing the detection of the underlying lensing signal.	70
7.8	Average standard deviation of the noiseless convergence maps for the BIGBOX and TILED simulations. The standard deviation increases with redshift and smoothing scale, with a subtle difference between the BIGBOX and TILED simulations.	71
7.9	Average $\sigma_1 = \sqrt{\kappa_x^2 + \kappa_y^2}$ of the noiseless convergence maps for the BIGBOX and TILED simulations. They are calculated for the smoothing scales $\theta_G = 2', 5', 8',$ and $10'$. The values decrease as the smoothing scale increases, while the difference between the BIGBOX and TILED simulations or the redshifts is subtle.	73
8.1	Comparison of the mean values of the angular power spectrum ($C_\ell^{\kappa\kappa}$) for different source redshifts ($z_s = 0.5, 1.0, 1.5, 2.0, 2.5$) obtained from the BIGBOX (solid lines) and TILED (dashed lines) simulations. The lower subplots show the ratio of the TILED to BIGBOX mean values, with a reference line at unity to facilitate the assessment of agreement between the two simulations.	77
8.2	Comparison of the covariance matrices and correlation matrices of the angular power spectrum ($C_\ell^{\kappa\kappa}$) between the BIGBOX and TILED simulations for various source redshifts ($z_s = 0.5, 1.0, 1.5, 2.0, 2.5$). The displayed ratios represent the element-wise division of the covariance and correlation matrices from the TILED simulations by those from the BIGBOX simulations. The ‘avg’ denotes the average ratio of the considered matrix elements.	77
8.3	Same as Figure 8.1, but for the bispectrum.	79

8.4	Similar to Figure 8.2, but for the correlation (upper) and covariance (lower) of bispectrum. The noisy nature of the bispectrum covariance makes it challenging to discern clear trends between the simulations.	80
8.5	Same as Figure 8.1, but for the probability density function (PDF) of the convergence field. The comparison highlights the agreement in mean PDF values between the simulations across different redshifts.	81
8.6	Same as Figure 8.2, but for the covariance matrices of the PDF. The covariance ratios indicate higher covariance in the BIGBOX simulations, particularly at higher redshifts.	81
8.7	Same as Figure 8.1, but for peak counts in the convergence maps. The analysis reveals deviations at low ν values due to resolution limitations affecting low-density regions.	82
8.8	Same as Figure 8.2, but for the covariance matrices of peak counts. The covariance ratios suggest increased covariance in the BIGBOX simulations, with pronounced effects at higher redshifts.	82
8.9	Same as Figure 8.1, but for minima in the convergence maps. The comparison underscores the simulation's limitations at resolving low-density minima accurately.	83
8.10	Same as Figure 8.2, but for the covariance matrices of minima. The covariance ratios reflect higher values in the BIGBOX simulations, consistent with other statistical measures.	83
8.11	Same as Figure 8.1, but for Minkowski Functionals (area V_0 , perimeter V_1 , and genus V_2). The agreement in mean values between simulations is generally good, with some discrepancies at extreme density thresholds.	84
8.12	Similar to Figure 8.2, but for the correlation (upper) and covariance (lower) of Minkowski Functionals.	85
8.13	Average ratio of covariance matrices of statistical measures between the BIGBOX and TILED simulations for different shape noise levels (see Table 1.1). The increasing trend indicates does not affected by the noise level.	86
8.14	Same as Figure 8.13, but for the correlation matrices. The off-diagonal elements compared to the diagonal elements do not show a clear trend with noise levels.	86
8.15	Average ratio of covariance matrices of statistical measures between the BIGBOX and TILED simulations for different smoothing scales. Larger smoothing scales lead to increased discrepancies in covariance estimates due to the loss of small-scale information.	87
8.16	Same as Figure 8.15, but for the correlation matrices. The instability at larger smoothing scales reflects the challenges in capturing correlations at reduced resolutions.	87

8.17	Ratio of covariance matrices of the angular power spectrum ($C_{\ell}^{\kappa\kappa}$) between the BIG-BOX and TILED simulations for different shape noise levels (see Table 1.1). The sensitivity of the power spectrum to noise is evident from the fluctuating covariance ratios with higher noise levels.	88
8.18	Same as Figure 8.17, but for the non-Gaussian statistical measures. The robustness of these measures against noise variations is reflected in the relatively stable covariance ratios.	88
8.19	Same as Figure 8.18, but showing the impact of different smoothing scales on the covariance matrices of non-Gaussian statistical measures. The results emphasize how increased smoothing affects the detection and characterization of small-scale features.	89
9.1	The ratios of covariance matrices and correlation matrices of power spectrum and bispectrum between the patches around special directions and the rest of the patches.	91
9.2	The same as Figure 9.1, but for PDF, peak/minima counts and Minkowski functionals. The box replication effect significantly enhances the covariance matrix.	91
9.3	The ratios of mean and variance of power spectrum and bispectrum between the patches around special directions and the rest of the patches. The mean of suspected patches are biased and the variance is larger.	92
9.4	The same as Figure 9.3, but for PDF, peak/minima counts and Minkowski functionals. The suspected patches tend to have more extreme values and larger variance.	92

List of Tables

1.1	Comparison of Key Galaxy Surveys for Weak Lensing	3
7.1	Cosmological parameters used in the N-body simulations.	64
7.2	Summary of the statistical measures employed in this investigation, including their respective value ranges and computational subroutines utilized for analyses.	71

Chapter 1

Introduction

Contents

1.1	Historical Overview	1
1.2	Astronomical Surveys and Observations	2
1.3	Constraint from Weak Lensing	4
1.4	Aim of this Thesis	6
1.5	Structure of the Thesis	7

1.1 Historical Overview

Over the past century, cosmological observations have profoundly reshaped our understanding of the universe. [Hubble \(1925\)](#) measured the distances to spiral nebulae, including the Andromeda Galaxy, demonstrating that these ‘nebulae’ were actually galaxies outside the Milky Way. Later, [Hubble \(1929\)](#) observed that galaxies are receding from us at velocities proportional to their distances, leading to the formulation of Hubble’s Law and the revolutionary concept of an expanding universe. The discovery of the cosmic microwave background (CMB) radiation by [Penzias & Wilson \(1965\)](#) provided compelling evidence for the Big Bang theory, suggesting that the universe originated from a hot, dense state approximately 13.8 billion years ago. Subsequent missions like the Cosmic Background Explorer (COBE; [Smoot et al. 1992](#)) and the Wilkinson Microwave Anisotropy Probe (WMAP; [Bennett et al. 2003](#)) measured the CMB with unprecedented precision. In the 1970s, Rubin and Ford analyzed galaxy rotation curves and found that galaxies rotate at speeds that cannot be accounted for by the visible matter alone ([Rubin & Ford, 1970](#); [Rubin et al., 1980](#)). This discrepancy provided strong evidence for the existence of dark matter, a mysterious form of matter that does not emit, absorb, or reflect light. Dark matter is now understood to constitute about 27% of the universe’s mass-energy content. The late 1990s witnessed the surprising discovery that the expansion of the universe is accelerating, based on observations of distant Type Ia supernovae by the Supernova Cos-

mology Project and the High-Z Supernova Search Team (Riess et al., 1998; Perlmutter et al., 1999). This acceleration implies the existence of dark energy, an enigmatic force that permeates all of space and makes up approximately 68% of the universe’s total mass-energy budget. The Neutrino Oscillation experiments, like the Super-Kamiokande, have demonstrated that neutrinos have mass and can change flavor as they travel, challenging the Standard Model of particle physics and have significant implications for our understanding of the universe’s evolution, particularly in the context of nucleosynthesis and the cosmic neutrino background (Fukuda et al., 1998; Ahmad et al., 2001). In 2015, the Laser Interferometer Gravitational-Wave Observatory (LIGO) made the first direct detection of gravitational waves providing direct evidence for the existence of gravitational waves, confirming a key prediction of General Relativity, opened a new window for observing cosmic events (Abbott et al., 2016). As observational technologies continue to advance, ongoing and future discoveries promise to further refine our understanding of the universe, addressing the remaining mysteries of dark matter, dark energy, and the fundamental forces shaping the universe.

From a theoretical standpoint, the cornerstone of modern cosmology is Einstein’s General Theory of Relativity, formulated in 1915 (Einstein, 1915). General Relativity provides the fundamental framework for explaining gravitational phenomena on cosmic scales, including the dynamics of the universe’s expansion, black holes, and gravitational lensing effects. Building upon Einstein’s equations, Friedmann (1922) and Lemaître (1931) independently derived solutions that describe a homogeneous and isotropic universe. These solutions led to the concept of an expanding or contracting universe and forms the mathematical foundation for the standard cosmological model. In the late 1940s, Gamow (1948), along with his collaborators Alpher & Herman (1948), proposed the Big Bang nucleosynthesis theory, which explains the formation of light elements like hydrogen and helium in the early universe. Peebles (1968), Zeldovich & Sunyaev (1969) further developed the theory of the recombination era, when the universe cooled enough for electrons and protons to combine into neutral hydrogen, allowing photons to travel freely, creating the CMB radiation. Subsequently, the theory of Baryonic Acoustic Oscillations (BAO) was introduced by Sunyaev & Zeldovich (1970), independently by Peebles & Yu (1970), which describes the imprint of primordial sound waves in the distribution of galaxies and the CMB. To address the Big-Bang’s challenges, the concept of cosmic inflation was introduced by Guth (1981), Linde (1982), and others. Together, these theories contribute to a comprehensive picture of the universe’s origin, composition, and evolution—a rich tapestry woven from both theoretical insights and observational discoveries.

1.2 Astronomical Surveys and Observations

Astronomical surveys are extensive observational projects designed to map large regions of the sky with high depth and precision, producing critical datasets for fundamental questions in astrophysics

and cosmology. They aim to test the standard cosmological model (Λ CDM) by providing precise measurements that can confirm or challenge it, addressing issues like the Hubble tension—a discrepancy in expansion rate measurements from early (Planck Collaboration et al., 2016) and late (Riess et al., 2019) observations—and inconsistencies in parameters like S_8 . Surveys also study the formation and evolution of cosmic structures by mapping millions of galaxies and dark matter distributions using techniques like weak gravitational lensing and galaxy-galaxy lensing(Mandelbaum et al., 2013; Abbott et al., 2022).

These surveys employ different methodologies:

Imaging surveys capture wide-field images across multiple wavelengths to map cosmic structures and analyze galaxy populations (e.g., SDSS (Kollmeier et al., 2019), DES (Abbott et al., 2018), LSST (Ivezić et al., 2019)), while spectroscopic surveys collect spectral data revealing redshifts, compositions, and kinematics essential for studying galaxy dynamics and the universe’s expansion (e.g., BOSS (Dawson et al., 2013), DESI (DESI Collaboration et al., 2016), KiDS with spectroscopic extensions (de Jong et al., 2013)).

They can be ground-based, utilizing Earth-based telescopes but limited by atmospheric effects (e.g., HSC (Aihara et al., 2018), DES, KiDS), or space-based, operating above Earth’s atmosphere for higher clarity and sensitivity, especially in inaccessible wavelengths (e.g., HST (Freedman et al., 2001), the upcoming Nancy Grace Roman Space Telescope(Spergel et al., 2015), and the Gaia mission(Gaia Collaboration et al., 2016)).

Surveys are also classified into Stage-III and Stage-IV based on technological sophistication and scale (Albrecht et al., 2006). Stage-III surveys (e.g., DES, KiDS, HSC) represent the current generation aiming to refine cosmological parameters and deepen understanding of dark energy and dark matter. Stage-IV surveys (e.g., Rubin Observatory (Ivezić et al., 2019), DESI, the upcoming Roman Space Telescope) are the next generation characterized by scale and precision, aiming for high-precision cosmological measurements and deeper exploration of dark energy and dark matter.

Several significant galaxy surveys have been designed to measure weak lensing signals with high precision. Table 1.1 provides a comprehensive overview of four pivotal surveys focusing on their observational capabilities.

Table 1.1: Comparison of Key Galaxy Surveys for Weak Lensing

Survey	Area (deg ²)	Approx. Galaxy Density (arcmin ⁻²)	Median Redshift
DES/KiDS	~5,000	7	0.4
HSC Wide	~1,400	15	0.7
LSST	~18,000	30	1.0
Roman	~2,000	50	1.5

The Dark Energy Survey (DES; The Dark Energy Survey Collaboration 2005; Abbott et al. 2018, 2021) utilized the 570-megapixel Dark Energy Camera (DECam; Flaugher et al. 2015) mounted on

the 4-m Blanco Telescope at the Cerro Tololo Inter-American Observatory (CTIO) in Chile. Over the course of its operation, DES observed more than 300 million galaxies across approximately 5,000 deg² of the southern sky in five optical bands (g , r , i , z , Y). It achieved an effective galaxy density of about ~ 6 arcmin⁻² and provided photometric redshift estimates up to $z \sim 1.2$. The data collected by DES has made significant contributions to cosmology and astrophysics, including precise measurements of cosmic shear (Amon et al., 2022) and galaxy clustering (Abbott et al., 2022).

The Hyper Suprime-Cam Subaru Strategic Program (HSC-SSP; Aihara et al. 2018) comprises three layers: Wide, Deep, and UltraDeep, conducted with the 8.2-m Subaru Telescope equipped with the 870-megapixel Subaru Hyper Suprime-Cam (HSC; Miyazaki et al. 2018). The Wide layer covers approximately 1,400 deg², yielding galaxy densities of around ~ 15 arcmin⁻². Photometric redshifts extend up to $z \sim 2$. The superior imaging quality of HSC enhances the accuracy of weak lensing measurements and contributes to tighter cosmological constraints (Hikage et al., 2019).

The Legacy Survey of Space and Time (LSST; LSST Science Collaboration et al. 2009; Ivezić et al. 2019) is conducted at the Vera C. Rubin Observatory. Over a 10-year period, LSST will survey approximately 18,000 deg² of the sky. It is expected to detect around 20 billion galaxies, corresponding to galaxy densities exceeding ~ 30 arcmin⁻², with redshift measurements up to $z \sim 3$. LSST's vast dataset will substantially improve the statistical precision of weak lensing analyses and further refine cosmological models (LSST Dark Energy Science Collaboration, 2012).

The *Nancy Grace Roman Space Telescope* (Roman; Spergel et al. 2015) will conduct wide-field near-infrared imaging and spectroscopy from space scheduled for launch in the mid-2020s. Covering approximately 2,000 deg². The expected galaxy densities exceed ~ 50 arcmin⁻², facilitated by its space-based observations. The mission aims to provide spectroscopic redshifts higher than $z \sim 3$, significantly enhancing the precision of weak lensing measurements.

1.3 Constraint from Weak Lensing

While Λ CDM has been successful in explaining a wide range of cosmological observations, several tensions have emerged between different datasets. A statistically significant discrepancy of about 4 to 5σ between the value of the Hubble constant (H_0) inferred from the Planck CMB measurements (Di Valentino et al., 2021) and the late-time measurements of local universe cosmic distance ladder measurements (Riess et al., 2022). In addition to the Hubble tension, discrepancies have been observed in the measurements of the parameter $S_8 \equiv \sigma_8 \sqrt{\Omega_m/0.3}$, where σ_8 represents the root-mean-square fluctuation of matter density in spheres of $8 h^{-1}$ Mpc, and Ω_m is the present-day matter density parameter. Several large-scale structure (LSS) experiments have reported 2 to 3σ lower values of S_8 compared to those inferred from Planck CMB data (Hikage et al., 2019; Asgari et al., 2021; García-García et al., 2021).

Some of the strongest constraints on S_8 from LSS observations come from the study of cosmic shear, which is the weak gravitational lensing of distant galaxies by the intervening LSS along the line of sight. These small, coherent distortions in the shapes of background galaxies are sensitive to both the amplitude of matter density fluctuations (σ_8) and the growth of these fluctuations over cosmic time (Bartelmann & Schneider, 2001; Bartelmann, 2010; Kilbinger, 2015). While there is a degeneracy between Ω_m and σ_8 in cosmic shear analyses, the product S_8 is tightly constrained (Kilbinger, 2015; Mandelbaum, 2018).

Traditionally, the power spectrum has been the primary statistical measure used to quantify the distribution of matter density fluctuations in the universe (Hikage et al., 2019; Dalal et al., 2023). However, the weak lensing field is inherently non-Gaussian due to the nonlinear evolution of structures under gravity, leading to features resulting from gravitational collapse, mergers, and other astrophysical processes. The power spectrum, being a two-point statistic, captures only the Gaussian aspects of the field and thus cannot fully characterize these non-Gaussian features.

To fully leverage the information contained in the weak lensing field, it is essential to employ higher-order statistics that are sensitive to the non-Gaussianities. Various higher-order statistics have been studied in the past, such as: moments (Petri et al., 2015; Gatti et al., 2020), Minkowski functionals (Marques et al., 2019; Grewal et al., 2022), probability distribution function (Boyle et al., 2021; Thiele et al., 2023; Uhlemann et al., 2023), Peak and Minima Counts (Martinet et al., 2018; Marques et al., 2024), three-point statistics (Takada & Jain, 2004; Fu et al., 2014), and deep learning (Fluri et al., 2018, 2022). Employing these higher-order statistics enhances the cosmological constraining power of weak lensing analyses, potentially alleviating tensions in parameter estimates and providing deeper insights into the underlying physics.

However, accurately estimating the cosmological constraints from these higher-order statistics requires precise knowledge of their covariance matrices. The covariance matrix quantifies the uncertainties and correlations between different statistical measures, and it is crucial for techniques like Fisher forecasting and likelihood analyses that predict parameter constraints (Tegmark, 1997). To estimate these covariance matrices, we rely on applying the same statistical measurements to a large ensemble of mock datasets that mimic real observations, accounting for the survey’s specific characteristics like super-sample covariance (Takada & Hu, 2013) and noise properties (Wu et al., 2019). For weak lensing surveys, these mock datasets are generated through ray-tracing simulations of light propagation through the universe, using lightcones constructed from cosmological N-body simulations (Shirasaki et al., 2019; Euclid Collaboration et al., 2024).

One common approach is to stack multiple multi-resolution simulation boxes to generate non-repeating lightcones that cover a wide range of redshifts (Fosalba et al., 2015; Crocce et al., 2015; Takahashi et al., 2017; DeRose et al., 2019). While this method successfully captures the evolution of structures over cosmic time, it can struggle with achieving high redshift resolution and requires

significant computational resources. Alternatively, repeating a single simulation box multiple times along the line of sight to construct the lightcone retains high redshift resolution and is computationally efficient ([Sehgal et al., 2010](#); [Liu et al., 2018](#); [Stein et al., 2020](#); [Omori, 2024](#)). However, this repetitive box method introduces artefacts like box replication effects ([Chen & Yu, 2024](#)).

1.4 Aim of this Thesis

The overarching goal of this thesis is to enhance the precision and reliability of cosmological constraints derived from higher-order weak lensing statistics by addressing key challenges in the estimation of their covariance matrices. Specifically, we focus on the impact of super-sample covariance (SSC) and box replication effects in simulations used for weak lensing analyses.

While super-sample covariance has been extensively studied and is well-understood for the power spectrum ([Takada & Hu, 2013](#); [Barreira & Schmidt, 2017](#); [Barreira et al., 2018](#)), its influence on higher-order statistics remains largely unexplored. Existing theoretical predictions for covariances that include SSC effects ([Linke et al., 2023](#); [Uhlemann et al., 2023](#)) have not yet been thoroughly tested for these higher-order statistic ([Euclid Collaboration et al., 2023](#)). Moreover, while the impact of SSC has been studied in three-dimensional (3D) box simulations ([Bayer et al., 2023](#)), its effects in two-dimensional (2D) weak lensing simulations have not been systematically examined.

Our first aim is to fill this gap by investigating how SSC affects higher-order weak lensing statistics and their covariance matrices. To achieve this, we conduct two sets of simulations:

BigBox Simulations — Large-volume simulations that naturally include super-survey modes, capturing the SSC effects inherent in the universe’s large-scale structure.

Tiled Simulations — Simulations that replicate smaller boxes to cover the desired light cone, which will suppress super-survey modes and thus underestimate SSC.

By comparing the results from these two simulation strategies, we assess the extent to which SSC impacts the estimation of cosmological parameters using higher-order statistics. We examine how the covariance matrices are affected by varying smoothing scales and shape noise levels, which are crucial factors in weak lensing analyses. This comprehensive study allows us to determine the reliability of cosmological parameter estimations and to identify the conditions under which SSC effects become significant.

The second aim of this thesis is to investigate the impact of box replication effects in weak lensing simulations. As introduced earlier, the box replication is a common technique used to extend the effective simulation volume by periodically replicating a single simulation box along different axes. While this method is computationally efficient and retains high redshift resolution, it introduces artificial periodicity and can lead to under-predicts the variance of the imulations on large scales ([Zürcher et al., 2021](#)).

Previous studies have examined box replication effects primarily for power spectrum and moments, focusing on biases in mean values (Chen & Yu, 2024). Another study (Fluri et al., 2019) examined the impact of the replication scheme on the predictions of the power spectrum and Convolutional Neural Networks (CNN) by increasing the boxsize and number of particles in a reference simulation while keeping the particle density constant. However, the impact on higher-order statistics and their covariance matrices has not been thoroughly explored. Given that higher-order statistics are more and more used in weak lensing analyses, it is essential to understand how box replication affects these statistics and their covariance matrices. By investigating these effects, we aim to provide guidelines for future surveys to mitigate these artefacts and improve the accuracy of their cosmological parameter estimates.

By addressing these two key challenges, this thesis contributes to the broader effort of maximizing the scientific return of weak lensing surveys. Accurate covariance estimation is essential for improving the precision of cosmological parameter constraints derived from higher-order statistics, enhancing the utility of these statistics for probing the underlying physics of structure formation and dark matter, and guiding the design of future survey missions.

1.5 Structure of the Thesis

This dissertation is organized into nine chapters that systematically develop the theoretical framework, methodologies, and empirical analyses pertinent to the research objectives outlined in the previous sections.

This dissertation is organized into chapters that develop the theoretical framework, methodologies, and empirical analyses pertinent to the research objectives.

In Chapter 2, we provide a comprehensive overview of modern cosmology, tracing the historical development of the field and highlighting key theoretical milestones that have shaped our current understanding of the universe.

Chapter 3 focuses on the theoretical basics and observational aspects of weak gravitational lensing.

In Chapter 4, we explore the statistical measures employed in weak lensing analyses to extract cosmological information from observational data, focusing on the power spectrum and higher-order statistics.

Chapter 5 addresses the theoretical prediction of covariance matrices including super-sample covariance and how the covariance affects the cosmological constraints.

In Chapter 6, we review the numerical methods in astrophysics and cosmology, focusing on the N-body simulations and weak lensing simulations.

In Chapter 7, we introduce the methodologies used in this thesis, including the simulation strate-

gies, data generation, statistical measurements, and covariance matrix estimation.

In Chapter 8, we present the results of our analyses, comparing the mean values and covariance matrices of higher-order statistics derived from the BigBox and Tiled simulations, examining how SSC influences the variances and correlations in the data.

Chapter 9 synthesizes the findings from our analyses, discussing their implications for weak lensing cosmology. The chapter explores the potential strategies for mitigating these effects in future analyses and simulations, and considers how our results inform the design and interpretation of upcoming weak lensing surveys.

The thesis concludes with Chapter 10, where we summarize the key contributions and conclusions of this research. We reflect on how the work advances our understanding of super-sample covariance and box replication effects in the context of higher-order weak lensing statistics.

Chapter 2

Cosmology

Contents

2.1	Einstein Field Equations	9
2.2	FLRW Metric and the Friedmann Equations	11
2.3	Cosmological Distances	14
2.4	Initial Conditions	15
2.5	The linear evolution of density fluctuations	18
2.6	Spherical Collapse	20
2.7	Dark Matter Halo	22

In this chapter, we provide an overview of the fundamental concepts and equations that underpin the field of cosmology following textbooks [Dodelson \(2003\)](#) and [Weinberg \(2008\)](#).

2.1 Einstein Field Equations

The Einstein Field Equations are the fundamental equations of General Relativity, describing how matter and energy influence the curvature of spacetime. Introduced by [Einstein \(1915\)](#), these equations extend Newton's law of universal gravitation to a relativistic context, accounting for the effects of high velocities and strong gravitational fields.

The EFE establish a relationship between the geometry of spacetime and the distribution of matter within it. They are expressed with the metric $g_{\mu\nu}$, which describes the curvature of spacetime, and the stress-energy tensor $T_{\mu\nu}$, which characterizes the distribution of matter and energy. The EFE are given by:

$$G_{\mu\nu} + \Lambda g_{\mu\nu} = \frac{8\pi G}{c^4} T_{\mu\nu}, \quad (2.1)$$

where Λ is the cosmological constant, G is the gravitational constant, and c is the speed of light. The

Einstein tensor $G_{\mu\nu}$ is defined by:

$$G_{\mu\nu} = R_{\mu\nu} - \frac{1}{2}Rg_{\mu\nu}, \quad (2.2)$$

the $R_{\mu\nu}$ is the Riemann tensor, described by the Christoffel symbols $\Gamma_{\mu\nu}^\lambda$ as:

$$R_{\mu\nu} = \partial_\lambda \Gamma_{\mu\nu}^\lambda - \partial_\nu \Gamma_{\mu\lambda}^\lambda + \Gamma_{\lambda\sigma}^\lambda \Gamma_{\mu\nu}^\sigma - \Gamma_{\mu\sigma}^\lambda \Gamma_{\lambda\nu}^\sigma, \quad (2.3)$$

the Ricci scalar R is given by:

$$R = g^{\mu\nu} R_{\mu\nu}, \quad (2.4)$$

Assuming a perfect fluid as the source of the gravitational field, the stress-energy tensor is given by

$$T_{\mu\nu} = (\rho + p) u_\mu u_\nu + p g_{\mu\nu}, \quad (2.5)$$

where ρ is the energy density, p is the pressure, and u_μ is the four-velocity of the fluid. In a homogeneous and isotropic universe, u_μ is given by

$$u_\mu = (-c, 0, 0, 0), \quad (2.6)$$

Therefore, each component of the stress-energy tensor can be expressed as

$$T_{00} = \rho c^2, \quad T_{ij} = p g_{ij}, \quad (2.7)$$

Different species of matter and energy contribute to the energy density ρ and pressure P in the universe. The equation of state parameter w is defined as the ratio of pressure P to energy density ρ :

$$w = \frac{p}{\rho}. \quad (2.8)$$

For perfect fluids, the equation of state parameter can be derived by considering the trace of the stress-energy tensor:

$$0 = T = g^{\mu\nu} T_{\mu\nu} = (\rho + p)(-1) + 4p = -\rho + 3p, \quad (2.9)$$

For non-relativistic matter where $p = 0$, the equation of state parameter is $w = 0$. For cosmological constant, the equation of state parameter can be derived by comparing the effective stress-energy of

the cosmological constant $T_{\mu\nu}^{(\Lambda)} = \rho_\Lambda g_{\mu\nu}$ to the stress-energy tensor of a perfect fluid:

$$\rho_\Lambda = \frac{\Lambda c^4}{8\pi G} \quad (2.10)$$

$$(\rho_\Lambda + p_\Lambda) u_\mu u_\nu + p_\Lambda g_{\mu\nu} = T_{\mu\nu}^{(\Lambda)} = \rho_\Lambda g_{\mu\nu} \quad (2.11)$$

$$\rho_\Lambda + p_\Lambda = 0 \quad (\text{valid for all } \mu, \nu)$$

$$p_\Lambda = -\rho_\Lambda \quad (2.12)$$

Therefore, the equation of state parameter for cosmological constant is $w = -1$.

To summarize, the Equations of States for each component of the universe are:

$$w = \begin{cases} 0 & \text{matter,} \\ \frac{1}{3} & \text{Radiation,} \\ -1 & \text{Cosmological Constant.} \end{cases} \quad (2.13)$$

In realistic universe, the energy density and pressure are contributed by multiple components. Assuming the interaction between different components is negligible, the total stress-energy tensor is the sum of the individual stress-energy tensors:

$$T_{\mu\nu} = \sum_i (T_i)_{\mu\nu}, \quad (2.14)$$

where i denotes the different components of the universe. Therefore, the total energy density and pressure are given by:

$$\rho = \sum_i \rho_i, \quad p = \sum_i p_i. \quad (2.15)$$

In the late universe, where each component evolves adiabatically, the energy density scales as:

$$\rho_i \propto a^{-3(1+w_i)}, \quad (2.16)$$

where a is the scale factor, and w_i is the equation of state parameter for the i -th component.

2.2 FLRW Metric and the Friedmann Equations

The Friedmann-Lemaître-Robertson-Walker (FLRW) metric describes a homogeneous and isotropic universe and is given by [Weinberg \(1972\)](#):

$$ds^2 = -c^2 dt^2 + a^2(t) [d\chi^2 + f_K^2(\chi) (d\theta^2 + \sin^2 \theta d\phi^2)], \quad (2.17)$$

where $a(t)$ is the scale factor, χ is the comoving radial coordinate, and $d\Omega^2 = d\theta^2 + \sin^2 \theta d\phi^2$ represents the metric on the unit two-sphere. The function $f_K(\chi)$ encodes the spatial curvature of the universe and is defined as:

$$f_K(\chi) = \begin{cases} \frac{1}{\sqrt{-K}} \sinh(\sqrt{-K}\chi) & \text{for } K < 0, \\ \chi & \text{for } K = 0, \\ \frac{1}{\sqrt{K}} \sin(\sqrt{K}\chi) & \text{for } K > 0, \end{cases} \quad (2.18)$$

where K is the spatial curvature constant, with $K < 0$ corresponding to an open universe, $K = 0$ to a flat universe, and $K > 0$ to a closed universe.

For the FLRW metric, the non-zero components of the Einstein tensor are:

$$G_{00} = 3 \left(\frac{\dot{a}}{a} \right)^2 + 3 \frac{Kc^2}{a^2}, \quad (2.19)$$

$$G_{ij} = - \left(2 \frac{\ddot{a}}{a} + \left(\frac{\dot{a}}{a} \right)^2 + \frac{Kc^2}{a^2} \right) a^2 g_{ij}, \quad (2.20)$$

where the dot denotes differentiation with respect to cosmic time t .

Substituting the components of $G_{\mu\nu}$ and $T_{\mu\nu}$ into the Einstein field equations (2.1), we obtain the Friedmann equations (Friedmann, 1922):

- First Friedmann equation (00 component):

$$3 \left(\frac{\dot{a}}{a} \right)^2 + 3 \frac{Kc^2}{a^2} + \Lambda c^2 = \frac{8\pi G}{c^4} \rho c^2 \quad (2.21)$$

$$\left(\frac{\dot{a}}{a} \right)^2 = \frac{8\pi G}{3} \rho - \frac{Kc^2}{a^2} + \frac{\Lambda c^2}{3} \quad (2.22)$$

- Second Friedmann equation (ii component):

$$-\left(2 \frac{\ddot{a}}{a} + \left(\frac{\dot{a}}{a} \right)^2 + \frac{Kc^2}{a^2} \right) g_{ii} + \Lambda c^2 g_{ii} = \frac{8\pi G}{c^4} P g_{ii} \quad (2.23)$$

$$\frac{\ddot{a}}{a} = -\frac{4\pi G}{c^4} P - \frac{1}{2} \left(\left(\frac{\dot{a}}{a} \right)^2 + \frac{Kc^2}{a^2} - \Lambda c^2 \right) \quad (2.24)$$

$$\frac{\ddot{a}}{a} = -\frac{4\pi G}{3} \left(\rho + \frac{3P}{c^2} \right) + \frac{\Lambda c^2}{3} \quad (2.25)$$

Introducing the Hubble parameter H and the critical density ρ_c , we can simplify the Friedmann equations. The Hubble parameter is defined as:

$$H = \frac{\dot{a}}{a}, \quad (2.26)$$

and the critical density is defined as:

$$\rho_c = \frac{3H^2}{8\pi G}. \quad (2.27)$$

Substituting H and ρ_c into the first Friedmann equation (2.22), we obtain:

$$H^2 = H^2 \frac{\rho}{\rho_c} - \frac{Kc^2}{a^2} + \frac{\Lambda c^2}{3}. \quad (2.28)$$

Rearranging terms, we get:

$$1 = \frac{\rho}{\rho_c} - \frac{Kc^2}{a^2 H^2} + \frac{\Lambda c^2}{3H^2}. \quad (2.29)$$

Defining the density parameters:

$$\Omega_m = \frac{\rho_m}{\rho_c}, \quad \Omega_r = \frac{\rho_r}{\rho_c}, \quad \Omega_\Lambda = \frac{\rho_\Lambda}{\rho_c} = \frac{\Lambda c^2}{3H^2}, \quad \Omega_K = -\frac{Kc^2}{a^2 H^2}, \quad (2.30)$$

where ρ_m and ρ_r are the energy densities of matter and radiation, respectively, and ρ_Λ is the effective energy density associated with the cosmological constant, we can write the first Friedmann equation as:

$$1 = \Omega_r + \Omega_m + \Omega_K + \Omega_\Lambda. \quad (2.31)$$

The evolution of the density parameters with the scale factor a can be derived from the conservation of energy-momentum and the equations of state. For matter-dominated and radiation-dominated universes, the energy densities scale as:

$$\rho_m \propto a^{-3}, \quad \rho_r \propto a^{-4}. \quad (2.32)$$

Therefore, the corresponding density parameters vary with a as:

$$\Omega_m(a) = \Omega_{m0} a^{-3} \left(\frac{H_0}{H(a)} \right)^2, \quad \Omega_r(a) = \Omega_{r0} a^{-4} \left(\frac{H_0}{H(a)} \right)^2, \quad (2.33)$$

where the subscript 0 denotes present-day values, and H_0 is the current Hubble parameter. Conventionally, the Hubble parameter is parametrized as:

$$H_0 = 100 h \text{ km s}^{-1} \text{Mpc}^{-1}, \quad (2.34)$$

where h is a dimensionless parameter that accounts for the uncertainty in the exact value of H_0 . It allows cosmological quantities to be expressed in a way that separates the dependence on the H_0 . Combining these expressions, the Friedmann equation (2.31) can be rewritten in terms of the present-

day density parameters:

$$\left(\frac{H(a)}{H_0}\right)^2 = \Omega_{r0}a^{-4} + \Omega_{m0}a^{-3} + \Omega_{K0}a^{-2} + \Omega_{\Lambda0}, \quad (2.35)$$

which describes the evolution of the Hubble parameter with scale factor a in terms of the contributions from radiation, matter, curvature, and the cosmological constant.

2.3 Cosmological Distances

For light-like (null) geodesics, the spacetime interval ds^2 is zero. Thus, the radial coordinate distance for a photon traveling from a source to the observer is obtained from the null condition:

$$ds^2 = 0 \quad \Rightarrow \quad d\chi = \frac{c dt}{a(t)}. \quad (2.36)$$

Integrating this expression, we obtain the comoving radial distance $\chi(z)$ as a function of redshift z :

$$\chi(z) = \int_{t(z)}^{t_0} \frac{c dt'}{a(t')} = \int_0^z \frac{c dz'}{H(z')}, \quad (2.37)$$

where t_0 is the present time. The redshift z is related to the scale factor by $1 + z = \frac{a_0}{a(t)}$, with $a_0 \equiv a(t_0) = 1$ for the present universe.

In the late universe, where radiation is negligible compared to matter and dark energy, the Hubble parameter $H(z)$ is given by the Friedmann Eq. (2.35):

$$H(z) = H_0 \sqrt{\Omega_{m0}(1+z)^3 + \Omega_{K0}(1+z)^2 + \Omega_{\Lambda0}}, \quad (2.38)$$

where H_0 is the present-day Hubble constant, and Ω_{m0} , Ω_{K0} , and $\Omega_{\Lambda0}$ are the present-day density parameters for matter, curvature, and dark energy, respectively.

2.3.1 Luminosity Distance

The luminosity distance $d_L(z)$ is a key concept in observational cosmology, relating the intrinsic luminosity L of an astronomical object to the observed flux F via the inverse-square law (Carroll et al., 1992):

$$F = \frac{L}{4\pi d_L^2}. \quad (2.39)$$

In an expanding universe, the luminosity distance accounts for the effects of redshift on both the energy of photons and the rate at which they are received. It is defined as (Hogg, 1999):

$$d_L(z) = (1+z) f_K(\chi(z)). \quad (2.40)$$

The luminosity distance is crucial for determining cosmological parameters using standard candles, such as Type Ia supernovae, whose intrinsic luminosities are known [Riess et al. \(1998\)](#). By measuring the observed flux F and applying Eq. (2.39), we can infer $d_L(z)$ and constrain cosmological models.

2.3.2 Angular Diameter Distance

The angular diameter distance $d_A(z)$ relates the physical size D of an object to its observed angular size:

$$\theta = \frac{D}{d_A}. \quad (2.41)$$

In an expanding universe, the angular diameter distance is given by ([Hogg, 1999](#)):

$$d_A(z) = \frac{f_K(\chi(z))}{1+z}. \quad (2.42)$$

The angular diameter distance is essential for studying standard rulers, such as the scale of baryon acoustic oscillations (BAO) in the cosmic microwave background and large-scale structure ([Eisenstein et al., 2005](#)). By measuring the angular size θ of these features and knowing their physical size D , we can determine $d_A(z)$ and thus constrain cosmological parameters.

2.4 Initial Conditions

The initial conditions of the universe are believed to originate from quantum fluctuations during the inflationary epoch. These fluctuations are imprinted on the cosmic microwave background (CMB) radiation, which provides a snapshot of the universe at the time of recombination, and these primordial perturbations served as the seeds for the formation of the large-scale structures (LSS) observed today

Figure 2.1 illustrates the CMB temperature power spectrum measured by the Planck satellite ([Planck Collaboration et al., 2014](#)), showing the primordial fluctuations imprinted at large angular scales ($\ell \lesssim 30$).

2.4.1 Primordial Power Spectrum

The standard single-field slow-roll inflation model predicts that the primordial fluctuations are nearly scale-invariant and Gaussian. The power spectrum of these primordial curvature perturbations is described by a nearly scale-invariant power-law form ([Dodelson, 2003](#)):

$$P_p(k) = A_s \left(\frac{k}{k_*} \right)^{n_s - 1}, \quad (2.43)$$

where A_s is the amplitude of the scalar fluctuations, k_* is the pivot scale, and n_s is the spectral index. The observational constraints on these parameters are provided by the Planck satellite ([Planck](#)

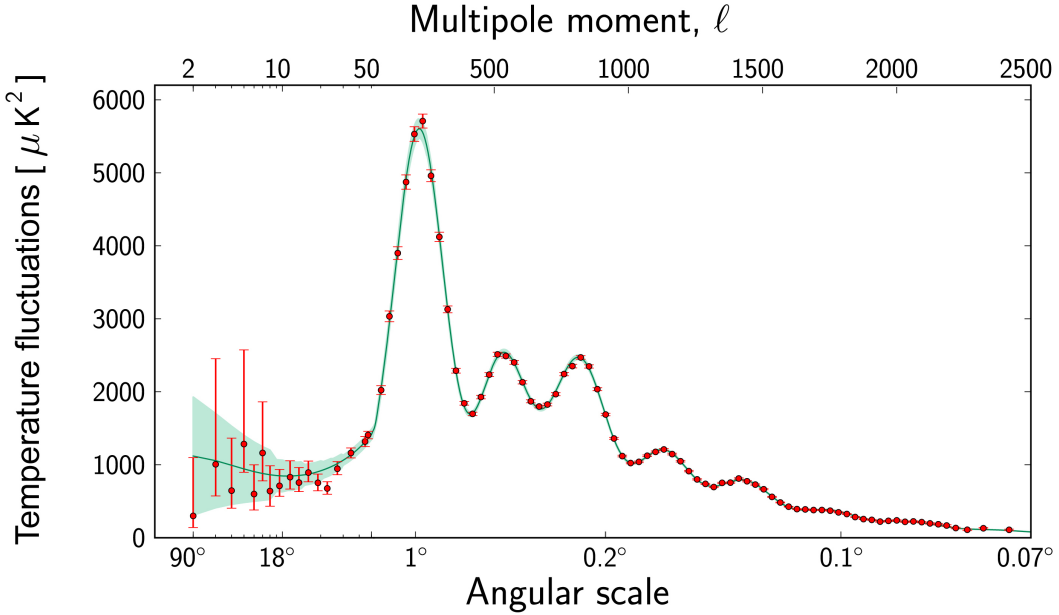


Figure 2.1: Angular Power Spectrum of Cosmic Microwave Background Temperature Fluctuations as a function of the multipole moment (ℓ) and the corresponding angular scale. The observational data are depicted by red markers with associated error bars, whereas the theoretical prediction derived from the Λ CDM cosmological model is represented by the green curve (Planck Collaboration et al., 2014). The primordial fluctuations imprinted at large angular scales ($\ell \lesssim 30$).

Collaboration et al., 2020):

$$A_s = (2.101_{-0.034}^{+0.031}) \times 10^{-9}, \quad n_s = 0.965 \pm 0.004. \quad (2.44)$$

for the pivot scale $k_* = 0.05 \text{ Mpc}^{-1}$.

As the universe evolves, various physical processes, such as radiation pressure, baryon-photon interactions, and dark matter dynamics, influence the growth of these initial perturbations. These effects are encapsulated in the transfer function $T(k)$, which modifies the primordial power spectrum to give the linear matter power spectrum at redshift z (Dodelson, 2003):

$$P(k, z) = P_p(k)T^2(k)D^2(z), \quad (2.45)$$

where $D(z)$ is the linear growth factor that describes the growth of perturbations in the linear regime, where each k -mode evolves independently of the others. The growth factor is given by:

$$D(a) = \frac{5\Omega_m a}{2} \int_0^1 \frac{dx}{(\Omega_m/x + \Omega_\Lambda x^2 + 1 - \Omega_m - \Omega_\Lambda)^{3/2}}, \quad (2.46)$$

where at the limit $a \rightarrow 0$, $D(a) \rightarrow a$.

The shape of $T(k)$ is determined by the Einstein-Boltzmann equations of a mixture of various energy components. Thus, there is no exact analytical form for $T(k)$; instead, it is typically computed using numerical codes such as CMB (Lewis et al., 2000) and CLASS (Blas et al., 2011).

Qualitatively, the transfer function behaves differently on scales relative to the equality scale k_{eq} . Since in the radiation-dominant era, the growth of perturbations on super-horizon scales is suppressed compared to those on sub-horizon scales. In the matter-dominant era, the growth of perturbations is the same on super-horizon and sub-horizon scales. Due to this, the transfer function behaves as:

$$T(k) \propto \begin{cases} 1 & \text{for } k \ll k_{\text{eq}}, \\ k^{-2} & \text{for } k \gg k_{\text{eq}}. \end{cases} \quad (2.47)$$

Figure 2.2 shows the linear matter power spectrum computed using the CLASS code. It is clear that the scaling of the linear power spectrum changes around k_{eq} . The wiggles around $k \sim 0.1 h/\text{Mpc}$ are due to Baryon Acoustic Oscillations (BAOs) imprinted.

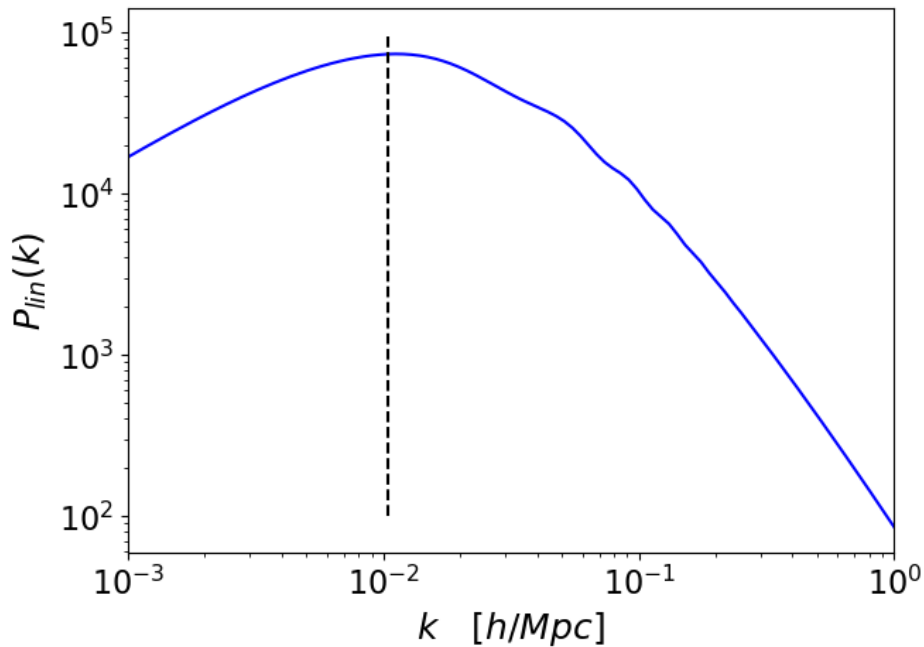


Figure 2.2: The linear matter power spectrum as a function of the wavenumber k computed using the CLASS code. The transition from the radiation-dominated to the matter-dominated era is evident around $k_{\text{eq}} = 0.0104 h/\text{Mpc}$ (Planck Collaboration et al., 2020).

2.4.2 Baryon Acoustic Oscillations

BAOs serve as a standard ruler for cosmological distance measurements and are crucial for constraining cosmological parameters. These features originate from the oscillatory behavior of the photon-baryon plasma in the primordial universe prior to the epoch of recombination. During this period, photons and baryons are tightly coupled, effectively forming a coherent photon-baryon fluid. The

coupling between photons and baryons is quantitatively characterized by the baryon-to-photon momentum density ratio, R , defined as:

$$R = \frac{\Pi_b}{\Pi_\gamma} = \frac{\rho_b \mathbf{v}_b}{(1 + \frac{1}{3}) \rho_\gamma \mathbf{v}_\gamma} = \frac{3\rho_b}{4\rho_\gamma}, \quad (2.48)$$

where ρ_b and ρ_γ denote the baryon and photon energy densities, respectively, while \mathbf{v}_b and \mathbf{v}_γ represent their respective velocities.

The propagation of acoustic waves within the photon-baryon plasma is governed by the effective sound speed, c_s , which arises from the interplay between radiation pressure and gravitational infall. The effective sound speed is derived from the effective pressure and energy density of the photon-baryon fluid:

$$\begin{aligned} c_s^2 &= \frac{\partial p_{\text{eff}}}{\partial \rho_{\text{eff}}} = \frac{\partial p_\gamma}{\partial (\rho_b + \rho_\gamma)} \\ &= \frac{1}{1+R} \frac{\partial p_\gamma}{\partial \rho_\gamma} = \frac{1}{1+R} \cdot \frac{1}{3} \\ c_s &= \frac{1}{\sqrt{3(1+R)}}, \end{aligned} \quad (2.49)$$

where p_γ and ρ_γ are the photon pressure and energy density, respectively.

The acoustic oscillations in the photon-baryon plasma can be described by solutions to the linearized perturbation equations (Eq. (2.62); we will discuss in the next section). We find that the perturbations in the photon density, δ_γ , exhibit harmonic oscillations with a wavenumber k and phase constant ϕ :

$$\delta_\gamma(k, t) \propto \cos(kc_s t + \phi), \quad (2.50)$$

where ϕ is a phase constant. Solutions of this form describe sound waves, propagating through the photon-baryon fluid.

2.5 The linear evolution of density fluctuations

Density fluctuations arise from quantum fluctuations during inflation and grow under the influence of gravity. Starting from the continuity and Euler equations, which govern the conservation of mass and momentum, respectively:

$$\frac{\partial \rho}{\partial t} + \nabla \cdot (\rho \mathbf{v}) = 0, \quad (2.51)$$

$$\frac{\partial \mathbf{v}}{\partial t} + (\mathbf{v} \cdot \nabla) \mathbf{v} = -\frac{\nabla P}{\rho} - \nabla \Phi, \quad (2.52)$$

where ρ is the density, v is the peculiar velocity field, P is the pressure, and Φ is the gravitational potential.

To analyze perturbations in an expanding universe, we move to comoving coordinates and express the density as a perturbation around the mean density, $\rho = \bar{\rho}(1 + \delta)$, where δ is the density contrast. The continuity and Euler equations then become:

$$\frac{\partial \delta}{\partial t} + \frac{1}{a} \nabla \cdot ((1 + \delta)v) = 0, \quad (2.53)$$

$$\frac{\partial v}{\partial t} + Hv + \frac{1}{a}(v \cdot \nabla)v = -\frac{\nabla \delta P}{a\bar{\rho}(1 + \delta)} - \frac{1}{a}\nabla\Phi, \quad (2.54)$$

where $a(t)$ is the scale factor, and $H = \dot{a}/a$ is the Hubble parameter.

To derive the equation of motion for the density contrast, we linearize the above equations under the assumption that $\delta \ll 1$ and v is small. Neglecting higher-order terms in δ and v , we obtain the linearized equations:

$$\frac{\partial \delta}{\partial t} + \frac{1}{a} \nabla \cdot v = 0, \quad (2.55)$$

$$\frac{\partial v}{\partial t} + Hv = -\frac{\nabla \delta P}{a\bar{\rho}} - \frac{1}{a}\nabla\Phi. \quad (2.56)$$

The gravitational potential Φ is related to the density contrast via Poisson's equation in comoving coordinates:

$$\nabla^2\Phi = 4\pi G\bar{\rho}a^2\delta, \quad (2.57)$$

where G is the gravitational constant. Assuming adiabatic perturbations, the pressure perturbation is related to the density perturbation by $\delta P = c_s^2\delta\rho = c_s^2\bar{\rho}\delta$, where c_s is the sound speed.

Taking the time derivative of the linearized continuity equation (2.55) and substituting the divergence of v from the linearized Euler equation (2.56), we obtain:

$$\frac{\partial^2 \delta}{\partial t^2} + 2H\frac{\partial \delta}{\partial t} - \frac{c_s^2}{a^2}\nabla^2\delta = 4\pi G\bar{\rho}\delta. \quad (2.58)$$

Transforming to Fourier space, where $\nabla^2\delta \rightarrow -k^2\tilde{\delta}(k, t)$, the equation becomes:

$$\ddot{\tilde{\delta}}(k, t) + 2H\dot{\tilde{\delta}}(k, t) + \left(\frac{c_s^2 k^2}{a^2} - 4\pi G\bar{\rho}\right)\tilde{\delta}(k, t) = 0, \quad (2.59)$$

where $\tilde{\delta}(k, t)$ is the Fourier transform of the density contrast.

Defining the effective frequency squared $\omega^2(k, t) = 4\pi G\bar{\rho} - \frac{c_s^2 k^2}{a^2}$, the equation simplifies to:

$$\ddot{\tilde{\delta}}(k, t) + 2H\dot{\tilde{\delta}}(k, t) - \omega^2(k, t)\tilde{\delta}(k, t) = 0. \quad (2.60)$$

The solutions to this differential equation depend on the sign of $\omega^2(k, t)$:

- **Gravity-Dominated Regime ($\omega^2(k, t) > 0$)**: For large-scale perturbations where gravity overcomes pressure forces (i.e., small k), the solutions are exponential:

$$\tilde{\delta}(k, t) = C_1 e^{\lambda t} + C_2 e^{-\lambda t}, \quad (2.61)$$

where $\lambda = \sqrt{\omega^2(k, t)}$. The growing mode ($e^{\lambda t}$) leads to the amplification of perturbations and structure formation, while the decaying mode ($e^{-\lambda t}$) becomes negligible over time.

- **Pressure-Dominated Regime ($\omega^2(k, t) < 0$)**: For small-scale perturbations where pressure resists gravitational collapse (i.e., large k), the solutions are oscillatory:

$$\tilde{\delta}(k, t) = e^{-Ht} (C_1 \cos(|\omega(k, t)|t) + C_2 \sin(|\omega(k, t)|t)). \quad (2.62)$$

The perturbations oscillate with frequency $|\omega(k, t)|$ and are damped by the cosmic expansion, preventing collapse on small scales.

These results illustrate the Jeans instability criterion, which states that perturbations grow only if their wavelength exceeds the Jeans length $\lambda_J = c_s \sqrt{\frac{\pi}{G\rho}}$ (Jeans, 1902).

2.6 Spherical Collapse

As gravity is attractive force, ambient matter falls into such high density regions, which results in formation of halos. The spherical collapse model (Gunn & Gott, 1972) provides a simplified description of the formation of cosmic structures by considering the evolution of a spherically symmetric overdensity in an expanding universe. Suppose that there is spherical matter around a certain point in the Universe and initial density contrast is denoted as $\delta_i \ll 1$. The equation of motion of the shell which the radius R is given by:

$$\ddot{R} = -\frac{GM(< R)}{R^2}, \quad (2.63)$$

where $M(< R)$ is the mass enclosed within the radius R . Multiplying both sides by \dot{R} and integrating over time, we get:

$$\dot{R}^2 = \frac{2GM(< R)}{R} + E. \quad (2.64)$$

The constant E corresponds to the energy, $E < 0$ for bound systems. From this expression, we can obtain a parametric solution for the radius $R(t)$ in term of θ :

$$R(t) = (GM)^{1/3} A^2 (1 - \cos \theta) \quad (2.65)$$

$$t = A^3 (\theta - \sin \theta) \quad (2.66)$$

where A is a constant. For a matter-dominated universe, the mean density $\bar{\rho} = (6\pi G t^2)^{-1}$. The density contrast within the shell is given by:

$$1 + \delta = \frac{\rho}{\bar{\rho}} = \frac{3M}{4\pi R^3} \frac{6\pi G t^2}{M} = \frac{9}{2} \frac{(\theta - \sin \theta)^2}{(1 - \cos \theta)^3} \quad (2.67)$$

$\theta = \pi$ corresponds to the turnaround point, where the shell reaches its maximum radius and starts collapsing. The density contrast at the turnaround point is given by:

$$\delta_{ta} = \frac{9\pi^2}{16} - 1 \approx 4.55 \quad (2.68)$$

where the corresponding radius R_{ta} and time t_{ta} are:

$$R_{ta} = 2(GM)^{1/3} A^2, \quad t_{ta} = \pi A^3 \quad (2.69)$$

At $\theta = 2\pi$, the shell reaches a singularity where the radius R goes to zero and the density contrast δ diverges. However, in reality, this does not occur because the shell undergoes virialization and forms a halo. We assume the shell virializes at $R = R_{ta}/2$ at time $t = t_{coll}$. The density contrast at virialization is given by:

$$\delta_{coll} = \delta_{ta} \times 4 \times 2^3 = 18\pi^2. \quad (2.70)$$

In the early epoch ($\theta \ll 1$), the density contrast follows the linear theory. If we expand the density contrast and time around $\theta = 0$, we get:

$$\delta = \frac{3}{20}\theta^2 + \mathcal{O}(\theta^4), \quad t = \frac{A^3}{6}\theta^3 + \mathcal{O}(\theta^5) \quad (2.71)$$

This yields $\delta \propto t^{2/3}$, which is consistent with linear theory. Denoting this linear fluctuation as $\delta_L(t)$:

$$\delta_L(t) = \frac{3(6t)^{2/3}}{20A^2} \quad (2.72)$$

Substituting $t = t_{ta}$ and $t = t_{coll}$, we obtain:

$$\delta_L(t_{ta}) = \frac{3(6\pi)^{2/3}}{20} \approx 1.06, \quad \delta_L(t_{coll}) = \frac{3(12\pi)^{2/3}}{20} \approx 1.69. \quad (2.73)$$

Therefore, when the linear density contrast exceeds $\delta_L \approx 1.69$, the shell virializes and forms a halo.

2.7 Dark Matter Halo

Dark matter halos are the fundamental building blocks of cosmic structures. They form through the gravitational collapse of overdense regions in the early universe and provide the potential wells in which baryonic matter accumulates to form galaxies and clusters.

2.7.1 Halo Mass Function

The halo mass function (HMF) describes the number density of dark matter halos as a function of their mass and redshift. The Press-Schechter (PS) formalism ([Press & Schechter, 1974](#)) provides an analytical approach to calculate the HMF based on the initial density field and the theory of gravitational collapse.

Let us consider the density field which follows Gaussian distribution at each position. The probability distribution function is:

$$P(\delta)d\delta = \frac{1}{\sqrt{2\pi\sigma^2}} \exp\left(-\frac{\delta^2}{2\sigma^2}\right) d\delta \quad (2.74)$$

where σ^2 is the variance of the density field. Supposed that the sphere of radius R contains mass $M = \frac{4}{3}\pi R^3 \bar{\rho}$, where $\bar{\rho}$ is the mean density. The density contrast within this sphere is:

$$\delta_M(q, t) = \frac{3}{4\pi} \int_{|q' - q| < R} \delta(q', t) d^3 q' \quad (2.75)$$

This density contrast follows Gaussian distribution. The probability distribution function of the density contrast is:

$$P(\delta_M) = \frac{1}{\sqrt{2\pi\sigma^2(M)}} \exp\left(-\frac{\delta_M^2}{2\sigma^2(M)}\right) \quad (2.76)$$

The halo formation happens when the density contrast exceeds a critical value δ_c . The fraction of Lagaranian volume which collapses to form halos is:

$$P_{>\delta_c} = \int_{\delta_c}^{\infty} P(\delta_M) d\delta_M = \frac{1}{\sqrt{2\pi}} \int_{\delta_c/\sigma(M)}^{\infty} e^{-x^2/2} dx \quad (2.77)$$

Thus, mass which forms dark halo with more than mass M can be calculated as $\bar{\rho}_0 P_{>\delta_c}$. In Press-Schechter formalism, the mass function is given by:

$$n(M) M dM = 2\bar{\rho}_0 \left| \frac{P_{\delta_c}}{d\sigma(M)} \right| \left| \frac{d\sigma(M)}{dM} \right| dM \quad (2.78)$$

Substituting Eq. (2.77) into the above equation, we obtain:

$$n(M) = \sqrt{\frac{2}{\pi}} \frac{\bar{\rho}_0}{M \sigma^2(M)} \left| \frac{d\sigma}{dM} \right| e^{-\delta_c^2/2\sigma^2(M)} \quad (2.79)$$

The mass function can be further simplified by using the relation between the variance of the density field and the linear power spectrum $P(k)$:

$$\sigma^2(M) = \int \frac{d^3k}{(2\pi)^3} P(k) W^2(kR) \quad (2.80)$$

where $W(kR)$ is the Fourier transform of the top-hat window function:

$$\begin{aligned} W(kR) &= \int d^3x e^{ik \cdot x} W_R(x) \\ &= 4\pi \int_0^R x^2 dx \frac{\sin(kx)}{kx} W_R(x) \\ &= \frac{3}{(kR)^3} [\sin(kR) - kR \cos(kR)] \end{aligned} \quad (2.81)$$

Finally, we can construct the Press-Schechter mass function only from the linear power spectrum $P(k)$. In reality, matter collapses into halos non-spherically. One of the most popular extensions of the Press-Schechter formalism is the Sheth-Tormen mass function ([Sheth & Tormen, 1999](#)), which provides a better fit to numerical simulations by incorporating ellipsoidal collapse.

2.7.2 Halo Bias

Halo bias quantifies how dark matter halos are biased tracers of the underlying matter distribution. Massive halos tend to form in regions of higher density contrast, leading to a scale-dependent and mass-dependent bias factor $b(M)$. [Mo & White \(1996\)](#) proposed a simple model for halo bias based on the Press-Schechter formalism and the spherical collapse model. They derive the analytical expression for the linear halo bias, which defined as:

$$b_h(M, z) := \frac{\delta_h(M, z)}{\delta_m} \quad (2.82)$$

where $\delta_h(M, z)$ is the overdensity of halos of mass M at redshift z , and δ_m is the overdensity of the matter field. In the lowest-order approximation, the linear halo bias is given by:

$$b_h(M, z) = 1 + \frac{\nu(M, z)^2 - 1}{\delta_c} \quad (2.83)$$

where $\nu(M, z) = \delta_c/\sigma(M, z)$ is the peak height, and δ_c is the critical density contrast for collapse. It is then extended by [Sheth et al. \(2001\)](#) to include ellipsoidal collapse.

2.7.3 Halo Density Profile

Since halos undergo nonlinear gravitational evolution, their density profiles need numerical simulations to be determined. The most widely used model is the Navarro-Frenk-White (NFW) profile ([Navarro et al., 1996, 1997](#)), which is found universally in numerical simulations. The NFW profile is given by:

$$\rho_{\text{NFW}}(r) = \frac{\rho_s}{(r/r_s)(1+r/r_s)^2} \quad (2.84)$$

where ρ_s and r_s are the characteristic density and scale radius, respectively. At large radii, the NFW profile follows a power-law behavior $\rho_{\text{NFW}} \propto r^{-3}$, while at small radii, it behaves as $\rho_{\text{NFW}} \propto r^{-1}$. The enclosed mass is not well defined for the NFW profile, so the virial radius r_{vir} and r_{200c} , which encloses a density contrast of 200 times the critical density, are used instead.

After specifying the boundary, one can compute the halo mass as ([Oguri & Hamana, 2011](#)):

$$M_{\text{vir}} = 4\pi r_s^3 \rho_s m(c_{\text{vir}}) \quad (2.85)$$

with

$$m(c) = \int_0^c \frac{x dx}{(1+x)^2} = \ln(1+c) - \frac{c}{1+c} \quad (2.86)$$

where $c_{\text{vir}} = r_{\text{vir}}/r_s$ is the concentration parameter.

Another widely used profile is the Einasto profile ([Einasto, 1965](#)), which provides a better fit to numerical simulations at small radii. The Einasto profile is given by:

$$\rho_{\text{Ein}}(r) = \rho_s \exp\left(-\frac{2}{\alpha} \left[\left(\frac{r}{r_s}\right)^\alpha - 1\right]\right) \quad (2.87)$$

where ρ_s and r_s are the characteristic density and scale radius, respectively, and α is the shape parameter.

Chapter 3

Weak Lensing

Contents

3.1	Lens Equation	25
3.2	Convergence	29
3.3	Shear	30
3.4	Estimation of Lensing Fields	31

Weak gravitational lensing (WL), also known as cosmic shear, refers to the subtle distortions in the images of distant source caused by the gravitational fields of intervening mass distributions. Unlike strong lensing, which produces noticeable effects such as multiple images or arcs, weak lensing induces small, coherent distortions that require statistical analysis to detect and interpret. For the standard approach to lensing, we refer to [Schneider et al. \(1992\)](#), [Bartelmann & Schneider \(2001\)](#) and [Bartelmann \(2010\)](#).

3.1 Lens Equation

3.1.1 Derivation

To derive the lens equation, we consider a perturbed FLRW metric, which incorporates gravitational potential perturbations. The metric is expressed as

$$ds^2 = - \left(1 + \frac{2\Phi}{c^2}\right) c^2 dt^2 + a^2(t) \left(1 - \frac{2\Psi}{c^2}\right) [d\chi^2 + f_K^2(\chi) \omega_{ab} dx^a dx^b] \quad (a, b = 2, 3), \quad (3.1)$$

where the angular part of the metric is defined by

$$\omega_{ab} dx^a dx^b := d\theta^2 + \sin^2 \theta d\phi^2. \quad (3.2)$$

In this context, Φ and Ψ represent the scalar gravitational potentials, and $f_K(\chi)$ encodes the spatial curvature as previously defined in Eq. (2.18).

The trajectory of light within this spacetime is governed by the geodesic equation, which is given by

$$\frac{d^2x^\mu}{d\lambda^2} + \Gamma_{\alpha\beta}^\mu \frac{dx^\alpha}{d\lambda} \frac{dx^\beta}{d\lambda} = 0, \quad (3.3)$$

where λ is an affine parameter and $\Gamma_{\alpha\beta}^\mu$ are the Christoffel symbols corresponding to the metric in Equation (3.1).

To facilitate the derivation, we reparametrize the geodesic equation by substituting the affine parameter λ with the comoving radial distance χ . Applying the chain rule, the geodesic equation transforms to

$$\frac{d^2x^\mu}{d\chi^2} + \Gamma_{\alpha\beta}^\mu \frac{dx^\alpha}{d\chi} \frac{dx^\beta}{d\chi} - \frac{d^2\lambda}{d\chi^2} \left(\frac{d\lambda}{d\chi} \right)^{-1} \frac{dx^\mu}{d\chi} = 0. \quad (3.4)$$

Setting $\mu = 1$ (where $x^1 = \chi$) in Equation (3.4) and simplifying, we obtain

$$\frac{d^2x^\mu}{d\chi^2} + (\Gamma_{\alpha\beta}^\mu - \Gamma_{\alpha\beta}^1) \frac{dx^\alpha}{d\chi} \frac{dx^\beta}{d\chi} = 0. \quad (3.5)$$

The evaluation of Equation (3.5) requires the computation of the Christoffel symbols. Additionally, the derivative $c dt/d\chi$ is derived from the null condition

$$g_{\mu\nu} \frac{dx^\mu}{d\chi} \frac{dx^\nu}{d\chi} = 0, \quad (3.6)$$

yielding

$$\frac{c dt}{d\chi} = -a(t) \left[1 - \frac{\Phi}{c^2} - \frac{\Psi}{c^2} + \frac{f_K^2(\chi)}{2} \omega_{ab} \frac{dx^a}{d\chi} \frac{dx^b}{d\chi} \right], \quad (3.7)$$

valid to first order in Φ and second order in $dx^a/d\chi$. Notably, for the evaluation of Equation (3.5), only the zeroth-order term $c dt/d\chi = -a(t)$ is required. However, the inclusion of perturbative terms in Equation (3.7) is essential for subsequent derivations of the lens equation.

Focusing on the angular components ($\mu = a$) of Equation (3.5), we derive the following differential equation:

$$\frac{d^2x^a}{d\chi^2} + 2 \frac{f'_K(\chi)}{f_K(\chi)} \frac{dx^a}{d\chi} + \omega_{ab} \frac{\Phi_b + \Psi_b}{c^2 f_K^2(\chi)} = 0, \quad (3.8)$$

where Φ_b and Ψ_b denote the derivatives of the gravitational potentials with respect to the angular

coordinates x^a . Integrating Equation (3.8) twice with respect to χ , we obtain

$$\begin{aligned} x^a(\chi_s) - x^a(0) &= -\frac{1}{c^2} \int_0^{\chi_s} d\chi' \int_0^{\chi'} d\chi \omega_{ab} [\Phi_b(\chi, \theta(\chi)) + \Psi_b(\chi, \theta(\chi))] \\ &= -\frac{1}{c^2} \int_0^{\chi_s} d\chi \omega_{ab} [\Phi_b(\chi, \theta(\chi)) + \Psi_b(\chi, \theta(\chi))] \int_\chi^{\chi_s} d\chi' \frac{1}{f_K^2(\chi')} \\ &= -\frac{1}{c^2} \int_0^{\chi_s} d\chi \omega_{ab} [\Phi_b(\chi, \theta(\chi)) + \Psi_b(\chi, \theta(\chi))] \frac{f_K(\chi_s - \chi)}{f_K(\chi_s) f_K(\chi)}, \end{aligned} \quad (3.9)$$

where χ_s denotes the comoving radial distance to the source, and $x^a(0)$ is the angular position at the observer's location. Defining $(\nabla_\theta)^a = \omega^{ab} \partial_b$, the angular position of the source galaxy β is related to the observed angular position θ by

$$\theta(\chi_s) = \theta(0) - \frac{1}{c^2} \int_0^{\chi_s} d\chi \nabla_\theta [\Phi(\chi, \theta(\chi)) + \Psi(\chi, \theta(\chi))] \frac{f_K(\chi_s - \chi)}{f_K(\chi_s) f_K(\chi)}. \quad (3.10)$$

Applying the Born approximation (Born, 1926), and assume that $\Phi = \Psi$, we can simplify the lens equation to:

$$\theta(\chi_s) = \theta(0) - \frac{2}{c^2} \int_0^{\chi_s} d\chi \nabla_\theta [\Phi(\chi, \theta(0))] \frac{f_K(\chi_s - \chi)}{f_K(\chi_s) f_K(\chi)}. \quad (3.11)$$

This final expression constitutes the lens equation, encapsulating the deflection of light due to the gravitational potentials Φ and Ψ along the line of sight.

3.1.2 Lensing Matrix

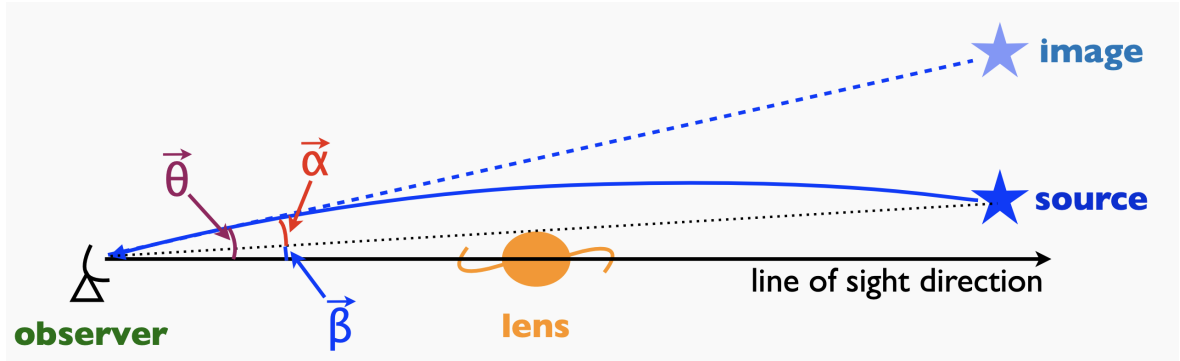


Figure 3.1: Schematic representation of the lensing geometry. The source is located at β , while the observed image is at θ . The deflection angle α is the difference between the observed and true angular positions.

Redefining the notation in Eq. (3.11) and considering the angular position of the source $\beta = \theta(\chi_s)$ and the observed angular position $\theta = \theta(0)$ (see Fig. 3.1), we can express the lens equation as (Bartelmann & Schneider, 2001; Hilbert et al., 2009; Kilbinger, 2015):

$$\beta = \theta - \alpha(\theta), \quad (3.12)$$

where the deflection angle $\alpha(\theta)$ is defined by:

$$\alpha(\theta) = \nabla_\theta \psi(\theta), \quad \psi(\theta) = \frac{2}{c^2} \int_0^{\chi_s} d\chi \frac{f_K(\chi_s - \chi)}{f_K(\chi_s) f_K(\chi)} \Phi(f_K(\chi)\theta, \chi). \quad (3.13)$$

The mapping between the source plane and the image plane can be described by the Jacobian matrix \mathcal{A} , which relates infinitesimal displacements in the source position to displacements in the image position:

$$\mathcal{A} := \frac{\partial \beta}{\partial \theta} = \begin{pmatrix} 1 - \kappa - \gamma_1 & -\gamma_2 \\ -\gamma_2 & 1 - \kappa + \gamma_1 \end{pmatrix} = (1 - \kappa) \begin{pmatrix} 1 & 0 \\ 0 & 1 \end{pmatrix} - |\gamma| \begin{pmatrix} \cos 2\phi & \sin 2\phi \\ \sin 2\phi & -\cos 2\phi \end{pmatrix}, \quad (3.14)$$

where κ is the convergence and $\gamma = \gamma_1 + i\gamma_2 = |\gamma|e^{2i\phi}$ is the shear. The quantities κ and γ will be discussed in detail in the subsequent sections. Figure 3.2 illustrates the effects of gravitational lensing on the shapes of background sources through the lensing matrix \mathcal{A} . The panels demonstrate how the combined effects of convergence and shear components in the Jacobian matrix \mathcal{A} lead to complex distortions of background sources.

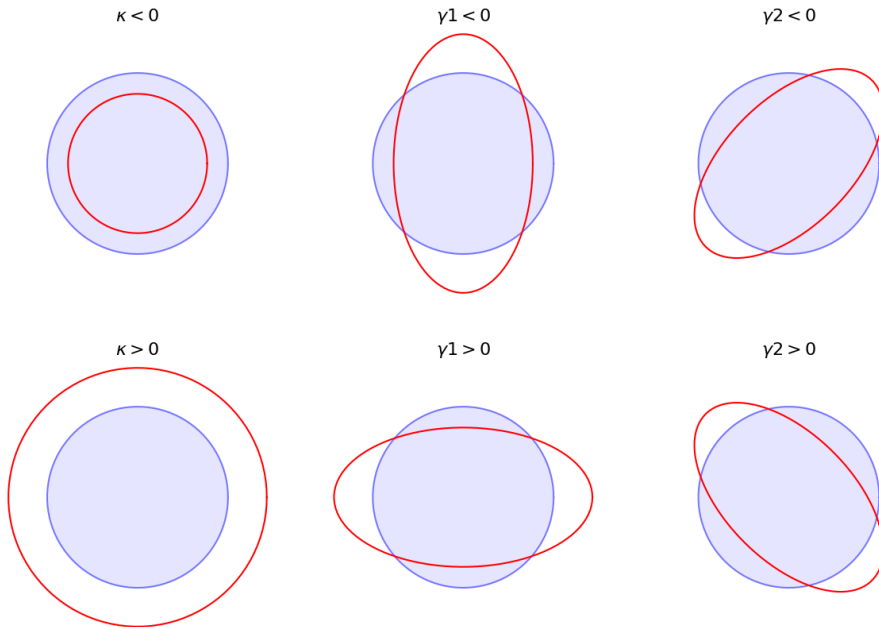


Figure 3.2: Illustration of the distortion of background sources due to gravitational lensing. The left panel depict the effect of the convergence κ and the middle and right panels show the components of the shear $\gamma = \gamma_1 + i\gamma_2$ on circular background sources. Positive and negative values of κ cause isotropic magnification or demagnification, while γ_1 and γ_2 introduce anisotropic distortions, stretching the sources along or at an angle to the principal axes.

3.2 Convergence

3.2.1 Definition

From the lensing matrix in Eq. (3.14), the convergence κ is defined as:

$$\kappa(\theta) := \frac{1}{2} \left(\frac{\partial^2 \psi}{\partial \theta_1^2} + \frac{\partial^2 \psi}{\partial \theta_2^2} \right) = \frac{1}{2} \nabla_\theta^2 \psi(\theta) \quad (3.15)$$

with θ_1 and θ_2 representing the angular coordinates on the sky. In Fourier space, the convergence field could be expressed as:

$$\tilde{\kappa}(\ell) = \int d^2\theta e^{-i\ell\cdot\theta} \kappa(\theta) = \frac{1}{2} \ell^2 \tilde{\psi}(\ell), \quad (3.16)$$

where $(\tilde{})$ denotes the Fourier transform of the corresponding quantity and $\ell = |\ell|$ is the Fourier counterpart to the angular position θ .

3.2.2 Convergence from Density Contrast

In a flat universe, the Poisson equation in comoving coordinates is expressed as

$$\begin{aligned} \nabla_{\mathbf{x}}^2 \Phi(\mathbf{x}, \chi) &= 4\pi G a^2(\chi) \bar{\rho}_m(\chi) \delta(\mathbf{x}, \chi) \\ &= 4\pi G a^2(\chi) \left[\frac{3H_0^2 \Omega_m}{8\pi G} a^{-3}(\chi) \right] \delta(\mathbf{x}, \chi) \\ &= \frac{3}{2} \Omega_m H_0^2 a^{-1}(\chi) \delta(\mathbf{x}, \chi), \end{aligned} \quad (3.17)$$

where we utilized Eq. (2.35) and Eq. (2.27). Substituting the expression for Φ from Eq. (3.17) into the lensing potential (Eq. (3.13)) and subsequently into the convergence (Eq. (3.15)), we derive:

$$\begin{aligned} \kappa(\theta) &= \frac{1}{c^2} \int_0^{\chi_s} d\chi \frac{f_K(\chi_s - \chi)}{f_K(\chi_s) f_K(\chi)} \left[\frac{1}{f_K^2(\chi)} \nabla_{\mathbf{x}}^2 \Phi(\mathbf{x}, \chi) \right] \\ &= \int_0^{\chi_s} d\chi \frac{3\Omega_m H_0^2}{2c^2} \frac{f_K(\chi_s - \chi) f_K(\chi)}{f_K(\chi_s)} \frac{a^{-1}(\chi)}{f_K^3(\chi)} \delta(\mathbf{x}, \chi) \\ &= \int_0^{\chi_s} d\chi W(\chi, \chi_s) \delta(\mathbf{x}, \chi), \end{aligned} \quad (3.18)$$

where the lensing efficiency function $W(\chi, \chi_s)$ is defined by:

$$W(\chi, \chi_s) := \frac{3\Omega_m H_0^2}{2c^2} \frac{f_K(\chi) f_K(\chi_s - \chi)}{f_K(\chi_s)} \frac{a^{-1}(\chi)}{f_K^2(\chi)}. \quad (3.19)$$

In a flat universe ($f_K(\chi) = \chi$), this simplifies to:

$$W(\chi, \chi_s) = \frac{3\Omega_m H_0^2}{2c^2} a^{-1}(\chi) \frac{\chi(\chi_s - \chi)}{\chi_s}. \quad (3.20)$$

3.3 Shear

The shear γ encapsulates the anisotropic stretching of galaxy images induced by gravitational lensing. Unlike convergence, which affects the size and brightness of images isotropically, shear induces distortions that alter the shapes of background galaxies coherently.

3.3.1 Definition

The shear components γ_1 and γ_2 describe distortions along different axes and are related to the lensing potential ψ by:

$$\gamma_1 := \frac{1}{2} \left(\frac{\partial^2 \psi}{\partial \theta_1^2} - \frac{\partial^2 \psi}{\partial \theta_2^2} \right), \quad \gamma_2 := \frac{\partial^2 \psi}{\partial \theta_1 \partial \theta_2}. \quad (3.21)$$

In Fourier space, the shear field can be expressed as:

$$\tilde{\gamma}_1(\ell) = \frac{1}{2} (\ell_1^2 - \ell_2^2) \tilde{\psi}(\ell) \quad \tilde{\gamma}_2(\ell) = \ell_1 \ell_2 \tilde{\psi}(\ell), \quad (3.22)$$

where $\tilde{\gamma}_1(\ell)$ and $\tilde{\gamma}_2(\ell)$ are the Fourier transforms of $\gamma_1(\theta)$ and $\gamma_2(\theta)$, respectively. Similar as Eq. (3.14), the shear field can be expressed in complex form as:

$$\tilde{\gamma}(\ell) := \tilde{\gamma}_1 + i\tilde{\gamma}_2 = |\tilde{\gamma}(\ell)| e^{2i\phi_\ell}, \quad \tan(2\phi_\ell) = \tilde{\gamma}_2/\tilde{\gamma}_1. \quad (3.23)$$

Therefore, the shear field in Fourier space is directly related to the convergence field combining Eq.(3.16) and Eq.(3.22):

$$\tilde{\kappa}(\ell) = \frac{\ell_1^2 - \ell_2^2 + 2i\ell_1\ell_2}{\ell^2} \tilde{\gamma}(\ell). \quad (3.24)$$

3.3.2 E-mode and B-mode

The shear field can be decomposed into two distinct modes: the **E-mode** (gradient component) and the **B-mode** (curl component). By rotating the complex shear field to align with the principal axes of the shear $\tilde{\gamma}_{EB} = e^{-2i\phi_\ell} \tilde{\gamma}$, we can express the shear field in terms of the E-mode and B-mode components:

$$\begin{pmatrix} \tilde{\gamma}_E \\ \tilde{\gamma}_B \end{pmatrix} := \begin{pmatrix} \cos 2\phi_\ell & \sin 2\phi_\ell \\ -\sin 2\phi_\ell & \cos 2\phi_\ell \end{pmatrix} \begin{pmatrix} \tilde{\gamma}_1 \\ \tilde{\gamma}_2 \end{pmatrix} \quad (3.25)$$

where $\tilde{\gamma}_E$ and $\tilde{\gamma}_B$ are the E-mode and B-mode components of the shear, respectively. The E-mode represents the gradient component of the shear field, while the B-mode describes the curl component.

For standard gravitational lensing by density fluctuations, the B-mode component $\tilde{\gamma}_B(\ell)$ is expected to vanish in the absence of systematics or additional physical effects. This implies that all the shear signal is contained within the E-mode such that:

$$\tilde{\gamma}_E(\ell) = \tilde{\kappa}(\ell), \quad \tilde{\gamma}_B(\ell) = 0. \quad (3.26)$$

3.4 Estimation of Lensing Fields

In the case of cosmic shear, not the convergence but the shear is measured from the observed galaxy shapes. Theoretical predictions of the convergence can be related to the observed shear using the relationship in Eq. (3.24). Here, we introduce a concept of the reduced shear. Furthermore, a convergence field can be estimated from the observed galaxy shapes (Kaiser & Squires, 1993) and can be estimated from magnification (Bartelmann & Schneider, 2001).

3.4.1 Ellipticity and Reduced Shear

To quantify the shapes of galaxies, we use the second moments of their surface brightness distributions $I(\theta)$. For each galaxy, the second moments Q_{ab} are defined as (Bartelmann & Schneider, 2001):

$$Q_{ab} := \frac{\int d^2\theta I(\theta)\theta_a\theta_b}{\int d^2\theta I(\theta)}, \quad (3.27)$$

where $\theta = (\theta_1, \theta_2)$ is the angular position relative to the galaxy center. The complex ellipticity ϵ of the galaxy is then defined as:

$$\epsilon := \frac{Q_{11} - Q_{22} + 2iQ_{12}}{Q_{11} + Q_{22}}. \quad (3.28)$$

Gravitational lensing transforms the image of a source galaxy via the Jacobian matrix A (see Eq. (3.14)). Assuming that the surface brightness is conserved during lensing, $I^{(s)}(\beta) = I(\theta)$, the second moments in the source plane $Q_{ab}^{(s)}$ are related to those in the image plane by:

$$Q_{ab}^{(s)} = \frac{\int d^2\beta I^{(s)}(\beta)\beta_a\beta_b}{\int d^2\beta I^{(s)}(\beta)} \approx A_{ac}A_{bd}Q_{cd}, \quad (3.29)$$

where we have approximated the size of the galaxy as sufficiently small so that the lensing distortion is constant across the galaxy image.

By expanding the components of $Q_{ab}^{(s)}$ and performing straightforward calculations (see Schneider et al. 1992 for details), we find that the intrinsic ellipticity $\epsilon^{(s)}$ is related to the observed ellipticity ϵ through:

$$\epsilon^{(s)} = \frac{(1-\kappa)^2\epsilon - 2(1-\kappa)\gamma + \gamma^2\epsilon^*}{(1-\kappa)^2 + |\gamma|^2 - 2(1-\kappa)\text{Re}[\gamma\epsilon^*]}, \quad (3.30)$$

where ϵ^* denotes the complex conjugate of ϵ , and Re denotes the real part.

Introducing the *reduced shear* $g = \gamma/(1 - \kappa)$, the above equation simplifies to (Schneider & Seitz, 1995):

$$\epsilon^{(s)} = \frac{\epsilon - 2g + g^2\epsilon^*}{1 + |g|^2 - 2\text{Re}[g\epsilon^*]}. \quad (3.31)$$

This relation indicates that weak lensing measurements are sensitive to the reduced shear g rather than the shear γ directly. In the weak lensing regime, where $|\kappa|, |\gamma| \ll 1$, and assuming that the intrinsic ellipticities of galaxies are randomly oriented (i.e., $\langle \epsilon^{(s)} \rangle = 0$), the observed ellipticity becomes an unbiased estimator of the reduced shear:

$$\langle \epsilon \rangle \approx g \approx \gamma. \quad (3.32)$$

However, in the weak-lensing regime, the shear cannot be detected from an individual galaxy due to the dominance of intrinsic shape noise. The typical root mean square (rms) of the intrinsic ellipticity is $\sigma_\epsilon \approx 0.26$ (Euclid Collaboration et al., 2019), which necessitates averaging over a large number of galaxies to measure the shear signal accurately. The noise for the reduced shear estimator is dominated by Poisson noise, which is given by:

$$\sigma_\gamma = \frac{\sigma_\epsilon}{\sqrt{N}}, \quad (3.33)$$

where N is the number of galaxies used in the shear estimation. It is known that the following transformation of convergence does not change the reduced shear,

$$\kappa' = \lambda\kappa + (1 - \lambda), \quad (3.34)$$

where λ is a arbitrary constant. This degree of freedom in the convergence field is known as the mass-sheet degeneracy (Falco et al., 1985).

3.4.2 From Shear to Convergence

As we have seen in Eq. (3.24), shear and convergence are related through the Fourier transform. Following Kaiser & Squires (1993), the relation between the shear and convergence fields in real space can be expressed as:

$$\gamma(\theta) = \frac{1}{\pi} \int d^2\theta' \mathcal{D}(\theta - \theta') \kappa(\theta'), \quad (3.35)$$

where $\mathcal{D}(\theta)$ is a kernel function defined by:

$$\mathcal{D}(\theta) = -\frac{\theta_1^2 - \theta_2^2 + 2i\theta_1\theta_2}{\theta^4} = -\frac{1}{(\theta_1 - i\theta_2)^2}. \quad (3.36)$$

Therefore, the convolution with the kernel function in Fourier space yields:

$$\tilde{\gamma}(\ell) = \frac{1}{\pi} \tilde{\mathcal{D}}(\ell) \tilde{\kappa}(\ell), \quad (3.37)$$

The Fourier transform of the kernel function, $\tilde{\mathcal{D}}(\ell)$, is given by:

$$\tilde{\mathcal{D}}(\ell) = \pi \frac{\ell_1^2 - \ell_2^2 + 2i\ell_1\ell_2}{\ell^2} \quad (3.38)$$

It is notable that this kernel function and its conjugate satisfies:

$$\tilde{\mathcal{D}}(\ell) \tilde{\mathcal{D}}^*(\ell) = \pi^2 \left(\frac{\ell_1^2 - \ell_2^2 + 2i\ell_1\ell_2}{\ell^2} \right) \left(\frac{\ell_1^2 - \ell_2^2 - 2i\ell_1\ell_2}{\ell^2} \right) = \pi^2. \quad (3.39)$$

Substituting the expression for $\tilde{\mathcal{D}}(\ell)$ into the relation between the shear and convergence fields, we find:

$$\tilde{\kappa}(\ell) = \frac{1}{\pi} \tilde{\gamma}(\ell) \tilde{\mathcal{D}}^*(\ell). \quad (3.40)$$

$$\kappa(\theta) = \kappa_0 + \frac{1}{\pi} \int d^2\theta' \mathcal{D}^*(\theta - \theta') \gamma(\theta'). \quad (3.41)$$

The constant term κ_0 arises from the unknown $\ell = 0$ mode in the Fourier space, which is not constrained by the observed shear field.

Chapter 4

Statistics

Contents

4.1	Convergence Power Spectrum	34
4.2	Convergence Bispectrum	37
4.3	Probability Density Functions	38
4.4	Peak and Minimum Counts	39
4.5	Minkowski Functionals	41

4.1 Convergence Power Spectrum

The matter power spectrum, $P(k)$, is a fundamental quantity in cosmology that characterizes the distribution of dark matter density fluctuations in Fourier space. It is defined as the Fourier transform of the two-point correlation function of the dark matter density field, $\delta(\mathbf{x})$ ([Bartelmann & Schneider, 2001](#)). Mathematically, the matter power spectrum is expressed as:

$$\langle \tilde{\delta}(\mathbf{k})\tilde{\delta}(\mathbf{k}') \rangle = (2\pi)^3 \delta^{(3)}(\mathbf{k} + \mathbf{k}') P(k), \quad (4.1)$$

where $\tilde{\delta}(\mathbf{k})$ represents the Fourier transform of the density contrast $\delta(\mathbf{x})$, and $\delta^{(3)}$ is the three-dimensional Dirac delta function ensuring statistical isotropy and homogeneity.

In the context of weak gravitational lensing, the matter power spectrum $P(k)$ is not directly observable. Instead, observations yield the angular power spectrum of the convergence field, $C_\ell^{\kappa\kappa}$, which encapsulates the statistical properties of the convergence $\kappa(\theta)$ across the sky ([Bartelmann & Schneider, 2001](#)). The convergence power spectrum, $P_\kappa(\ell)$, is defined through the relation:

$$\langle \tilde{\kappa}(\ell)\tilde{\kappa}(\ell') \rangle = (2\pi)^2 \delta^{(2)}(\ell + \ell') P_\kappa(\ell), \quad (4.2)$$

where $\tilde{\kappa}(\ell)$ is the Fourier transform of the convergence field $\kappa(\theta)$, and $\delta^{(2)}$ is the two-dimensional

Dirac delta function.

The convergence field $\kappa(\theta)$ can be expressed as a weighted projection of the matter density contrast along the line of sight (see Eq. (3.18)):

$$\kappa(\theta) = \int_0^{\chi_s} d\chi W(\chi) \delta_m(\chi\theta, \chi), \quad (4.3)$$

where $W(\chi)$ is the lensing kernel, χ is the comoving radial distance.

Recognizing the Fourier transform of the matter density field $\delta_m(\chi\theta, \chi)$, we write:

$$\delta_m(\chi\theta, \chi) = \int \frac{d^3\mathbf{k}}{(2\pi)^3} \tilde{\delta}(\mathbf{k}) e^{i\mathbf{k}\cdot\mathbf{x}}, \quad (4.4)$$

where $\mathbf{x} = (\chi\theta, \chi)$ is the comoving position vector. Substituting this into the Fourier transform of the convergence field $\tilde{\kappa}(\ell)$, we obtain:

$$\begin{aligned} \tilde{\kappa}(\ell) &= \int_0^{\chi_s} d\chi W(\chi) \int d\theta e^{-i\ell\cdot\theta} \delta_m(\chi\theta, \chi) \\ &= \int_0^{\chi_s} d\chi W(\chi) \int \frac{d^3\mathbf{k}}{(2\pi)^3} \tilde{\delta}(\mathbf{k}) e^{ik_{\parallel}\chi} \int d\theta e^{-i\ell\cdot\theta} e^{i\chi\mathbf{k}_{\perp}\cdot\theta} \\ &= \int_0^{\chi_s} d\chi W(\chi) \int \frac{dk_{\parallel}}{2\pi} \frac{d^2\mathbf{k}_{\perp}}{(2\pi)^2} \tilde{\delta}_m(k_{\parallel}, \mathbf{k}_{\perp}) e^{ik_{\parallel}\chi} \int d\theta e^{-i(\ell-\chi\mathbf{k}_{\perp})\cdot\theta} \\ &= \int_0^{\chi_s} d\chi \frac{W(\chi)}{\chi^2} \int \frac{dk_{\parallel}}{2\pi} \tilde{\delta}_m\left(k_{\parallel}, \frac{\ell}{\chi}\right) e^{ik_{\parallel}\chi}, \end{aligned} \quad (4.5)$$

where \mathbf{k}_{\perp} and k_{\parallel} are the components of \mathbf{k} perpendicular and parallel to the line of sight, respectively.

Next, we compute the ensemble average of the Fourier transform of the convergence field:

$$\begin{aligned} \langle \tilde{\kappa}(\ell)\tilde{\kappa}(\ell') \rangle &= \int_0^{\chi_s} d\chi \frac{W(\chi)}{\chi^2} \int_0^{\chi_s} d\chi' \frac{W(\chi')}{\chi'^2} \int \frac{dk_{\parallel}}{2\pi} \int \frac{dk'_{\parallel}}{2\pi} \\ &\quad \times \langle \tilde{\delta}_m\left(k_{\parallel}, \frac{\ell}{\chi}\right) \tilde{\delta}_m\left(k'_{\parallel}, \frac{\ell'}{\chi'}\right) \rangle e^{ik_{\parallel}\chi} e^{ik'_{\parallel}\chi'} \\ &= \int_0^{\chi_s} d\chi \frac{W(\chi)}{\chi^2} \int_0^{\chi_s} d\chi' \frac{W(\chi')}{\chi'^2} \int \frac{dk_{\parallel}}{2\pi} e^{ik_{\parallel}(\chi-\chi')} \\ &\quad \times (2\pi)^2 \delta^{(2)}\left(\frac{\ell}{\chi} + \frac{\ell'}{\chi'}\right) P_m\left(\sqrt{k_{\parallel}^2 + \frac{\ell^2}{\chi^2}}\right) \end{aligned}$$

where in the last step we have applied the Limber approximation (Limber, 1954), which assumes $k_{\parallel} \ll \ell/\chi$. Under the Limber approximation, the integral simplifies as:

$$\int \frac{dk_{\parallel}}{2\pi} e^{ik_{\parallel}(\chi-\chi')} P_m\left(\sqrt{k_{\parallel}^2 + \frac{\ell^2}{\chi^2}}\right) \approx P_m\left(\frac{\ell}{\chi}\right) \delta(\chi - \chi'), \quad (4.6)$$

where $P_m(k)$ is evaluated at $k = \ell/\chi$. Substituting this into Eq. (4.6), we obtain:

$$\langle \tilde{\kappa}(\ell) \tilde{\kappa}(\ell') \rangle = (2\pi)^2 \delta^{(2)}(\ell + \ell') \int_0^{\chi_s} d\chi \frac{W^2(\chi)}{\chi^2} P_m\left(\frac{\ell}{\chi}; \chi\right), \quad (4.7)$$

where $P_m\left(\frac{\ell}{\chi}; \chi\right)$ denotes the matter power spectrum evaluated at wavenumber $k = \ell/\chi$ and at the comoving distance χ . Finally, equating this result with the definition of the convergence power spectrum in Eq. (4.2), we derive the expression for $C_\ell^{\kappa\kappa}$:

$$C_\ell^{\kappa\kappa} = \int_0^{\chi_s} d\chi \frac{W^2(\chi)}{\chi^2} P_m\left(\frac{\ell}{\chi}; \chi\right). \quad (4.8)$$

This relation demonstrates how the observable convergence power spectrum $C_\ell^{\kappa\kappa}$ is sourced by the underlying matter power spectrum $P_m(k; \chi)$ integrated along the line of sight.

4.1.1 Halofit Model

Based on the halo models (discussed in Sec. 2.7), Halofit model is a widely used prescription to compute the non-linear matter power spectrum $P(k)$ from the linear power spectrum $P_L(k)$ (Smith et al., 2003; Takahashi et al., 2012). In the Halofit regime, the power spectrum consists of two terms:

$$P(k) = P_{1h}(k) + P_{2h}(k), \quad (4.9)$$

where the two-halo term $P_{2h}(k)$ captures the contribution from large-scale linear structures, given by:

$$P_{2h}(k) = P_L(k) \left[\frac{1}{\bar{\rho}} \int dM b(M) n(M) \tilde{\rho}(k, M) \right]^2, \quad (4.10)$$

and one-halo term $P_{1h}(k)$ accounts for the contribution from small-scale non-linear structures, defined as:

$$P_{1h}(k) = \frac{1}{\bar{\rho}^2 (2\pi)^3} \int dM n(M) |\tilde{\rho}(k, M)|^2. \quad (4.11)$$

Here, $\bar{\rho}$ is the mean matter density, $n(M)dM$ is the halo mass function, $b(M)$ is the halo bias, and $\tilde{\rho}(k, M)$ is the Fourier transform of the halo density profile. Those two terms are then approximated into empirical fitting formulae and calibrated against N -body simulations.

The one-halo term resembles a shot noise spectrum on large scales but is progressively reduced on small scales due to the filtering effects of halo profiles and the mass function. Conversely, the two-halo term modifies the relative correlations of halos beyond what is predicted by linear theory and becomes negligible on small scales.

4.2 Convergence Bispectrum

The bispectrum, $B(k)$, serves as the Fourier counterpart to the three-point correlation function and is the lowest-order statistical quantity capable of characterizing non-Gaussianity in the matter distribution (Bernardeau et al., 2002). While the power spectrum effectively captures Gaussian fluctuations through two-point statistics, the bispectrum provides deeper insights by incorporating three-point correlations, thereby unveiling more complex structures in the cosmic density field (Scoccimarro et al., 1999; Takada & Jain, 2004).

Analogous to the angular power spectrum, the convergence bispectrum can be expressed as the ensemble average of three Fourier-transformed convergence modes, $\tilde{\kappa}$ (Dodelson & Zhang, 2005):

$$\langle \tilde{\kappa}(\mathbf{l}_1) \tilde{\kappa}(\mathbf{l}_2) \tilde{\kappa}(\mathbf{l}_3) \rangle = (2\pi)^2 \delta_D(\mathbf{l}_1 + \mathbf{l}_2 + \mathbf{l}_3) B_{\ell_1 \ell_2 \ell_3}^{\kappa}, \quad (4.12)$$

Building upon the derivations analogous to Equations (4.5) through (4.7), the convergence bispectrum can be expressed as:

$$B_{\ell_1 \ell_2 \ell_3}^{\kappa} = \int_0^{\chi_s} d\chi \frac{W^3(\chi)}{\chi^4} B_m \left(\frac{\ell_1}{\chi}, \frac{\ell_2}{\chi}, \frac{\ell_3}{\chi}; \chi \right), \quad (4.13)$$

where $B_m(k_1, k_2, k_3, z)$ denotes the matter bispectrum at redshift z , and $W(\chi)$ is the lensing kernel.

The bispectrum depends not only on the magnitudes of the wavevectors but also on the shapes formed by the triplet (k_1, k_2, k_3) , constrained by the condition $k_1 + k_2 + k_3 = 0$. Different triangle configurations (e.g. equilateral, squeezed, isoceles) probe different physical processes and scales in the Universe (Dodelson & Zhang, 2005).

4.2.1 BiHalofit Model

The BiHalofit model (Takahashi et al., 2020) extends the Halofit prescription to compute the non-linear matter bispectrum $B_m(k_1, k_2, k_3)$ from the linear matter power spectrum $P_L(k)$. The bispectrum is decomposed into one-halo and three-halo terms, given by:

$$B_m(k_1, k_2, k_3) = B_{1h}(k_1, k_2, k_3) + B_{3h}(k_1, k_2, k_3), \quad (4.14)$$

The one-halo term describes the correlation in an individual halo, and the three-halo term captures the correlation between three different halos. Because the two-halo term is subdominant in most of the triangle configurations (except at the squeezed limit; Valageas & Nishimichi 2011), it is neglected in the BiHalofit model.

The one-halo term is given by:

$$B_{1h}(k_1, k_2, k_3) = \int dM \frac{dn(M)}{dM} \left(\frac{M}{\bar{\rho}} \right)^3 u(k_1; M) u(k_2; M) u(k_3; M) \quad (4.15)$$

where $u(k; M)$ is the Fourier transform of the scaled halo density profile $\rho(r; M)/M$. The three-halo term is given by:

$$B_{3h}(k_1, k_2, k_3) = 2 \left[F_2(k_1, k_2) + \frac{I_1^2(k_3)}{2I_1^1(k_3)} \right] I_1^1(k_1) I_1^1(k_2) I_1^1(k_3) P_L(k_1) P_L(k_2) + 2 \text{ perm.} \quad (4.16)$$

with

$$I_1^\beta(k) = \int dM \frac{dn(M)}{dM} \frac{M}{\bar{\rho}} b_\beta(M) u(k; M) \quad (4.17)$$

and

$$F_2(k_1, k_2) = \frac{5}{7} + \frac{1}{2} \left(\frac{k_1}{k_2} + \frac{k_2}{k_1} \right) \mu_{12} + \frac{2}{7} \mu_{12}^2 \quad (4.18)$$

which is given at the tree level (leading order) in perturbation theory (Bernardeau et al., 2002).

4.3 Probability Density Functions

The Probability Density Function (PDF) of the convergence field, κ , provides a fundamental statistical characterization of the field's one-point distribution. By encompassing all moments and cumulants, the PDF captures both Gaussian and non-Gaussian features intrinsic to the convergence field.

To effectively suppress noise and small-scale fluctuations, the convergence map $\kappa(\hat{\mathbf{n}})$ is first smoothed with a Gaussian kernel. The smoothed convergence field, $\kappa_{\text{smooth}}(\hat{\mathbf{n}})$, is defined as:

$$\kappa_{\text{smooth}}(\hat{\mathbf{n}}) = \int_{S^2} \kappa(\hat{\mathbf{n}}') W(\hat{\mathbf{n}} - \hat{\mathbf{n}}') d\hat{\mathbf{n}}', \quad (4.19)$$

where $W(\theta)$ is the Gaussian smoothing kernel given by:

$$W(\theta) = \frac{1}{2\pi\sigma_\theta^2} \exp\left(-\frac{\theta^2}{2\sigma_\theta^2}\right), \quad (4.20)$$

with $\theta = \arccos(\hat{\mathbf{n}} \cdot \hat{\mathbf{n}}')$ representing the angular separation between the points $\hat{\mathbf{n}}$ and $\hat{\mathbf{n}}'$ on the unit sphere S^2 , and σ_θ is the smoothing scale. To standardize the statistical analysis, the smoothed convergence values are normalized by their standard deviation. The normalized smoothed convergence, $\tilde{\kappa}_{\text{smooth},i}$, is defined as:

$$\nu_i = \frac{\kappa_{\text{smooth},i} - \langle \kappa_{\text{smooth}} \rangle}{\sigma_{\text{smooth}}}, \quad (4.21)$$

where:

$$\langle \kappa_{\text{smooth}} \rangle = \frac{1}{N_{\text{pix}}} \sum_{i=1}^{N_{\text{pix}}} \kappa_{\text{smooth},i}, \quad \sigma_{\text{smooth}}^2 = \sigma_{\text{signal}}^2 + \sigma_{\text{noise}}^2. \quad (4.22)$$

Formally, the PDF $P(\nu)$ is defined such that:

$$P(\nu) d\nu = \text{Prob}(\nu \leq \nu' \leq \nu + d\nu), \quad (4.23)$$

where Prob denotes the probability that the normalized convergence ν' lies within the interval $[\nu, \nu + d\nu]$.

For a discrete set of normalized convergence measurements $\{\nu_i\}_{i=1}^{N_{\text{pix}}}$ obtained from N_{pix} pixels, the PDF can be represented using the Dirac delta function δ_D :

$$P(\nu) = \frac{1}{N_{\text{pix}}} \sum_{i=1}^{N_{\text{pix}}} \delta_D(\nu - \nu_i). \quad (4.24)$$

This expression effectively constructs the PDF by summing over all pixel values, assigning a weight to each normalized convergence measurement ν_i at its exact value.

In practical applications, however, the Dirac delta function is not computationally feasible. Instead, we approximate the PDF by discretizing the normalized convergence values into bins of finite width $\Delta\nu$. This leads to a binned estimator:

$$P(\nu) \approx \frac{1}{N_{\text{pix}} \Delta\nu} \sum_{i=1}^{N_{\text{pix}}} \Theta\left(|\nu_i - \nu| \leq \frac{\Delta\nu}{2}\right), \quad (4.25)$$

where $\Theta(x)$ is the Heaviside step function. This estimator counts the number of normalized convergence ν_i that fall within each bin centered at ν , normalizing by the total number of pixels and the bin width $\Delta\nu$.

4.3.1 hmpdf Model

The `hmpdf` model (Thiele et al., 2020) presents a halo-model formalism to compute the weak lensing convergence PDF, and its covariance matrix. The one-point $P(\kappa_a)$ and two-point $P(\kappa_a, \kappa_b; \phi)$ PDFs are separated into one-halo and two-halo terms as:

$$P_{1\text{pt}/2\text{pt}} = P_{1\text{pt}/2\text{pt}}^{1h} P_{1\text{pt}/2\text{pt}}^{2h}, \quad (4.26)$$

for exact formulae, see Thiele et al. (2020). Expanding the exponentials to the first order, the p -th order of the one-halo term describes overlaps of p halos along the line of sight. The two-halo term arises from the dependence of halo density on the underlying matter density field.

4.4 Peak and Minimum Counts

Local maxima (peaks) and minima in convergence field correspond to regions of over-densities and under-densities, respectively. Analyzing the statistics of these extrema offers insights into the non-Gaussian features of the matter distribution, providing a powerful tool to constrain cosmological models beyond traditional two-point statistics like the power spectrum (Jain & Van Waerbeke, 2000;

[Dietrich & Hartlap, 2010](#)).

The i -th pixel in the normalized convergence map, ν is identified as a peak or a minimum by comparing its value with those of its neighboring pixels. Formally, let $\mathcal{N}(i)$ denote the set of neighboring pixels adjacent to pixel i . The conditions for a pixel to be classified as a peak or a minimum are then defined as:

$$\text{Peak Condition: } \kappa_{\text{smooth},i} > \kappa_{\text{smooth},j} \quad \forall j \in \mathcal{N}(i), \quad (4.27)$$

$$\text{Minimum Condition: } \kappa_{\text{smooth},i} < \kappa_{\text{smooth},j} \quad \forall j \in \mathcal{N}(i). \quad (4.28)$$

These conditions ensure that peaks are local maxima and minima are local minima in the convergence field. Figure 4.1 illustrates the identification of peaks (red circles) and minima (blue circles) in the smoothed convergence map $\kappa_{\text{smooth}}(\hat{\mathbf{n}})$.

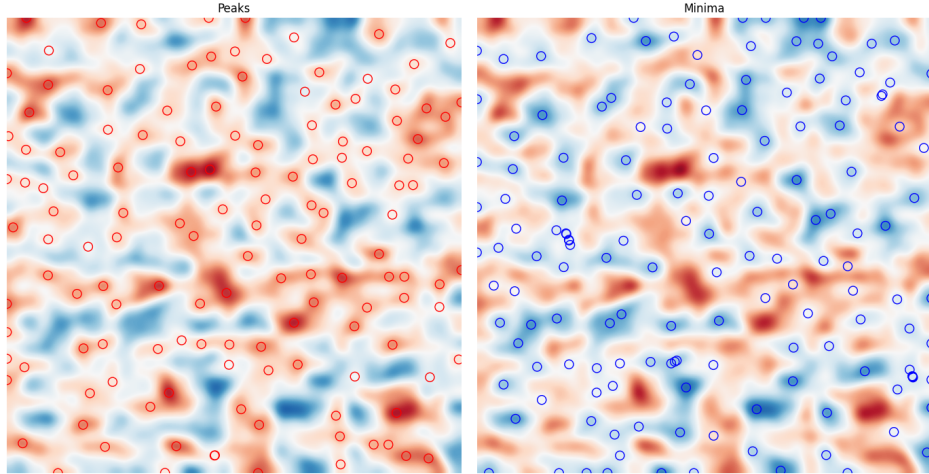


Figure 4.1: Identification of peaks and minima in a smoothed convergence map. The left panel shows the smoothed convergence field $\kappa_{\text{smooth}}(\hat{\mathbf{n}})$ with peaks (red circles) satisfying the peak condition (Equation (4.27)), and the right panel highlights the minima (blue circles) satisfying the minimum condition (Equation (4.28)).

The noise properties of peaks can be analytically described using Gaussian statistics ([Bardeen et al., 1986; Bond & Efstathiou, 1987](#)). Due to the symmetry of a Gaussian field, the expected number density of minima below $-\nu$ is equal to that of peaks above ν , $N_{\min}(-\nu) = N_{\text{peak}}(\nu)$.

Different approaches to analytically predict weak lensing peak counts have been developed over the recent years. One milestone is the model for Gaussian random Field developed by [Bardeen et al. \(1986\)](#), and the extention to the weak lensing field by [Maturi et al. \(2010\)](#). Another popular way to analyze weak lensing data is to compare the measured peak counts to weak lensing maps generated by N-body simulations ([Kacprzak et al., 2016; Martinet et al., 2018; Zürcher et al., 2021](#)).

4.5 Minkowski Functionals

Minkowski functionals are powerful morphological descriptors derived from integral geometry, widely used to quantify the geometry and topology of spatial structures ([Armijo et al., 2024](#)).

For a two-dimensional normalized convergence field $\nu(\hat{\mathbf{n}})$ with zero mean and variance σ_0^2 , the excursion set $\Sigma(\nu_0)$ at threshold ν_0 is defined as the set of points where the field exceeds a certain threshold value:

$$\Sigma(\nu_0) = \left\{ \hat{\mathbf{n}} \in S^2 \mid \nu(\hat{\mathbf{n}}) > \nu_0 \right\}. \quad (4.29)$$

Figure 4.2 shows $\Sigma(\nu_0)$ for increasing threshold values $\nu_0 = 0.5, 1, 1.5$ and 2 . As the threshold increases, the size and connectivity of the excursion sets diminish, reflecting the decreasing number of high-value regions in the field.

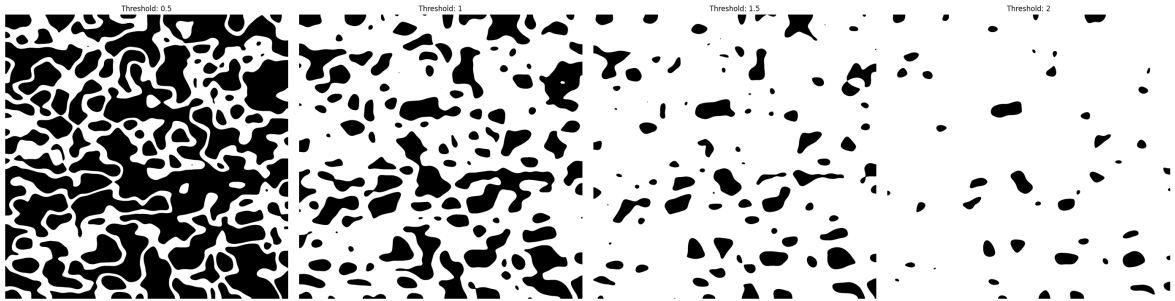


Figure 4.2: Excursion sets $\Sigma(\nu) = \{\kappa > \nu\sigma_0\}$ for increasing thresholds ($\nu = 0.5, 1, 1.5, 2$). Black regions indicate areas where κ exceeds $\nu\sigma_0$, showing reduced size and connectivity as ν increases.

The Minkowski functionals $V_0(\nu_0)$, $V_1(\nu_0)$, and $V_2(\nu_0)$ quantify the morphological properties of these excursion sets ([Matsubara, 2010](#)):

$$V_0(\nu_0) = \frac{1}{A} \int_{\Sigma(\nu_0)} da, \quad (4.30)$$

$$V_1(\nu_0) = \frac{1}{4A} \int_{\partial\Sigma(\nu_0)} dl, \quad (4.31)$$

$$V_2(\nu_0) = \frac{1}{2\pi A} \int_{\partial\Sigma(\nu_0)} \mathcal{K} dl, \quad (4.32)$$

where A is the total area, da and dl are area and length elements, and \mathcal{K} is the geodesic curvature of the boundary $\partial\Sigma(\nu)$. Specifically: $V_0(\nu)$ measures the area fraction of the excursion set, $V_1(\nu)$ measures half the boundary length per unit area, and $V_2(\nu)$ quantifies the Euler characteristic per unit area.

For a pixelized map with ν_{pix} pixels, the continuous integrals in Equations (4.30)–(4.32) are ap-

proximated by discrete sums ([Kratochvil et al., 2012](#)):

$$V_0(\nu_0) \approx \frac{1}{N_{\text{pix}}} \sum_{i=1}^{N_{\text{pix}}} \Theta(\nu_i - \nu_0), \quad (4.33)$$

$$V_1(\nu_0) \approx \frac{1}{4N_{\text{pix}}} \sum_{i=1}^{N_{\text{pix}}} \sum_{j \in \mathcal{N}(i)} |\Theta(\nu_i - \nu_0) - \Theta(\nu_j - \nu_0)|, \quad (4.34)$$

$$V_2(\nu_0) \approx \frac{1}{2\pi N_{\text{pix}}} \sum_{i=1}^{N_{\text{pix}}} \delta_D(\nu_i - \nu_0) \left(\frac{\nu_{,xx}\nu_{,yy} - \nu_{,xy}^2}{\nu_{,x}^2 + \nu_{,y}^2} \right), \quad (4.35)$$

where Θ is the Heaviside function, δ_D the Dirac delta function, $\mathcal{N}(i)$ the neighboring pixels of i , and derivatives are estimated via finite differences.

For a two-dimensional GRF $\kappa(\hat{\mathbf{n}})$ with zero mean and unit variance (after normalization), the Minkowski functionals are ([Matsubara, 2010](#)):

$$V_0(\nu) = \frac{1}{2} \operatorname{erf} \left(\frac{\nu}{\sqrt{2}} \right), \quad (4.36)$$

$$V_1(\nu) = \frac{\sigma_1}{8\sqrt{2}\sigma_0} e^{-\nu^2/2}, \quad (4.37)$$

$$V_2(\nu) = \frac{\sigma_1^2}{2\pi\sigma_0^3} \nu e^{-\nu^2/2}, \quad (4.38)$$

where erf is the error function, and $\sigma_1^2 = \langle |\nabla \nu|^2 \rangle = \langle \kappa_{,x}^2 + \kappa_{,y}^2 \rangle$. These expressions provide a Gaussian benchmark for identifying non-Gaussian features in the data.

Chapter 5

Covariance

Contents

5.1	Role of the Covariance Matrix	43
5.2	Covariance of the Matter Power Spectrum	45
5.3	Covariance of the Angular Power Spectrum	46
5.4	Covariance of Higher-Order Statistics	48

The covariance matrix encapsulates the uncertainties and correlations between different measurements. It plays a critical role in parameter estimation techniques, including maximum likelihood analyses and Bayesian inference, and is foundational in forecasting the capabilities of future surveys through the Fisher information matrix.

The covariance matrix between two observables \mathcal{O}_i and \mathcal{O}_j is defined as:

$$\text{Cov}(\mathcal{O}_i, \mathcal{O}_j) = \langle (\mathcal{O}_i - \langle \mathcal{O}_i \rangle)(\mathcal{O}_j - \langle \mathcal{O}_j \rangle) \rangle, \quad (5.1)$$

where $\langle \cdot \rangle$ denotes the ensemble average over multiple realizations. For an unbiased estimator, the covariance matrix is given by:

$$\text{Cov}(\mathcal{O}_i, \mathcal{O}_j) = \frac{1}{N_{\text{sim}} - 1} \sum_{n=1}^{N_{\text{sim}}} (\mathcal{O}_i^{(n)} - \langle \mathcal{O}_i \rangle)(\mathcal{O}_j^{(n)} - \langle \mathcal{O}_j \rangle), \quad (5.2)$$

where N_{sim} is the number of simulations, and $\mathcal{O}_i^{(n)}$ is the i -th realization of the statistic in the n -th simulation.

5.1 Role of the Covariance Matrix

Though we leave the Fisher forecast using the covariance matrix for future work, it is worthwhile to discuss the importance of the covariance matrix in the context of weak lensing statistics ([Takada &](#)

Jain, 2004; Kilbinger & Schneider, 2005). When comparing theoretical models to observational data, we often compute a likelihood function $\mathcal{L}(\mathbf{d}|\mathbf{p})$, where \mathbf{d} represents the data vector and \mathbf{p} denotes the set of cosmological parameters. According to Bayes's theorem, the posterior distribution $P(\mathbf{p}|\mathbf{d})$ of the model parameters \mathbf{p} given the data \mathbf{d} is given by:

$$P(\mathbf{p}|\mathbf{d}) = \frac{\mathcal{L}(\mathbf{d}|\mathbf{p})\pi(\mathbf{p})}{\epsilon(\mathbf{d})}, \quad (5.3)$$

where $\pi(\mathbf{p})$ is the prior distribution of the parameters, and $\epsilon(\mathbf{d})$ is the evidence, which normalizes the posterior distribution. For Gaussian-distributed data, the likelihood function is given by:

$$\ln \mathcal{L}(\mathbf{d}|\mathbf{p}) = -\frac{1}{2}(\mathbf{d} - \mathbf{m}(\mathbf{p}))^T \mathbf{C}^{-1} (\mathbf{d} - \mathbf{m}(\mathbf{p})) + \text{const}, \quad (5.4)$$

where $\mathbf{m}(\mathbf{p})$ is the model prediction for the data vector \mathbf{d} , and N is the number of data points. The covariance matrix \mathbf{C} quantifies the uncertainties and correlations between different data points.

Based on the likelihood function, we can construct the Fisher information matrix $\mathcal{F}_{\alpha\beta}$, which quantifies the sensitivity of the likelihood function to changes in the model parameters \mathbf{p} . The Fisher information matrix is defined as:

$$\mathcal{F}_{\alpha\beta} = - \left\langle \frac{\partial^2 \ln \mathcal{L}}{\partial p_\alpha \partial p_\beta} \right\rangle, \quad (5.5)$$

In the case of Gaussian likelihoods, the Fisher information matrix is simplified to:

$$\mathcal{F}_{\alpha\beta} = \frac{1}{2} \text{Tr} \left[\mathbf{C}^{-1} \frac{\partial \mathbf{C}}{\partial p_\alpha} \mathbf{C}^{-1} \frac{\partial \mathbf{C}}{\partial p_\beta} \right] \Bigg|_{p_\alpha = \mu_\alpha} + \left(\frac{\partial \mu}{\partial p_\alpha} \right)^T \mathbf{C}^{-1} \frac{\partial \mu}{\partial p_\beta}, \quad (5.6)$$

where μ is the mean of the data vector \mathbf{d} . As assumed in most studies, the covariance matrix \mathbf{C} is model independent, so that the Fisher information matrix can be reduced to:

$$\mathcal{F}_{\alpha\beta} = \left(\frac{\partial \mu}{\partial p_\alpha} \right)^T \mathbf{C}^{-1} \frac{\partial \mu}{\partial p_\beta}, \quad (5.7)$$

The Fisher matrix allows us to forecast the expected uncertainties on the parameters via the Cramér-Rao bound:

$$\langle (\Delta p_\alpha)^2 \rangle \geq (\mathcal{F}^{-1})_{\alpha\alpha}, \quad (5.8)$$

where Δp_α is the uncertainty on the α -th parameter. Note that this condition is marginalized over all other parameters, p_β ($\beta \neq \alpha$). The correlation coefficient between two parameters p_α and p_β is given by:

$$\rho_{\alpha\beta} = \frac{(\mathcal{F}^{-1})_{\alpha\beta}}{\sqrt{(\mathcal{F}^{-1})_{\alpha\alpha}(\mathcal{F}^{-1})_{\beta\beta}}}. \quad (5.9)$$

5.2 Covariance of the Matter Power Spectrum

Understanding the covariance matrix of the matter power spectrum $P_m(k)$ is crucial before delving into two-dimensional weak lensing statistics. The covariance matrix for the matter power spectrum is defined as:

$$\text{Cov}(k, k') = \langle \hat{P}_m(k) \hat{P}_m(k') \rangle - \langle \hat{P}_m(k) \rangle \langle \hat{P}_m(k') \rangle, \quad (5.10)$$

where $\hat{P}_m(k)$ is an estimator of the matter power spectrum obtained from a finite volume V . An estimator for the matter power spectrum in a finite survey volume is given by (Feldman et al., 1994):

$$\hat{P}_m(k) = (2\pi)^3 \delta_D(\mathbf{k} + \mathbf{k}') \tilde{\delta}(\mathbf{k}) \tilde{\delta}(-\mathbf{k}) = V_f \int_{V_s(k)} \frac{d^3 \mathbf{k}}{V_s(k)} \tilde{\delta}(\mathbf{k}) \tilde{\delta}(-\mathbf{k}), \quad (5.11)$$

where $V_f = (2\pi)^3/V$ is the volume of a Fourier cell where V is the total survey volume, and $V_s(k) = 4\pi k^2 \Delta k$ is the volume of the shell in Fourier space corresponding to wavenumber k .

To derive the covariance matrix, we substitute the estimator $\hat{P}_m(k)$ into the covariance definition:

$$\text{Cov}(\mathbf{k}, \mathbf{k}') = V_f^2 \left(\langle \tilde{\delta}(\mathbf{k}) \tilde{\delta}(-\mathbf{k}) \tilde{\delta}(\mathbf{k}') \tilde{\delta}(-\mathbf{k}') \rangle - \langle \tilde{\delta}(\mathbf{k}) \tilde{\delta}(-\mathbf{k}) \rangle \langle \tilde{\delta}(\mathbf{k}') \tilde{\delta}(-\mathbf{k}') \rangle \right) \quad (5.12)$$

The four-point correlation function $\langle \tilde{\delta}(\mathbf{k}_1) \tilde{\delta}(\mathbf{k}_2) \tilde{\delta}(\mathbf{k}_3) \tilde{\delta}(\mathbf{k}_4) \rangle$ can be decomposed using Wick's theorem (valid for Gaussian fields) into products of two-point functions (Wick, 1950):

$$\begin{aligned} \langle \tilde{\delta}(\mathbf{k}) \tilde{\delta}(-\mathbf{k}) \tilde{\delta}(\mathbf{k}') \tilde{\delta}(-\mathbf{k}') \rangle &= \langle \tilde{\delta}(\mathbf{k}) \tilde{\delta}(-\mathbf{k}) \rangle \langle \tilde{\delta}(\mathbf{k}') \tilde{\delta}(-\mathbf{k}') \rangle \\ &+ \langle \tilde{\delta}(\mathbf{k}) \tilde{\delta}(\mathbf{k}') \rangle \langle \tilde{\delta}(-\mathbf{k}) \tilde{\delta}(-\mathbf{k}') \rangle \\ &+ \langle \tilde{\delta}(\mathbf{k}) \tilde{\delta}(-\mathbf{k}') \rangle \langle \tilde{\delta}(-\mathbf{k}) \tilde{\delta}(\mathbf{k}') \rangle \\ &+ \langle \tilde{\delta}(\mathbf{k}) \tilde{\delta}(-\mathbf{k}) \tilde{\delta}(\mathbf{k}') \tilde{\delta}(-\mathbf{k}') \rangle_c, \end{aligned} \quad (5.13)$$

where the last term represents the connected (non-Gaussian) part of the four-point function, known as the trispectrum $T(\mathbf{k}, -\mathbf{k}, \mathbf{k}', -\mathbf{k}')$.

Using the properties of the Dirac delta function and assuming statistical isotropy, the covariance matrix simplifies to:

$$\text{Cov}(k, k') = \frac{2P_m(k)^2}{N(k)} \delta_{k,k'} + \frac{T(k, k')}{V} \quad (5.14)$$

where $N(k) = V_s(k)/V_f$ is the number of independent modes in the shell at wavenumber k . The first term represents the Gaussian (disconnected) contribution, and the second term accounts for the non-Gaussian (connected) contribution from the trispectrum.

In the presence of a finite survey volume, super-sample covariance arises due to modes larger than the survey size influencing the observed modes (Takada & Hu, 2013). This effect adds an additional

term to the covariance matrix:

$$\text{Cov}(k, k') = \frac{2P_m^2(k)}{N(k)}\delta_{kk'} + \frac{1}{V}T(k, k') + \left(\frac{\partial P_m(k)}{\partial \delta_b}\right)\left(\frac{\partial P_m(k')}{\partial \delta_b}\right)\sigma_b^2, \quad (5.15)$$

where δ_b represents the large-scale (background) density fluctuation, and σ_b^2 is its variance:

$$\sigma_b^2 = \int \frac{d^3k}{(2\pi)^3} P_m(k) |\tilde{W}(\mathbf{k})|^2, \quad (5.16)$$

with $\tilde{W}(\mathbf{k})$ being the Fourier transform of the survey window function $W(\mathbf{x})$. The derivatives $\partial P_m(k)/\partial \delta_b$ quantify the response of the power spectrum to changes in the background density and can be related to the concept of the response function or integrated perturbation theory (Li et al., 2014).

5.3 Covariance of the Angular Power Spectrum

We consider a cosmological survey characterized by a window function $\mathcal{W}(\theta)$ and a total survey area $\Omega_{\mathcal{W}}$, defined as the integral of the window function over the sky (Takada & Hu, 2013):

$$\Omega_{\mathcal{W}} = \int d^2\theta \mathcal{W}(\theta). \quad (5.17)$$

The window function $\mathcal{W}(\theta)$, and its Fourier transform, $\tilde{\mathcal{W}}(\ell)$, accounts for the survey geometry and selection effects. Therefore, we can define the observed convergence field $\kappa_{\mathcal{W}}(\theta)$ as:

$$\kappa_{\mathcal{W}}(\theta) = \mathcal{W}(\theta) \kappa(\theta). \quad (5.18)$$

where $\kappa(\theta)$ is the true convergence field. The Fourier transform of the observed convergence field is given by:

$$\tilde{\kappa}_{\mathcal{W}}(\ell) = \int \frac{d^2\ell'}{(2\pi)^2} \tilde{\mathcal{W}}(\ell') \tilde{\kappa}(\ell - \ell'). \quad (5.19)$$

In the presence of the window function, the estimator for the angular power spectrum C_ℓ is given by (Takada & Hu, 2013):

$$\hat{C}_\ell = \frac{1}{\Omega_{\mathcal{W}}} \tilde{\kappa}_{\mathcal{W}}(\ell) \tilde{\kappa}_{\mathcal{W}}(-\ell). \quad (5.20)$$

The covariance matrix of the angular power spectrum C_ℓ is defined as:

$$\text{Cov}(\ell_1, \ell_2) = \langle \hat{C}_{\ell_1} \hat{C}_{\ell_2} \rangle - \langle \hat{C}_{\ell_1} \rangle \langle \hat{C}_{\ell_2} \rangle, \quad (5.21)$$

which measures the statistical correlation between estimates of C_{ℓ_1} and C_{ℓ_2} .

Substituting the estimator \hat{C}_ℓ into the covariance definition and expanding the resulting expression leads to terms involving two-point and four-point correlation functions of the convergence field $\kappa(\theta)$.

Specifically, the covariance can be expressed as:

$$\begin{aligned}\text{Cov}(\ell_1, \ell_2) &= \frac{1}{\Omega_{\mathcal{W}}^2} [\langle \tilde{\kappa}_{\mathcal{W}}(\ell_1) \tilde{\kappa}_{\mathcal{W}}(-\ell_1) \tilde{\kappa}_{\mathcal{W}}(\ell_2) \tilde{\kappa}_{\mathcal{W}}(-\ell_2) \rangle - \langle \tilde{\kappa}_{\mathcal{W}}(\ell_1) \tilde{\kappa}_{\mathcal{W}}(-\ell_1) \rangle \langle \tilde{\kappa}_{\mathcal{W}}(\ell_2) \tilde{\kappa}_{\mathcal{W}}(-\ell_2) \rangle] \\ &= \frac{1}{\Omega_{\mathcal{W}}^2} [\langle \tilde{\kappa}(\ell_1) \tilde{\kappa}(-\ell_1) \tilde{\kappa}(\ell_2) \tilde{\kappa}(-\ell_2) \rangle + (\ell_2 \leftrightarrow -\ell_2)] \\ &+ \frac{1}{\Omega_{\mathcal{W}}^2} \langle \tilde{\kappa}(\ell_1) \tilde{\kappa}(-\ell_1) \tilde{\kappa}(\ell_2) \tilde{\kappa}(-\ell_2) \rangle_c\end{aligned}\quad (5.22)$$

By a straightforward calculation, this expression can be simplified to:

$$\begin{aligned}\text{Cov}(\ell_1, \ell_2) &= \frac{1}{\Omega_{\mathcal{W}}^2} [C_{\ell_1}]^2 \left[|\tilde{\mathcal{W}}(\ell_1 + \ell_2)|^2 + |\tilde{\mathcal{W}}(\ell_1 - \ell_2)|^2 \right] \\ &+ \frac{1}{\Omega_{\mathcal{W}}^2} \int \frac{d^2 \ell'}{(2\pi)^2} \mathcal{T}(\ell'_1, -\ell'_1 + \ell', \ell'_2, -\ell'_2 - \ell'),\end{aligned}\quad (5.23)$$

where $\mathcal{T}(\ell_1, -\ell_1, \ell_2, -\ell_2)$ is the trispectrum of the convergence field.

Using the Limber approximation (Limber, 1954), which simplifies the projection of three-dimensional quantities into two dimensions, the covariance matrix can be related to the matter power spectrum.

$$C_{\ell} = \int d\chi \frac{W^2(\chi)}{\chi^2} P_m \left(\frac{\ell}{\chi}, \chi \right), \quad (5.24)$$

$$\mathcal{T}(\ell_1, -\ell_1, \ell_2, -\ell_2) = \int d\chi \frac{W^4(\chi)}{\chi^6} T_m \left(\frac{\ell_1}{\chi}, -\frac{\ell_1}{\chi}, \frac{\ell_2}{\chi}, -\frac{\ell_2}{\chi} \right), \quad (5.25)$$

Similar to the matter power spectrum, the covariance matrix for the angular power spectrum can be decomposed into:

$$\text{Cov}(\ell_1, \ell_2) = \text{Cov}^G(\ell_1, \ell_2) + \text{Cov}^{\text{cNG}}(\ell_1, \ell_2) + \text{Cov}^{\text{SSC}}(\ell_1, \ell_2), \quad (5.26)$$

where:

$$\text{Cov}^G(\ell_1, \ell_2) = \frac{1}{\Omega_{\mathcal{W}}^2} [C_{\ell_1}]^2 \left[|\tilde{\mathcal{W}}(\ell_1 + \ell_2)|^2 + |\tilde{\mathcal{W}}(\ell_1 - \ell_2)|^2 \right], \quad (5.27)$$

$$\text{Cov}^{\text{cNG}}(\ell_1, \ell_2) = \frac{1}{\Omega_{\mathcal{W}}^2} \int \frac{d^2 \ell'}{(2\pi)^2} \mathcal{T}^{\text{cNG}}(\ell'_1, -\ell'_1 + \ell', \ell'_2, -\ell'_2 - \ell'), \quad (5.28)$$

$$\text{Cov}^{\text{SSC}}(\ell_1, \ell_2) = \frac{1}{\Omega_{\mathcal{W}}^2} \int \frac{d^2 \ell'}{(2\pi)^2} |\tilde{\mathcal{W}}(\ell')|^2 \sigma_{\ell_1, \ell_2}^{\ell'}, \quad (5.29)$$

with:

$$\sigma_{\ell_1, \ell_2}^{\ell'} = \int d\chi \frac{W^4(\chi)}{\chi^6} \left(\frac{\partial P_m \left(\frac{\ell_1}{\chi}, \chi \right)}{\partial \delta_b} \right) \left(\frac{\partial P_m \left(\frac{\ell_2}{\chi}, \chi \right)}{\partial \delta_b} \right) P_m \left(\frac{\ell_1}{\chi}, \chi \right) P_m \left(\frac{\ell_2}{\chi}, \chi \right) P_L \left(\frac{\ell'}{\chi} \right), \quad (5.30)$$

where $P_L(k)$ is the linear matter power spectrum. Notably, the SSC term $\text{Cov}^{\text{SSC}}(\ell_1, \ell_2)$ arises from

the large-scale density fluctuations modulating the observed power spectrum within the survey area ([Takada & Hu, 2013](#)).

5.4 Covariance of Higher-Order Statistics

Despite some successes in analytical modeling ([Chan et al. 2018](#); [Lacasa et al. 2018](#); [Lacasa & Grain 2019](#); [Uhlemann et al. 2023](#)), computing the covariance matrices for higher-order statistics still need to rely on simulations. Drawing an analogy with the matter power spectrum, the covariance matrix for higher-order statistics can be expressed as:

$$\text{Cov}(\mathcal{O}_i, \mathcal{O}_j) = \text{Cov}^{\text{noSSC}}(\mathcal{O}_i, \mathcal{O}_j) + \text{Cov}^{\text{SSC}}(\mathcal{O}_i, \mathcal{O}_j), \quad (5.31)$$

A rigorous super-sample covariance for line-of-sight integrated observable \mathcal{O}_i , where $\mathcal{O}_i = \int dV_i \mathfrak{o}_i = \int \chi_i^2 d\chi \mathfrak{o}_i$, is given by ([Lacasa & Rosenfeld, 2016](#)):

$$\text{Cov}^{\text{SSC}}(\mathcal{O}_i, \mathcal{O}_j) = \iint dV_i dV_j \left(\frac{\partial \mathfrak{o}_i}{\partial \delta_b} \right) \left(\frac{\partial \mathfrak{o}_j}{\partial \delta_b} \right) \sigma_b^2, \quad (5.32)$$

Chapter 6

Simulations

Contents

6.1	Initial Condition Generation	50
6.2	Simulation Basics	52
6.3	Tools for Fast Computation	54
6.4	FASTPM	57
6.5	Weak Lensing Map Generation	59

Numerical simulations are crucial in physics and astronomy for studying complex systems of interacting particles, such as galaxies and the Universe’s large-scale structure, where analytical solutions are often impractical due to complexity and nonlinearity. This section provides an overview of N -body simulations commonly used in cosmology.

Since the 1980s, numerical cosmology has developed algorithms to mitigate the computational challenges posed by long-range gravitational interactions by reducing global communication across the computational domain. Key algorithms include mesh-based methods, tree codes, and multipole expansions (Hockney & Eastwood, 1981). Figure 6.1 displays the number of particles used in selected N -body simulations employing these techniques. Symbols and colors indicate the gravitational solvers: particle-particle-particle-mesh (P^3M) and adaptive P^3M (AP^3M); parallel or vectorized P^3M ; Tree codes; TreePM; and particle-mesh methods with adaptive mesh refinement (PM AMR).

Advancements in algorithms and software optimization have increased the number of particles in cosmological simulations beyond what direct summation methods allow. Since 1990, gravity-only simulations have exhibited a super-exponential growth trend, indicated by the quadratic regression in Figure 6.1, reflecting significant methodological innovations beyond hardware improvements (Leclercq, 2020).

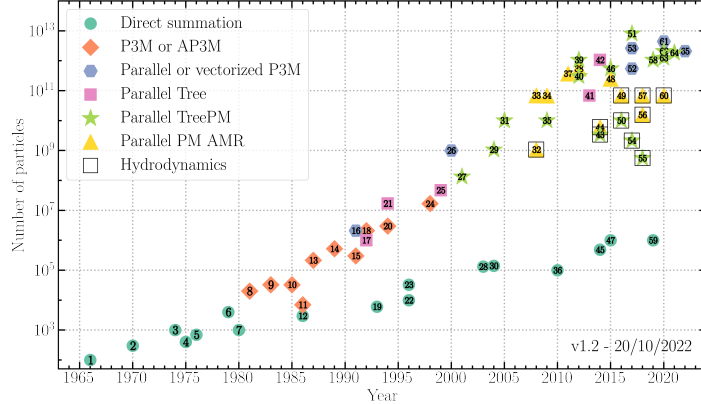


Figure 6.1: Evolution of the number of particles used in N -body simulations as a function of the year of publication (Leclercq, 2020). The symbols and colors indicate the gravitational solver employed: P^3M and adaptive P^3M (AP^3M); parallel or vectorized P^3M ; Tree codes; TreePM; and particle-mesh methods with adaptive mesh refinement (PM AMR). Hydrodynamic simulations are represented by black squares.

6.1 Initial Condition Generation

As we have seen in Section 2.4, the primordial power spectrum $P(k)$ is a key ingredient in generating initial conditions for cosmological simulations. Based on the linear power spectrum, we will review the process of generating initial conditions for N -body simulations.

6.1.1 Initial Density Field

To generate the initial density field for the simulations, we express the density contrast $\delta(\mathbf{x})$ in terms of its Fourier components:

$$\delta(\mathbf{x}) = \int \frac{d^3 k}{(2\pi)^3} \tilde{\delta}(\mathbf{k}) e^{i\mathbf{k}\cdot\mathbf{x}}. \quad (6.1)$$

Assuming a Gaussian random field, each Fourier mode $\tilde{\delta}(\mathbf{k})$ is a complex Gaussian random variable with zero mean and variance $P(k)$:

$$\tilde{\delta}(\mathbf{k}) = A(\mathbf{k}) + iB(\mathbf{k}), \quad (6.2)$$

$$\langle A(\mathbf{k}) \rangle = \langle B(\mathbf{k}) \rangle = 0, \quad (6.3)$$

$$\langle A(\mathbf{k})A(\mathbf{k}') \rangle = \langle B(\mathbf{k})B(\mathbf{k}') \rangle = \frac{1}{2}P(k)\delta_D(\mathbf{k}-\mathbf{k}'), \quad (6.4)$$

$$\langle A(\mathbf{k})B(\mathbf{k}') \rangle = 0, \quad (6.5)$$

where $A(\mathbf{k})$ and $B(\mathbf{k})$ are real Gaussian random variables, and δ_D is the Dirac delta function.

6.1.2 Initial Displacement Field

The initial displacement field $\Psi(\mathbf{q})$ relates the Lagrangian coordinates \mathbf{q} to the Eulerian coordinates \mathbf{x} :

$$\mathbf{x}(\mathbf{q}) = \mathbf{q} + \Psi(\mathbf{q}). \quad (6.6)$$

The displacement field is proportional to the gradient of the gravitational potential $\Phi(\mathbf{q})$:

$$\Psi(\mathbf{q}) = -\nabla\Phi(\mathbf{q}), \quad (6.7)$$

where the potential satisfies Poisson's equation:

$$\nabla^2\Phi(\mathbf{q}) = \delta(\mathbf{q}). \quad (6.8)$$

The first order solution to the displacement field is given by the Zel'dovich approximation ([Zel'dovich, 1970](#)):

$$-k^2\tilde{\Phi}(\mathbf{k}) = \tilde{\delta}(\mathbf{k}), \quad (6.9)$$

$$\tilde{\Psi}(\mathbf{k}) = i\mathbf{k}\tilde{\Phi}(\mathbf{k}) = i\mathbf{k}\frac{\tilde{\delta}(\mathbf{k})}{k^2}, \quad (6.10)$$

$$\Psi(\mathbf{q}) = \int \frac{d^3k}{(2\pi)^3} i\mathbf{k} \frac{\tilde{\delta}(\mathbf{k})}{k^2} e^{i\mathbf{k}\cdot\mathbf{q}}. \quad (6.11)$$

6.1.3 Initial Velocities

The initial velocities of particles are derived from the time derivative of the displacement field. The velocities are given by ([Efstathiou et al., 1985](#)):

$$\mathbf{v}(\mathbf{q}) = aHf(a)\Psi(\mathbf{q}), \quad (6.12)$$

$$\tilde{\mathbf{v}}(\mathbf{k}) = aHf(a)\tilde{\Psi}(\mathbf{k}) = aHf(a)i\mathbf{k}\frac{\tilde{\delta}(\mathbf{k})}{k^2}, \quad (6.13)$$

$$\mathbf{v}(\mathbf{q}) = iaHf(a) \int \frac{d^3k}{(2\pi)^3} \frac{\mathbf{k}}{k^2} \tilde{\delta}(\mathbf{k}) e^{i\mathbf{k}\cdot\mathbf{q}}, \quad (6.14)$$

where a is the scale factor, H is the Hubble parameter, and $f(a)$ is the growth rate defined as:

$$f(a) = \frac{d \ln D}{d \ln a}, \quad (6.15)$$

6.2 Simulation Basics

We outline the fundamental concepts and algorithms used in N -body simulations, including direct summation, particle-mesh methods, particle-particle particle-mesh (P3M) methods, and tree-particle-mesh (Tree-PM) methods.

6.2.1 Direct Summation

Direct Summation calculates gravitational forces between all particle pairs directly, scaling as $\mathcal{O}(N^2)$ and becoming computationally intensive for large N . Each particle i has position \mathbf{r}_i , velocity \mathbf{v}_i , and mass m_i . At each time step t :

1. Compute Forces:

$$\mathbf{F}_i = Gm_i \sum_{\substack{j=1 \\ j \neq i}}^N \frac{m_j(\mathbf{r}_j - \mathbf{r}_i)}{\|\mathbf{r}_j - \mathbf{r}_i\|^3}$$

2. Update Particle States:

$$\mathbf{v}_i(t + \Delta t) = \mathbf{v}_i(t) + \frac{\mathbf{F}_i}{m_i} \Delta t, \quad \mathbf{r}_i(t + \Delta t) = \mathbf{r}_i(t) + \mathbf{v}_i(t + \Delta t) \Delta t$$

3. Advance Time:

$$t \leftarrow t + \Delta t$$

6.2.2 Particle-Mesh (PM) Method

The PM method approximates gravitational forces by mapping particles onto a grid and solving for the gravitational potential, reducing computational cost to $\mathcal{O}(N + M \log M)$, where M is the number of grid points. While efficient for large-scale simulations, it smooths out small-scale forces.

The main difference between the PM method and direct summation is the grid-based force calculation:

1. Assign Particles to Grid: See Section 6.3.2.

2. Compute Density Field:

$$\rho(\mathbf{x}) = \sum_i m_i W(\mathbf{x} - \mathbf{r}_i) \quad (\text{where } W: \text{Interpolation Kernel})$$

3. Solve Poisson's Equation:

$$\nabla^2 \Phi = 4\pi G \rho$$

4. Compute Force due to Potential:

$$\mathbf{E} = -\nabla\Phi$$

6.2.3 Particle-Particle Particle-Mesh (P³M) Method

The P³M method combines direct summation for short-range forces with the PM approach for long-range interactions, achieving $\mathcal{O}(N \log N)$ complexity while enhancing accuracy for nearby particles. Key parameters include mesh size, softening parameter ϵ , and force resolution.

The difference between the P³M method and the PM method lies in the force calculation:

1. Long-Range Forces (PM):

$$\mathbf{F}_{\text{long},i} = m_i \mathbf{E}_{\text{long}}(\mathbf{r}_i)$$

2. Short-Range Forces (Direct Summation):

(a) **Neighbor Search:** Identify particles j within cutoff radius r_{cut} of particle i .

(b) **Force Calculation:**

$$\mathbf{F}_{\text{short},i} = -Gm_i \sum_{j \in \text{neighbors}} \frac{m_j(\mathbf{r}_i - \mathbf{r}_j)}{(\|\mathbf{r}_i - \mathbf{r}_j\|^2 + \epsilon^2)^{3/2}}$$

3. Combine Forces:

$$\mathbf{F}_i = \mathbf{F}_{\text{long},i} + \mathbf{F}_{\text{short},i}$$

6.2.4 Tree-Particle-Mesh (Tree-PM) Method

The Tree-PM method integrates the PM approach for long-range forces with a tree algorithm for short-range interactions, reducing complexity to $\mathcal{O}(N \log N)$. Proper tuning of parameters like grid size, softening length ϵ , and opening angle θ_{\max} is essential.

The main updates in the Tree-PM method compared to the P³M method are in the tree construction when calculating short-range forces:

1. Tree Construction:

(a) **Build Spatial Cells:** Partition the simulation volume into spatial cells (e.g., octree) and assign particles to nodes.

(b) **Multipole Moments:** For each node j , calculate mass M_j and center of mass $\mathbf{r}_{\text{cm},j}$.

2. Force Calculation: For each particle i , traverse the tree to compute the short-range gravitational force:

$$\mathbf{F}_{\text{short},i} = -Gm_i \sum_{\text{nodes}} \frac{M_j(\mathbf{r}_i - \mathbf{r}_j)}{(\|\mathbf{r}_i - \mathbf{r}_j\|^2 + \epsilon^2)^{3/2}}$$

using the opening angle criterion:

$$\theta = \frac{l_j}{\|\mathbf{r}_i - \mathbf{r}_j\|} < \theta_{\max}$$

where l_j is the size of node j and θ_{\max} is the maximum allowed opening angle.

6.3 Tools for Fast Computation

Efficient computational tools are crucial for large-scale simulations and data analysis in scientific and engineering applications. This section overviews key computational techniques and algorithms used in N -body simulations and large-scale structure studies.

6.3.1 Fast Fourier Transform

The Fast Fourier Transform (FFT) is a highly efficient algorithm for computing the Discrete Fourier Transform (DFT) of a sequence. Given a sequence of N complex numbers $\{x_n\}_{n=0}^{N-1}$, the DFT is defined as:

$$X_k = \sum_{n=0}^{N-1} x_n e^{-2\pi i k n / N}, \quad k = 0, 1, \dots, N-1. \quad (6.16)$$

The naive computation of the DFT requires $\mathcal{O}(N^2)$ operations. The FFT reduces this complexity to $\mathcal{O}(N \log N)$ by exploiting the symmetry and periodicity properties of the exponential kernel. The most common FFT algorithm is the Cooley-Tukey radix-2 FFT ([Cooley & Tukey, 1965](#)), which recursively decomposes the DFT into smaller DFTs of even and odd-indexed elements:

$$X_k = \sum_{n=0}^{N/2-1} x_{2n} e^{-2\pi i k (2n) / N} + \sum_{n=0}^{N/2-1} x_{2n+1} e^{-2\pi i k (2n+1) / N} \quad (6.17)$$

$$= X_k^{\text{even}} + e^{-2\pi i k / N} X_k^{\text{odd}}, \quad (6.18)$$

where X_k^{even} and X_k^{odd} are the DFTs of the even and odd subsequences, respectively.

6.3.2 Mass Assignment Schemes

Mass assignment schemes map particle masses onto a computational grid to compute density fields and gravitational forces, ensuring mass conservation and minimizing aliasing errors. Common schemes include:

- **Nearest Grid Point (NGP):** Each particle is assigned entirely to the nearest grid point.
- **Cloud-In-Cell (CIC):** Mass is linearly interpolated to the nearest $2^3 = 8$ surrounding grid points.

- **Triangular-Shaped Cloud (TSC):** Mass is distributed to the nearest $3^3 = 27$ grid points using a quadratic interpolation function.

In Fourier space, these mass assignment window functions are represented as:

$$W(\mathbf{k}) = \prod_{i=1}^3 W(k_i), \quad (6.19)$$

where

$$W(k_i) = \left[\frac{\sin(\pi k_i / (2k_N))}{\pi k_i / (2k_N)} \right]^p, \quad (6.20)$$

with k_N being the Nyquist wavenumber, k_i the i -th component of the wavevector \mathbf{k} , and $p = 1$ for NGP, $p = 2$ for CIC, and $p = 3$ for TSC ([Hockney & Eastwood, 1981](#); [Efstathiou et al., 1985](#)).

Figure 6.2 illustrates the mass assignment process for a particle distribution on a 1D grid using different schemes.

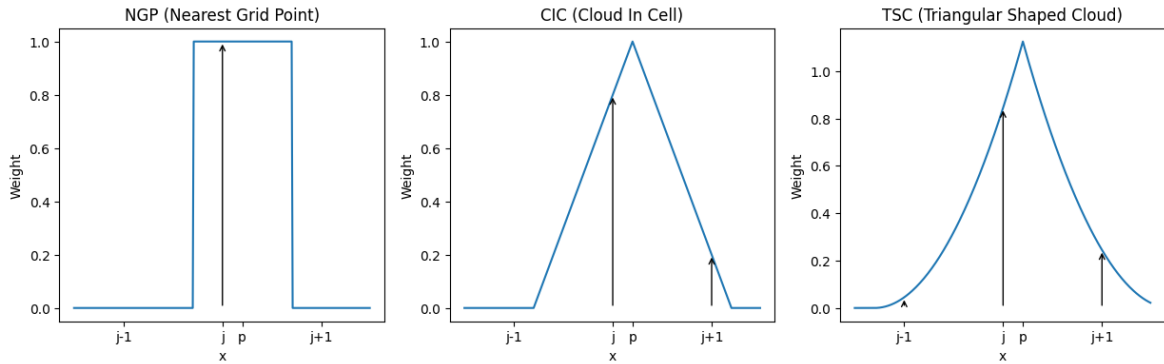


Figure 6.2: Illustration of three mass assignment schemes—Nearest Grid Point (NGP), Cloud-In-Cell (CIC), and Triangular-Shaped Cloud (TSC)—used to map a particle’s mass onto a 1D grid.

6.3.3 Parallelization Techniques

Parallelization accelerates computations in large-scale simulations by leveraging multiple processors or computing nodes. Key strategies include:

- **Domain Decomposition:** The computational domain is partitioned into smaller subdomains, each assigned to a separate processor ([Barnes & Hut, 1986](#)).
- **Task Parallelism:** Distributing independent tasks across multiple processors.
- **Data Parallelism:** Performing identical operations concurrently on different data elements, enabling SIMD (Single Instruction, Multiple Data) execution.

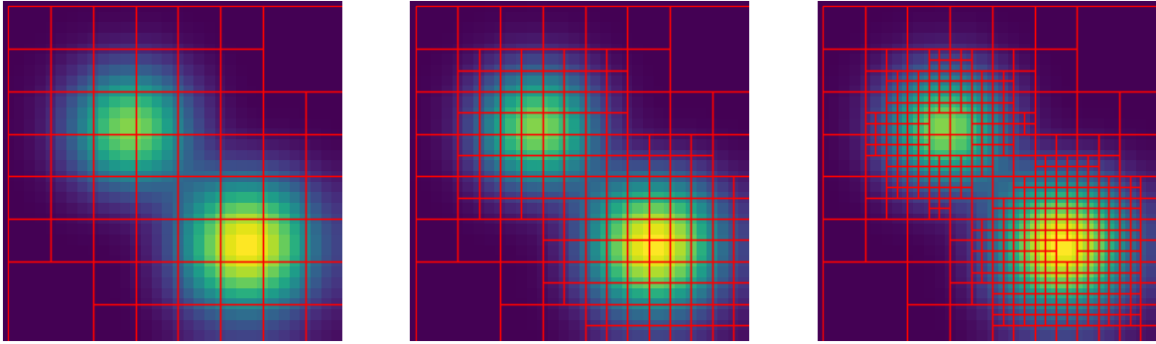


Figure 6.3: Illustration of adaptive mesh refinement (AMR) applied to a 2D image with two Gaussian kernels. The left panel shows the initial coarse grid structure over the image. The middle and right panels demonstrate progressively finer levels of mesh refinement in regions of higher intensity, where the Gaussian kernels are located. The red grid outlines indicate the adaptively refined mesh hierarchy, ensuring higher resolution where needed while maintaining computational efficiency in lower-intensity regions.

6.3.4 Adaptive Mesh Refinement

Adaptive Mesh Refinement (AMR) dynamically adjusts grid resolution, refining the mesh where higher accuracy is needed (e.g., regions with high density gradients) and coarsening it elsewhere (Berger & Colella, 1989). This creates a hierarchy of grids with increasing resolution and optimizes computational resources. Refinement is typically triggered when:

$$|\nabla \phi(\mathbf{x})| > \theta, \quad (6.21)$$

with θ being a predefined threshold.

Figure 6.3 demonstrates the application of Adaptive Mesh Refinement (AMR) to a two-dimensional image containing two Gaussian kernels. Initially, a uniformly coarse grid overlays the entire image (left panel). As the refinement process progresses, the mesh becomes increasingly finer in regions with higher intensity, specifically around the Gaussian kernels (middle and right panels). The red grid lines represent the hierarchy of the refined meshes, enabling higher resolution where it is most needed and optimizing computational resources by keeping a coarser grid in less significant areas.

6.3.5 Tree Construction

Tree-based data structures efficiently organize hierarchical spatial data. The Barnes-Hut algorithm employs an octree to partition space, reducing computational complexity from $\mathcal{O}(N^2)$ to $\mathcal{O}(N \log N)$ by approximating distant particle clusters as single mass points. This approximation is controlled by the opening angle θ :

$$\frac{s}{d} < \theta, \quad (6.22)$$

where s is the node size and d is the distance from the particle to the node's center of mass.

One of the popular algorithms for tree construction is the Barnes-Hut Octree (Barnes & Hut, 1986), which recursively subdivides the simulation volume into hierarchical grid cells. Figure 6.4 illustrates the Octree decomposition for a 3D volume containing four particles.

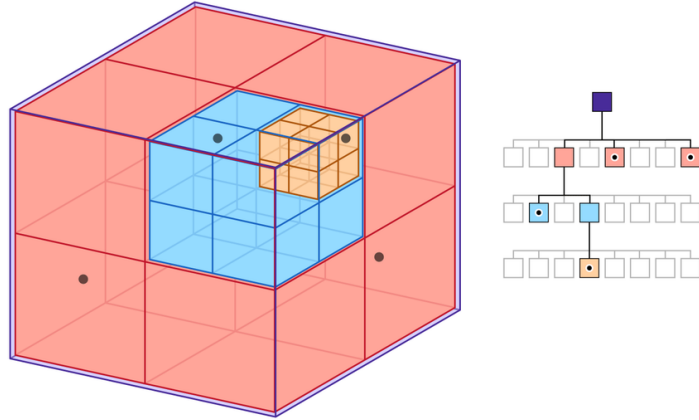


Figure 6.4: Illustration of an Octree decomposition for a 3D volume containing four particles. The left panel showcases the spatial subdivision of the volume into hierarchical grid cells, with color-coding indicating different levels of refinement. The right panel presents the corresponding Octree data structure, highlighting the hierarchical relationships between nodes. Credit by Powell et al. (2023)

Parallel tree construction involves building local trees within each subdomain and integrating them for global computations (Dubinski, 1996). Efficient parallelization enhances scalability and performance in large-scale simulations.

6.4 FASTPM

FASTPM (Fast Particle Mesh; Feng et al. 2016) is an advanced N-body simulation code tailored for efficiently modeling the evolution of dark matter and halo structures on cosmological scales. Building upon the foundational PM approach, FASTPM integrates modified kick and drift factors derived from the Zel'dovich Approximation (ZA). This enhancement allows FASTPM to achieve high accuracy in large-scale structure formation while significantly reducing computational overhead. This subsection delineates the core methodology of FASTPM, incorporating the mathematical formalism of its modified kick and drift factors.

6.4.1 Modified Kick and Drift Factors

The cornerstone of FASTPM's enhanced performance lies in its **modified kick** (K_{FASTPM}) and **drift** (D_{FASTPM}) factors. These factors are meticulously derived from the Zel'dovich Approximation (ZA), a first-order Lagrangian perturbation theory (1LPT), to rectify inaccuracies in large-scale growth inherent in standard PM solvers, especially when operating with a limited number of time steps.

First, the Zel'dovich equation of motion to the first order is defined as:

$$\begin{aligned}\mathbf{x}_{\text{ZA}}(a) &= \mathbf{q} + D(a)\mathbf{s}_1, \\ \mathbf{p}_{\text{ZA}}(a) &= a^3 E(a) g_p(a) \mathbf{s}_1, \\ \mathbf{f}_{\text{ZA}}(a) &= a^2 E(a) g_f(a) \mathbf{s}_1,\end{aligned}\quad (6.23)$$

where $E(a) = \frac{H(a)}{H(a=1)}$ is the dimensionless Hubble parameter, and $g_p(a)$ and $g_f(a)$ are auxiliary factors defined as:

$$g_p(a) = \frac{dD}{da}, G_p(a) = D(a) \quad (6.24)$$

$$g_f(a) = \frac{d(a^3 E g_p)}{da}, G_f(a) = a^3 E g_p(a) \quad (6.25)$$

The ZA equations of motion are reformulated in terms of drift and kick operators by integrating over a time step from a_0 to a_1 and eliminating the ZA displacement \mathbf{s}_1 :

$$\begin{aligned}\Delta \mathbf{x}_{\text{ZA}} &= \mathbf{x}_{\text{ZA}}(a_1) - \mathbf{x}_{\text{ZA}}(a_0) \\ &= [D(a)]_{a_0}^{a_1} \mathbf{s}_1 \\ &= \frac{\mathbf{p}_{\text{ZA}}(a_r)}{a_r^3 E(a_r)} \left(\frac{\Delta G_p}{g_p(a_r)} \right),\end{aligned}\quad (6.26)$$

$$\begin{aligned}\Delta \mathbf{p}_{\text{ZA}} &= \mathbf{p}_{\text{ZA}}(a_1) - \mathbf{p}_{\text{ZA}}(a_0) \\ &= \frac{\mathbf{f}_{\text{ZA}}(a_r)}{a_r^2 E(a_r)} \left(\frac{\Delta G_f}{g_f(a_r)} \right),\end{aligned}\quad (6.27)$$

where $\Delta \mathbf{x}_{\text{ZA}}$ is the change in displacement over the time step, $\Delta \mathbf{p}_{\text{ZA}}$ is the change in momentum over the time step, a_r is a reference scale factor within the time step, $\Delta G_p = G_p(a_1) - G_p(a_0)$, and $\Delta G_f = G_f(a_1) - G_f(a_0)$. Therefore, the modified kick and drift factors in FASTPM are defined as:

$$\mathcal{D}_{\text{FASTPM}} = \frac{\Delta \mathbf{x}_{\text{ZA}}}{\mathbf{p}_{\text{ZA}}} = \frac{1}{a_r^3 E(a_r)} \left(\frac{\Delta G_p}{g_p(a_r)} \right) \quad (6.28)$$

$$\mathcal{K}_{\text{FASTPM}} = \frac{\Delta \mathbf{p}_{\text{ZA}}}{\mathbf{f}_{\text{ZA}}} = \frac{1}{a_r^2 E(a_r)} \left(\frac{\Delta G_f}{g_f(a_r)} \right) \quad (6.29)$$

These operators ensure the exact integration of the ZA equations of motion, thereby accurately capturing the linear growth of structures within each time step.

6.4.2 Algorithm Steps

The main steps of the FASTPM algorithm follow the standard PM method discussed in Section 6.2.2, with the addition of the modified kick and drift operators to ensure accurate linear growth.

1. **Apply Modified Operators:** Utilize the modified kick (K_{FASTPM}) and drift (D_{FASTPM}) factors to update particle velocities and positions. These factors, derived from the ZA, ensure accurate linear growth:

- (a) **Kick Step:** Update particle velocities by applying the gravitational acceleration scaled by the modified kick factor:

$$\mathbf{v}_i \left(t + \frac{\Delta t}{2} \right) = \mathbf{v}_i(t) + \mathbf{g}_i(t) \cdot K_{\text{FASTPM}} \cdot \Delta t$$

- (b) **Drift Step:** Update particle positions using the updated velocities and the modified drift factor:

$$\mathbf{r}_i(t + \Delta t) = \mathbf{r}_i(t) + \mathbf{v}_i \left(t + \frac{\Delta t}{2} \right) \cdot D_{\text{FASTPM}} \cdot \Delta t$$

- (c) **Second Kick Step:** Apply another kick to update velocities to the full time step:

$$\mathbf{v}_i(t + \Delta t) = \mathbf{v}_i \left(t + \frac{\Delta t}{2} \right) + \mathbf{g}_i(t + \Delta t) \cdot K_{\text{FASTPM}} \cdot \Delta t$$

2. **Update Particle States:** Finalize the update of particle velocities and positions after applying the modified kick and drift operators:

$$\mathbf{v}_i(t + \Delta t) = \mathbf{v}_i \left(t + \frac{\Delta t}{2} \right) + \mathbf{g}_i(t + \Delta t) \cdot K_{\text{FASTPM}} \cdot \Delta t$$

$$\mathbf{r}_i(t + \Delta t) = \mathbf{r}_i(t) + \mathbf{v}_i \left(t + \frac{\Delta t}{2} \right) \cdot D_{\text{FASTPM}} \cdot \Delta t$$

3. **Advance Time:** Increment the simulation time by the time step Δt :

$$t \leftarrow t + \Delta t$$

6.5 Weak Lensing Map Generation

To extract statistics from N-body simulations, it is necessary to generate detailed WL maps by simulating the propagation of a vast number of virtual light rays from source galaxies to the observer. This process involves calculating the distortions and magnifications of the source images caused by the cumulative gravitational deflections from the intervening matter distribution along each line of sight.

6.5.1 Conventional Ray-Tracing Algorithm

Conventional ray-tracing algorithms are fundamental tools for generating WL maps from N-body simulations. These algorithms simplify the complex three-dimensional matter distribution by projecting it onto a series of two-dimensional lens planes. The numerical implementation of the ray-tracing algorithm involves several key computational steps, outlined below ([Das & Bode, 2008](#); [Teyssier et al., 2009](#); [Shirasaki et al., 2015](#)):

- 1. Lens Plane Generation:** The first step involves constructing the surface mass density $\Delta_{\Sigma}^j(\theta)$ for each lens plane j . This is achieved by projecting the three-dimensional matter density $\rho(\chi, \chi\theta)$ within a spherical shell bounded by comoving distances χ_j and χ_{j+1} onto a two-dimensional plane:

$$\Delta_{\Sigma}^j(\theta) = \int_{\chi_j}^{\chi_{j+1}} [\rho(\chi, \chi\theta) - \bar{\rho}(\chi)] \chi^2 d\chi, \quad (6.30)$$

where $\bar{\rho}(\chi)$ is the mean matter density at distance χ . The effective comoving distance to the center of the j -th shell, χ^j , is calculated as ([Shirasaki et al., 2015](#)):

$$\chi^j = \frac{\int_{\chi_{\min}}^{\chi_{\max}} \chi^3 d\chi}{\int_{\chi_{\min}}^{\chi_{\max}} \chi^2 d\chi} = \frac{3 \frac{\chi_{\max}^4 - \chi_{\min}^4}{\chi_{\max}^3 - \chi_{\min}^3}}, \quad (6.31)$$

where χ_{\min} and χ_{\max} are the minimum and maximum comoving distances of the shell, respectively. The convergence field $\kappa_j(\theta)$ for the j -th lens plane is then computed as:

$$\kappa_j(\theta) = \frac{4\pi G}{c^2} \frac{\Delta_{\Sigma}^j(\theta)}{a_j \chi_j}, \quad (6.32)$$

with a_j being the scale factor and χ_j the comoving distance to the j -th lens plane.

To express $\kappa_j(\theta)$ in terms of the simulation parameters, we consider the following quantities:

- V_{sim} : The simulation volume.
- N_{part} : The total number of particles in the simulation.
- N_{pix} : The number of pixels on each lens plane.
- n_{part}^j : The number of particles in the j -th shell.
- \bar{n}_{part}^j : The mean number of particles per pixel in the j -th shell.

The convergence field is then given by:

$$\kappa_j(\theta) = \frac{3H_0^2 \Omega_m}{2c^2 a_j \chi_j} \frac{V_{\text{sim}}}{N_{\text{part}}} \frac{N_{\text{pix}}}{4\pi} \left(n_{\text{part}}^j - \bar{n}_{\text{part}}^j \right), \quad (6.33)$$

2. **Potential Calculation:** To facilitate the computation of lensing effects, the lensing potential $\psi^j(\theta)$ for each lens plane is derived from the convergence field $\kappa_j(\theta)$. This is efficiently done using spherical harmonics:

$$\psi_{lm}^j = \frac{2}{l(l+1)} \kappa_{lm}^j \quad \text{for } l \neq 0, \quad (6.34)$$

and $\psi_{lm}^j = 0$ for $l = 0$. Subsequently, the lensing potential in real space is reconstructed, allowing the calculation of the deflection field $\alpha^j(\theta)$ and the optical tidal matrix $U_{ik}^j(\theta)$ through:

$$\alpha_i^j = -\nabla_i \psi^j, \quad U_{ik}^j = \nabla_i \nabla_k \psi^j. \quad (6.35)$$

3. **Deflection Angle Determination:** The deflection field $\alpha^j(\theta)$ and the optical tidal matrix $U_{ik}^j(\theta)$ are interpolated to arbitrary positions on each lens plane. The lensing matrix \mathcal{A}_{ik}^j at each plane is then updated using the recurrence relation:

$$\begin{aligned} \mathcal{A}_{ik}^{j+1} &= \left(1 - \frac{\chi_j}{\chi_{j+1}} \frac{\chi_{j+1} - \chi_{j-1}}{\chi_j - \chi_{j-1}} \right) \mathcal{A}_{ik}^{j-1} + \frac{\chi_j}{\chi_{j+1}} \frac{\chi_{j+1} - \chi_{j-1}}{\chi_j - \chi_{j-1}} \mathcal{A}_{ik}^j \\ &\quad - \frac{\chi_{j+1} - \chi_j}{\chi_{j-1}} U_{im}^j \mathcal{A}_{mk}^j, \end{aligned} \quad (6.36)$$

with the initial conditions:

$$\mathcal{A}_{ik}^1 = \delta_{ik}, \quad \mathcal{A}_{ik}^0 = \delta_{ik}, \quad (6.37)$$

for $j \geq 1$. The closest lens plane to the observer is designated as $j = 0$.

4. **Ray Propagation:** Light rays are propagated from the source galaxies to the observer through the sequence of lens planes. At each plane, the accumulated deflection angles are updated based on the lensing matrix \mathcal{A}_{ik}^j .
5. **Map Assembly:** After propagating all light rays through the lens planes, the convergence $\kappa(\theta)$ and shear $\gamma(\theta)$ fields are compiled into full-sky maps. These maps are typically represented on the HEALPix grid.

6.5.2 Born-approximated Ray-tracing

The Born approximation offers a simplified approach to weak lensing map generation by assuming that light rays travel along their unperturbed, straight-line paths from the source galaxies to the observer. This approximation neglects the bending of light rays due to gravitational deflections between lens planes, thereby reducing the computational complexity of the ray-tracing process. While this simplification can lead to faster computations, it introduces certain limitations in accurately capturing multiple deflections and non-linear lensing effects.

The Born-approximated ray-tracing algorithm comprises the following key steps:

1. **Lens Plane Calculation:** For each lens plane j , the convergence contribution $\kappa_j(\theta)$ is computed independently, incorporating the lensing efficiency function $W(\chi_j, \chi_s)$, where χ_j is the comoving distance to the j -th lens plane and χ_s is the comoving distance to the source galaxy. The convergence on the j -th plane is given by

$$\kappa_j(\theta) = W(\chi_j, \chi_s) \delta_j(\theta) \Delta \chi_j, \quad (6.38)$$

where $\delta_j(\theta) = n_{\text{part}}^j(\theta)/\bar{n}_{\text{part}}^j - 1$ represents the projected matter density contrast on the j -th lens plane, and $\Delta \chi_j$ is the comoving thickness of the j -th lens plane. The lensing efficiency function, previously defined in Eq. (3.20), is discretized for each lens plane as:

$$W(\chi_j, \chi_s) = \frac{3H_0^2 \Omega_m}{2c^2} \frac{(\chi_s - \chi_j)}{\chi_s} \frac{\chi_j}{a_j}, \quad (6.39)$$

2. **Convergence Field Assembly:** The total convergence field $\kappa(\theta)$ is obtained by summing the contributions from all individual lens planes:

$$\kappa(\theta) = \sum_j \kappa_j(\theta). \quad (6.40)$$

This linear superposition is a direct consequence of the Born approximation, which assumes that each lens plane contributes independently to the total convergence without accounting for the altered path of the light ray due to previous deflections.

Chapter 7

Methods

Contents

7.1	N-body Simulations	63
7.2	Generating Convergence Maps	66
7.3	Incorporating Noise	66
7.4	Patch Extraction for Analysis	67
7.5	Gaussian Smoothing	69
7.6	Measurements	70

In this work, we are quantifying the effect of super-sample effect on the covariance matrix of higher-order statistics for a weak lensing survey. To achieve this, we are conducting a series of N-body simulations and analyzing the resulting convergence maps. These maps allow us to compute the statistics and covariance matrices for various statistical measures. Therefore, we can investigate the impact of super-sample covariance on the covariance matrices of these statistics.

In the following sections, we will discuss the methodology used to generate the convergence maps, extract patches for analysis, incorporate noise, apply Gaussian smoothing, and compute the statistical measures. We will also outline the process for estimating the covariance matrices and comparing the results between the **BIGBOX** and **TILED** simulations.

7.1 N-body Simulations

We employed the publicly available particle-mesh simulation code, FASTPM ([Feng et al., 2016](#)) to generate the simulations used in this study. As discussed in Section [6.4](#), FASTPM is chose to achieve high accuracy while minimizing computational time.

The two simulations we have used are **BIGBOX** and **TILED**. For both simulations, we have used the same cosmological parameters as the IllustrisTNG project ([Nelson et al., 2019](#)). The parameters are listed in Table [7.1](#).

Parameter	Symbol	Value
Hubble constant	H_0	67.74 [km s ⁻¹ Mpc ⁻¹]
Matter density	Ω_m	0.3089
Baryon density	Ω_b	0.0486
Amplitude of fluctuations	σ_8	0.8159
Spectral index	n_s	0.9667
Sum of neutrino masses	M_ν	0.0 [eV]

Table 7.1: Cosmological parameters used in the N-body simulations.

The BIGBOX simulation, conducted as part of the HalfDome project ([Bayer et al., 2024](#)), models using 6144^3 particles, a box with a side length of 3750 Mpc/h and periodic boundary conditions. We replicated the box 2 times along each axis (2^3 replications in total), in order to sample a large enough cosmological volume, such that we can cover the necessary redshift range (up to $z = 2.5$).

The TILED simulation covers a smaller volume with side length $L = 625$ Mpc/h, populated with 1024^3 particles and also with periodic boundary condition. This combination of box size and particle number is chosen to match the resolution of the BIGBOX simulation. To cover the same redshift range as the BIGBOX simulation, we replicated the box 10 times along each axis (10^3 replicas). Figure 7.1 showcases the spatial and redshift setup for the BIGBOX and TILED simulations used in cosmological studies.

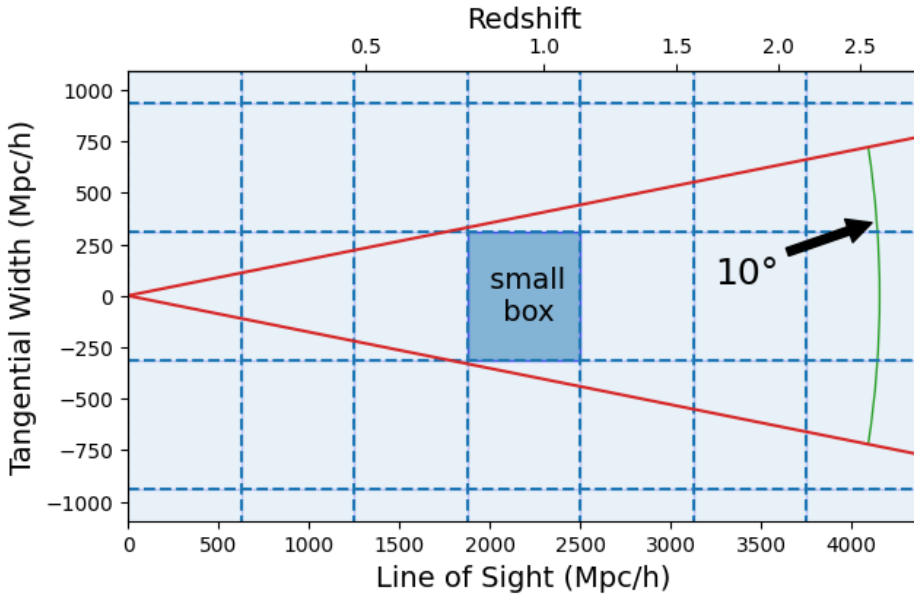


Figure 7.1: Spatial and redshift setup for the BIGBOX and TILED simulations. Dashed blue grids partition the overall simulation volume into smaller, manageable tiling regions where each tile is a replication of the TILED simulation. The lower horizontal axis represents the line-of-sight distance measured in Mpc/h, with the corresponding redshift values displayed on the top axis.

Both simulations commence at an initial redshift of $z = 9$, utilizing an initial linear matter power spectrum at $z = 0$ generated via the CLASS code ([Blas et al., 2011](#)). We evolved the simulations over

60 time steps, reaching the present day ($z = 0$). The resulting particle distributions are returned in 80 shells spanning scale factors from $a = 0.2$ to $a = 1.0$ with a uniform spacing of $\Delta a = 0.01$. At each scale factor a_i , particles within the shells are projected onto a HEALPix grid (Górski et al., 2005) with $N_{\text{side}} = 8192$, providing an angular resolution of approximately 0.43 arcminutes, to create mass maps.

The BIGBOX and TILED simulations were executed on the TACC (Texas Advanced Computing Center) cluster. Specifically, the BIGBOX simulations required approximately 4 hours per realization utilizing 2048 nodes, while the TILED simulations were completed in 2 hours per realization utilizing 64 nodes.

In total, we obtained 11 realizations of the BIGBOX simulation and 20 realizations of the TILED simulation, each initialized with distinct initial seeds. This ensemble of realizations allows us to robustly sample cosmic variance and ensures that our statistical analyses are not biased by any single simulation’s initial conditions.

It is important to note that the observer is positioned at the corner point shared by 8 replicated boxes for both the TILED and BIGBOX simulations. This placement induces the Box Replication Effect, characterized by a Kaleidoscope pattern of heavily tiled regions along the line of sight and near the equatorial regions (see Figure 7.2), particularly in directions parallel to the box edges. These replicated regions can introduce artificial correlations and anisotropies in the mass maps, potentially biasing our statistical measurements. To address this, we exclude the most heavily tiled regions from our analysis, ensuring that our results are not significantly impacted by the Box Replication Effect. A detailed discussion of this phenomenon and its implications is provided in Section 9.1.1.

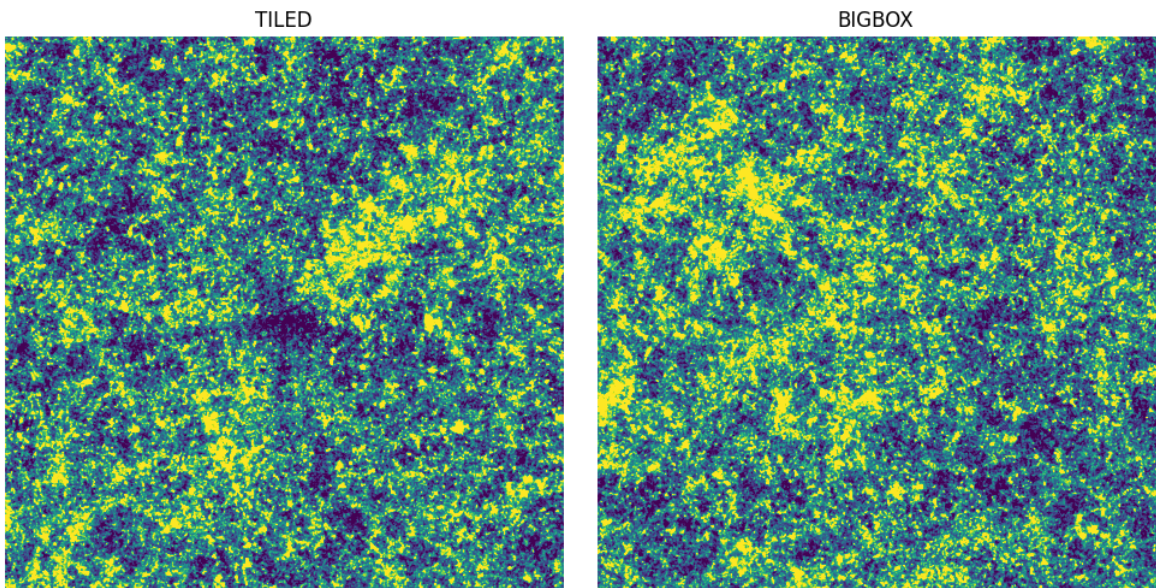


Figure 7.2: Illustration of a 5×5 patch around $(\theta, \phi) = (\pi/2, 0)$ extracted from the TILED and BIGBOX simulations. The TILED simulation exhibits a distinct Kaleidoscope pattern due to box replication, resulting in heavily tiled regions along the line of sight and near the equator.

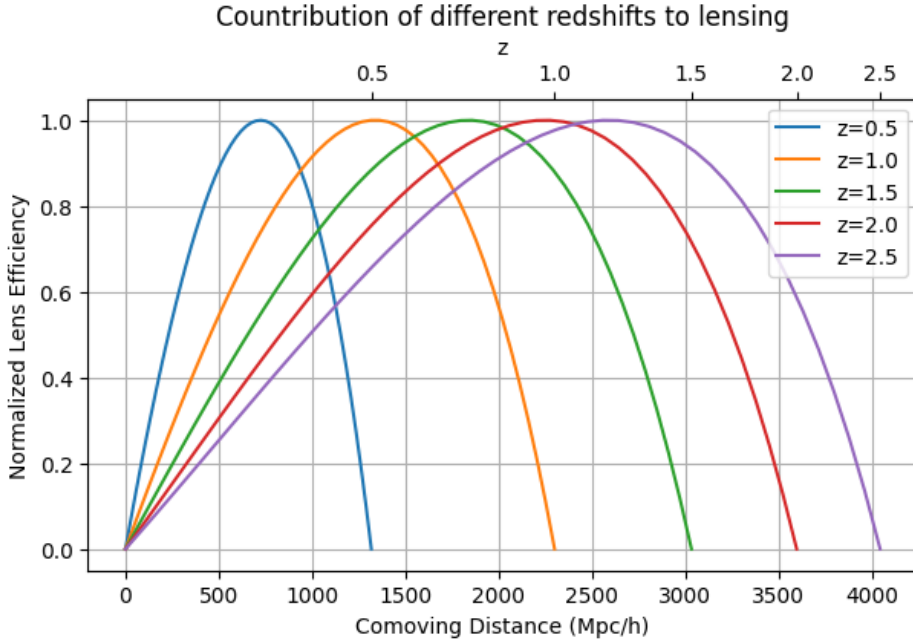


Figure 7.3: Normalized lensing efficiency as a function of comoving distance for multiple source redshifts. The lensing efficiency peaks at intermediate comoving distances, indicating regions where the distribution of matter enhances the gravitational lensing signal.

7.2 Generating Convergence Maps

Since we already have the projected mass map at each scale factor, we can calculate the convergence map at each redshift following the discussion in Section 3.2 and 6.5. Since the difference between TILED and BIGBOX simulations due to the super-sample effect shows up at the redshift $z \approx 1$, it is worthwhile to check the contribution from each redshift to the convergence map.

Figure 7.3 presents the normalized lensing efficiency as a function of comoving distance (measured in Mpc/h) for multiple source redshifts (z). The lensing efficiency curves exhibit peaks at intermediate comoving distances, indicating the regions where the distribution of matter along the line of sight most significantly enhances the gravitational lensing signal.

We considered source redshifts $z_s = [0.5, 1.0, 1.5, 2.0, 2.5]$ covering the range of distances relevant for current and future galaxy surveys. At redshift $z < 1$, both simulation suffer from the super-sample effect, while at redshift $z > 1$, the effect is more pronounced in the BIGBOX simulation. Figure 7.4 illustrates the convergence maps generated from the BIGBOX and TILED simulations for source redshift $z_s = 1.5$.

7.3 Incorporating Noise

In real observations, measurements of the lensing signal are contaminated by noise arising from the intrinsic shapes of galaxies and errors in shape measurements. This noise, referred to as shape noise,

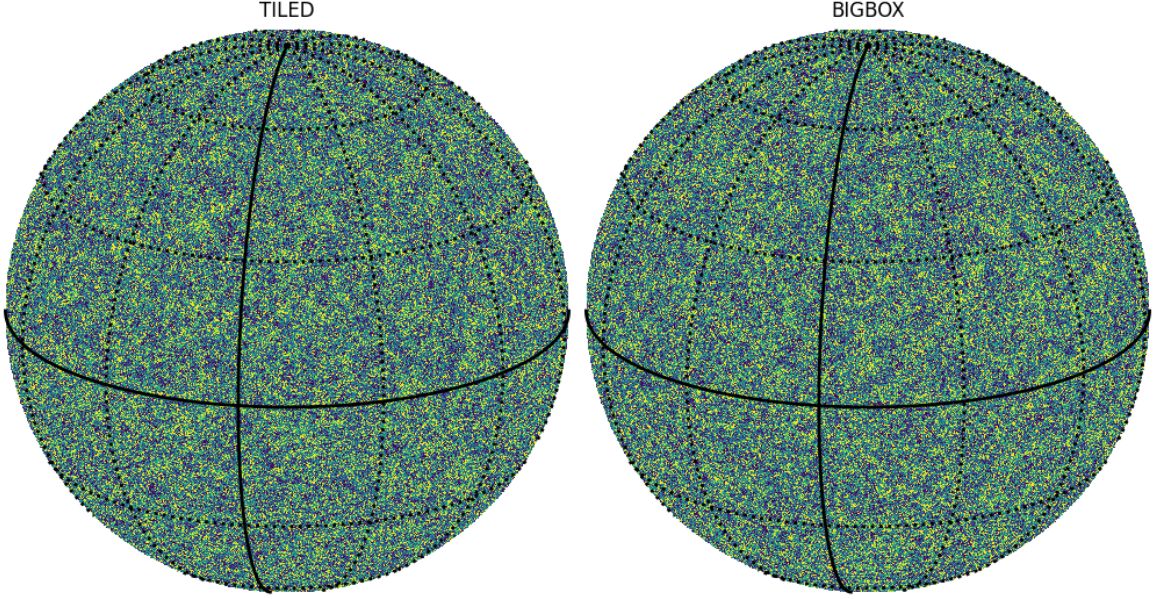


Figure 7.4: Convergence maps generated from the BIGBOX and TILED simulations for source redshift $z_s = 1.5$. The yellow regions represent positive convergence, while the blue regions indicate negative convergence. The convergence maps exhibit similar large-scale structures.

constitutes a significant source of uncertainty, particularly on small angular scales.

We considered four different surveys with varying galaxy number densities, as detailed in Table 1.1. The variance of the shape noise per pixel was calculated as:

$$\sigma_{\kappa, \text{noise}}^2 = \frac{\sigma_\epsilon^2}{2n_{\text{gal}} A_{\text{pix}}}, \quad (7.1)$$

where σ_ϵ is the intrinsic ellipticity dispersion of galaxies, set to $\sigma_\epsilon = 0.26$ ([Euclid Collaboration et al., 2019](#)), n_{gal} is the galaxy number density per square arcminute, and A_{pix} is the solid angle of a pixel, set to 0.43 arcminutes². We generated a Gaussian random field $n(\hat{\mathbf{n}})$ with the calculated variance and added it to the convergence maps:

$$\kappa_{\text{obs}}(\hat{\mathbf{n}}) = \kappa(\hat{\mathbf{n}}) + n(\hat{\mathbf{n}}). \quad (7.2)$$

7.4 Patch Extraction for Analysis

In order to simplify the analysis onto a flat patch, we extracted patches from the full-sky convergence maps. Each patch covers an area of $10^\circ \times 10^\circ$ and is uniformly distributed across the sky using a Fibonacci grid ([Swinbank & James Purser, 2006; Ferlito et al., 2023](#)). The center of each patch is positioned at the vertices of the Fibonacci grid defined by golden ratio spirals:

$$\sin \theta_i = \frac{2i}{2N+1}, \quad \phi_i = \frac{2\pi i}{\varphi}, \quad -N \leq i \leq N, \quad -\frac{\pi}{2} \leq \theta_i \leq \frac{\pi}{2}, \quad (7.3)$$

where N is the number of patches and $\varphi = (1 + \sqrt{5})/2$ is the golden ratio. The visualization of the Fibonacci grid is shown in Figure 7.5.

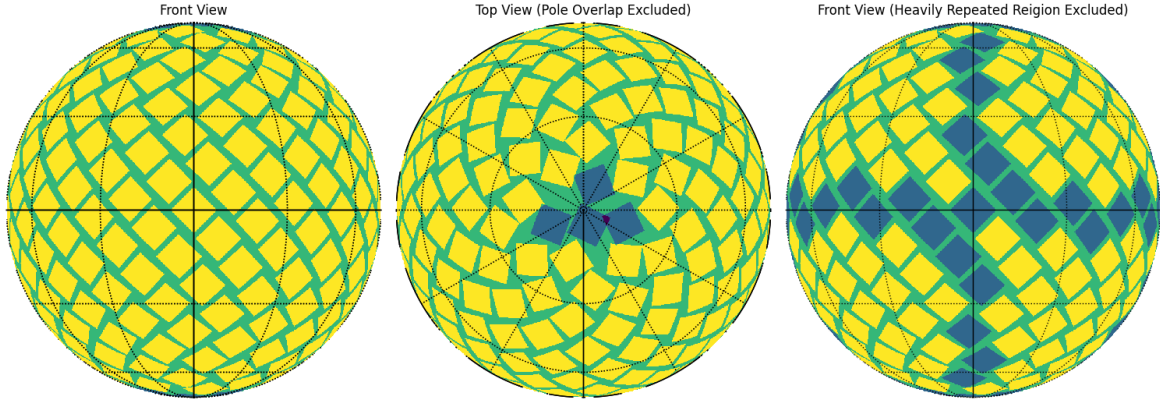


Figure 7.5: Visualization of the Fibonacci grid with $N_{\text{patches}} = 273$ patches, each covering approximately $10 \times 10 \text{ deg}^2$. After the optimization and masking, the number of patches is reduced to $N_{\text{patches}} = 194$, effectively covering 47% of the sky. Each panel shows the patches distribution on the Front, Top view and the final patches from the front.

Following Ferlito et al. (2023), we can obtain the maximum number of patches by align the diagonal of square patches with the longitude lines. Nonetheless, we have to extract patches which their sides are aligned with the latitude lines due to the programming reason. Therefore, we first obtain a patch with wider side length and then rotate and crop the patch to get the desired shape.

Before extracting the patches, we first optimize the number of patches to extract from the full-sky map. The number of patches, denoted N_{patches} , was optimized to ensure that individual patches do not overlap, except in regions near the poles where overlapping patches were subsequently discarded. Each patch on the full-sky map is defined as:

$$\begin{aligned} & (\theta_i - R_{\text{patch}}, \phi_i + R_{\text{patch}} \sin \theta_i), \quad (\theta_i + R_{\text{patch}}, \phi_i + R_{\text{patch}} \sin \theta_i), \\ & (\theta_i - R_{\text{patch}}, \phi_i - R_{\text{patch}} \sin \theta_i), \quad (\theta_i + R_{\text{patch}}, \phi_i - R_{\text{patch}} \sin \theta_i) \end{aligned} \quad (7.4)$$

with $R_{\text{patch}} = 5\sqrt{2} \text{ deg}$, the half diagonal length of the patch. The optimization process commenced with an initial count of $N_{\text{patches}} = 400$ and involved iteratively reducing this number until a configuration was achieved wherein the patches remained non-overlapping, except for centers located within $2R_{\text{patch}}$ of the poles, that is $|\theta_i| \geq 2R_{\text{patch}}$ and $|\phi_i| \leq \pi - 2R_{\text{patch}}$. This threshold was selected to ensure that the patches were not including the poles.

After optimization and masking, the number of patches was set to $N_{\text{patches}} = 273$, effectively reducing to $N_{\text{patches}} = 265$, effectively cover 64% of the sky. Additionally, patches include points heavily tiled along with line of sight are excluded to avoid severe Box Replication Effect (see Sec. 9.1.1 for further check). Hence, the final number of patches used for analysis is $N_{\text{patches}} = 194$, covering 47% of the sky.

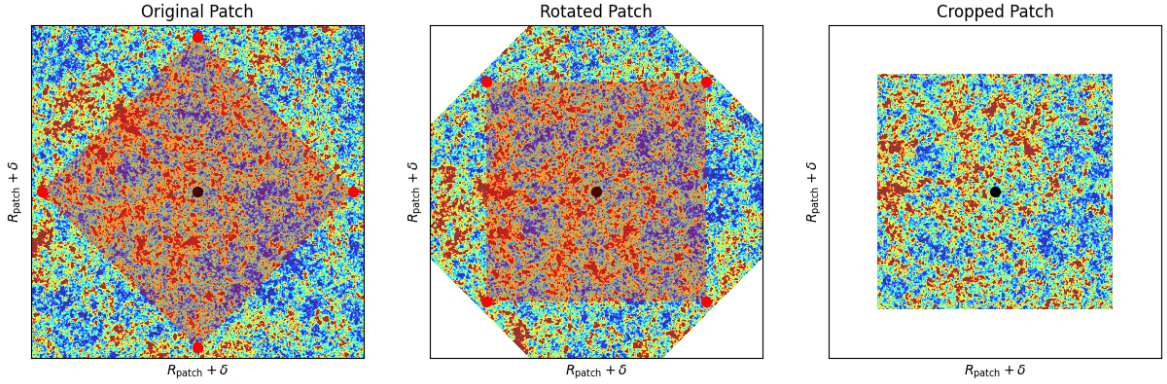


Figure 7.6: Extraction of a patch from the full-sky convergence map using a Fibonacci grid. The patch covers an area of $10^\circ \times 10^\circ$ and is centered at the vertices of the Fibonacci grid. From the left to the right, the panels show the original extracted patch, patch rotated 45° around the center and the final patch after the second rotation. The red shaded region represents the final patch we used for analysis.

For a Fibonacci grid center characterized by coordinates (θ_i, ϕ_i) , we first employed the `gnomview` function from the `healpy` library (Zonca et al., 2019) to project each spherical patch onto a flat plane via a gnomonic projection. Then for each patch, we rotated them by 45° around the center of the patch to align the diagonal of the patch with the longitude lines. Finally, we cropped the patch according to the corresponding vertices.

Figure 7.6 showcases an extracted patch from the full-sky convergence map, and additional handling of the patches to get the desired shape.

Each patch is represented by a 2048×2048 grid of pixels, resulting in a pixel size of:

$$\Delta\theta = \frac{10^\circ}{2048} \approx 0.00488^\circ \approx 0.293' \quad \text{per pixel.} \quad (7.5)$$

For each realization, the covariance is computed using 194 patches extracted from the full-sky map of each simulation. Therefore, we obtain a total of 2134 patches from the BIGBOX simulation and 3880 patches from the TILED simulation.

7.5 Gaussian Smoothing

Shape noise predominantly affects small angular scales. To mitigate this noise and enhance the detection of the underlying lensing signal, we applied Gaussian smoothing to the noisy convergence maps. The Gaussian filter used is defined by:

$$W(\theta) = \frac{1}{\pi\theta_G^2} \exp\left(-\frac{\theta^2}{\theta_G^2}\right), \quad (7.6)$$

where θ is the angular distance from the center of the filter, and θ_G is the smoothing scale. For our analysis, we selected $\theta_G = 2'$, $5'$, $8'$, and $10'$.

By convolving the noisy convergence map with the Gaussian filter, we obtained the smoothed convergence map:

$$\kappa_{\text{smoothed}}(\hat{\mathbf{n}}) = \int d\Omega' W(|\hat{\mathbf{n}} - \hat{\mathbf{n}}'|) \kappa_{\text{obs}}(\hat{\mathbf{n}}'). \quad (7.7)$$

Figure 7.7 demonstrates the application of Gaussian smoothing to a noisy convergence map. The figure presents four panels, each corresponding to a different smoothing scale: $\theta_G = 2'$, $5'$, $8'$, and $10'$. As the smoothing scale increases, the convolution with the Gaussian filter effectively reduces small-scale noise, as evidenced by the diminishing small-scale fluctuations in the map.

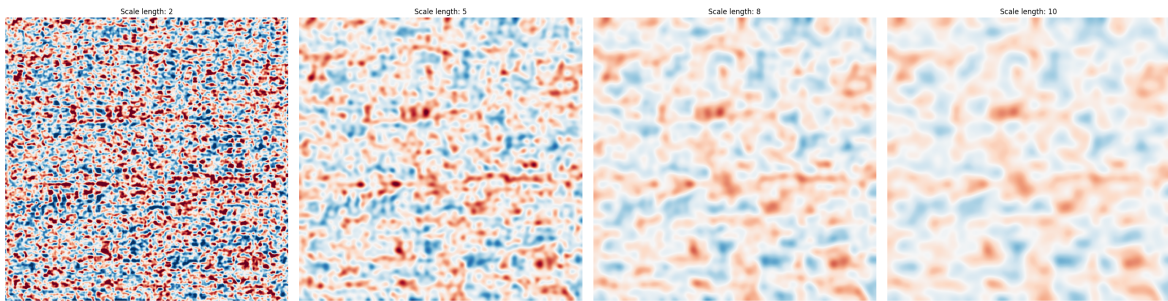


Figure 7.7: Effect of Gaussian smoothing on a noisy convergence map. Each panel shows the result of applying a Gaussian filter with a different smoothing scale $\theta_G = 2'$, $5'$, $8'$, and $10'$. As the smoothing scale increases, small-scale noise is progressively suppressed, and large-scale structures become more prominent. This demonstrates how Gaussian smoothing effectively reduces shape noise while enhancing the detection of the underlying signal.

For the non-Gaussian statistics, we adapt Gaussian smoothing. The statistics are then calculated from the smoothed convergence maps. The application of smoothing kernel to the convergence maps wash out the small-scale structures and therefore change the range of κ values. To avoid the smoothing issues and the complex binning to consider, we normalize κ values by the standard deviation of each patch's convergence map, σ_κ . Figure 7.8 shows the average standard deviation of the noiseless convergence maps for the BIGBOX and TILED simulations. Obviously, the standard deviation of convergence maps goes higher as the redshift or the smoothing scale decreases, while subtle difference between the BIGBOX and TILED simulations can be observed.

7.6 Measurements

In order to characterize the influence of super-sample covariance on higher-order statistics, this study concentrates on the bispectrum, probability distribution function (PDF), peak counts, minima counts, and Minkowski functionals.

Table 7.2 delineates the range of values and the computational subroutines employed for each statistical measure.

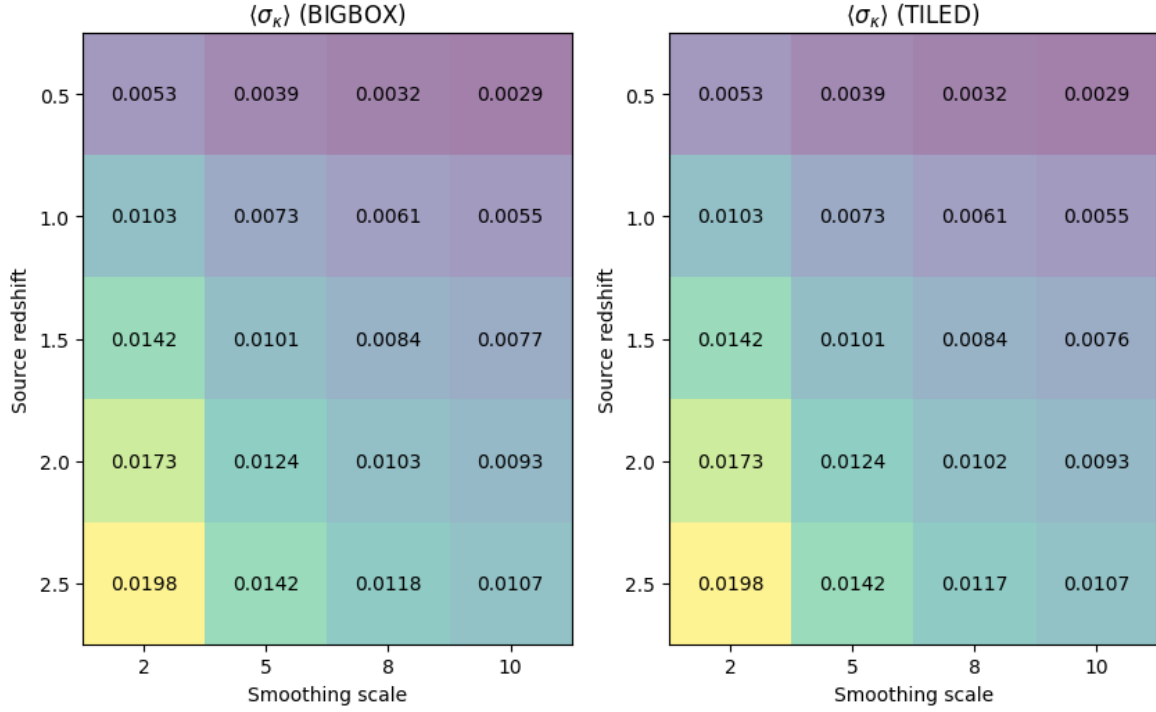


Figure 7.8: Average standard deviation of the noiseless convergence maps for the BIGBOX and TILED simulations. The standard deviation increases with redshift and smoothing scale, with a subtle difference between the BIGBOX and TILED simulations.

Statistic	Range	Subroutine (Sky Patch)
Angular Power Spectrum	$300 \leq \ell \leq 3000$	lenstools.powerSpectrum
Bispectrum	$300 \leq \ell \leq 3000$	lenstools.bispectrum
Peak Counts	$-4 \leq \kappa/\sigma_\kappa \leq 4$	lenstools.peakCount
Minima Counts	$-4 \leq \kappa/\sigma_\kappa \leq 4$	lenstools.peakCount
Probability Distribution Function (PDF)	$-4 \leq \kappa/\sigma_\kappa \leq 4$	lenstools.pdf
Minkowski Functionals	$-4 \leq \kappa/\sigma_\kappa \leq 4$	own implementation

Table 7.2: Summary of the statistical measures employed in this investigation, including their respective value ranges and computational subroutines utilized for analyses.

7.6.1 Angular Power Spectrum

The angular power spectrum ($C_\ell^{\kappa\kappa}$) is calculated directly from the simulated convergence maps using `lenstools` (Petri, 2016) without performing any prior smoothing of the maps. We consider an angular multipole range from $\ell = 300$ to $\ell = 3000$ with 8 logarithmically spaced bins. The number of bins is chosen to match the multipole selection in the HSC Y3 cosmic shear analysis (Dalal et al., 2023). As the goal of this work is to investigate higher-order statistics, we choose the lower limit of $\ell = 300$ to avoid the large-scale regimes. The upper limit of $\ell = 3000$ is selected to ensure that the analysis reach the small-scale regime where the super-sample effect is more pronounced.

For a reference, we compute the theoretical prediction using `Halofit` (Takahashi et al., 2012) and compare it with the measured angular power spectrum. The theoretical prediction is calculated

using the same cosmological parameters as the simulations.

7.6.2 Bispectrum

The bispectrum ($B_{\ell_1 \ell_2 \ell_3}^{\kappa \kappa \kappa}$) is computed from the unsmoothed convergence maps using `lenstools`. We consider three distinct configurations: equilateral ($\ell_1 = \ell_2 = \ell_3$), squeezed ($\ell_1 = \ell_2 = 10\ell_3$), and isosceles ($\ell_1 = \ell_2 = 2\ell_3$). Those configurations are chosen to capture the different shapes of the bispectrum and provide complementary information about the underlying matter distribution. The bispectrum calculations are confined within the multipole range $\ell \in [300, 3000]$ with 8 logarithmically spaced bins, same as the angular power spectrum. Though the bispectrum is more sensitive to the noise and the small-scale structures, we choose the same multipole range to compare the results with the angular power spectrum.

For the bispectrum, we also compute the theoretical prediction using the `BiHalofit` code ([Takahashi et al., 2020](#)) and compare it with the measured bispectrum. The theoretical prediction is calculated using the same cosmological parameters as the simulations.

7.6.3 PDF

The PDF of the convergence field is computed from the smoothed convergence maps using `lenstools`. The PDF is calculated within the normalized range $-4 \leq \kappa/\sigma_\kappa \leq 4$, linearly divided into 8 bins. σ_κ denotes the standard deviation of each patch's convergence map.

The theoretical prediction for the PDF is calculated using the `hmpdf` code [Thiele et al. \(2020\)](#) and compared with the measured PDF. The theoretical prediction is calculated based on the same linear matter power spectrum as the simulations.

7.6.4 Peak/Mimima Counts

The peak and minima counts are computed from the smoothed convergence maps using `lenstools`. The peak and minima counts are calculated within the normalized range $-4 \leq \kappa/\sigma_\kappa \leq 4$, linearly divided into 8 bins. Thought the highest/lowest peaks contain only few data points, we choose to include them in the analysis to match the range of the PDF.

7.6.5 Minkowski Functionals

The Minkowski functionals are computed from the smoothed convergence maps using our own implementation naively follow the definition in Section 4.5. They are calculated within the normalized range $-4 \leq \kappa/\sigma_\kappa \leq 4$, linearly divided into 8 bins. We show $\sigma_1 = \sqrt{\kappa_x^2 + \kappa_y^2}$ which used to calculate the Minkowski functionals in Figure 7.9. The values decrease as the smoothing scale increases, while the difference between the BIGBOX and TILED simulations or the redshifts is subtle.

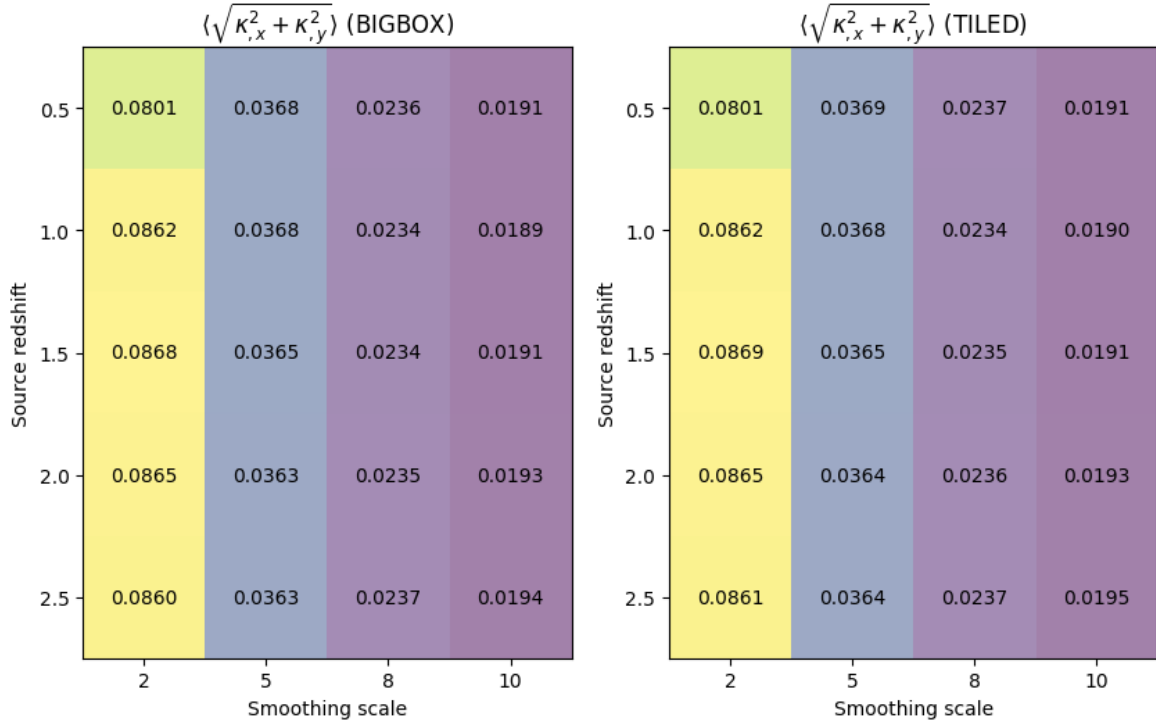


Figure 7.9: Average $\sigma_1 = \sqrt{\kappa_x^2 + \kappa_y^2}$ of the noiseless convergence maps for the BIGBOX and TILED simulations. They are calculated for the smoothing scales $\theta_G = 2', 5', 8',$ and $10'$. The values decrease as the smoothing scale increases, while the difference between the BIGBOX and TILED simulations or the redshifts is subtle.

7.6.6 Covariance Matrix Estimation

Following the measurement phase, this study examines the influence of super-sample covariance on the covariance matrices associated with the aforementioned statistical measures. To achieve this, we employ an unbiased estimator for the covariance matrix as previously defined in Equation 7.8.

$$\text{Cov}(\mathcal{O}_i, \mathcal{O}_j) = \frac{1}{N_{\text{sim}} - 1} \sum_{n=1}^{N_{\text{sim}}} (\mathcal{O}_i^{(n)} - \langle \mathcal{O}_i \rangle)(\mathcal{O}_j^{(n)} - \langle \mathcal{O}_j \rangle), \quad (7.8)$$

Additionally, we also compute the correlation matrix for each statistical measure to investigate the interdependence between different scales and configurations. The correlation matrix is defined as:

$$\rho_{ij} = \frac{\text{Cov}(\mathcal{O}_i, \mathcal{O}_j)}{\sqrt{\text{Cov}(\mathcal{O}_i, \mathcal{O}_i)\text{Cov}(\mathcal{O}_j, \mathcal{O}_j)}}, \quad (7.9)$$

where \mathcal{O}_i and \mathcal{O}_j represent the i -th and j -th statistical measures, respectively.

After the covariance and correlation matrices are computed for both the BIGBOX and TILED simulations, we compare the matrices to quantify the impact of super-sample covariance on the statistical measures. The comparison is conducted by calculating the ratio between the covariance and correlation matrices of the BIGBOX and TILED simulations.

In the case of correlation matrices, we exclude the diagonal elements—since they are always unity—when calculating the ratio. For covariance matrices, the ratio is calculated over the entire matrix.

Regarding ℓ -binned statistics, we determine the ratio across all bins. For ν -binned statistics, we exclude the first and last bins from the ratio calculation due to their limited data points and unreliability.

Chapter 8

Results

Contents

8.1 Overview	75
8.2 Effects of Noise	76
8.3 Effects of Smoothing Scale	76

In this chapter, we initiate a comprehensive analysis by systematically comparing each statistical measure derived from our simulations. We focus on evaluating the mean values, covariance matrices, and correlation matrices obtained from the BIGBOX and TILED simulations to assess their consistency and understand the underlying discrepancies.

8.1 Overview

Figures 8.1 through 8.12 provide detailed visualizations of the mean values, variances, covariance matrices, and correlation matrices for each statistical measure under consideration. For each statistic, one figure illustrates the comparison of mean values and variances, while another figure presents the comparison of covariance and correlation matrices.

From these figures, we observe that the mean values of most statistical measures exhibit excellent agreement between the BIGBOX and TILED simulations, with differences remaining below 1% across the majority of the studied range. However, notable deviations occur at low ν values for peak counts, minima, and the Minkowski Functionals V_1 and V_2 . These deviations are attributed to the limited resolution of the simulations, which affects the accurate detection of regions with the lowest density contrasts.

Analyzing the covariance matrices reveals that, except for the bispectrum, the ratios of covariance matrix elements between the BIGBOX and TILED simulations are consistently greater than unity. This indicates that the BIGBOX simulations yield higher covariance values compared to the TILED simulations, and this discrepancy becomes more pronounced at higher source redshifts. The

bispectrum, on the other hand, exhibits noisy covariance matrices without a clear trend, making it challenging to draw definitive conclusions for this statistic.

Examining the correlation matrices further, we focus on the off-diagonal elements to assess the degree of inter-bin correlations. For statistical measures that are not inherently correlated, the off-diagonal elements remain close to unity, as expected. In contrast, the power spectrum shows off-diagonal elements that exceed unity, displaying a clear increasing trend with higher source redshifts. This behavior aligns with theoretical predictions of super-sample covariance effects, as detailed in [Takada & Hu \(2013\)](#), suggesting that larger-scale modes beyond the survey volume contribute to the observed correlations.

Overall, these findings support the hypothesis that super-sample covariance significantly impacts the statistical measures derived from our simulations. The discrepancies observed between the BIG-BOX and TILED simulations emphasize the importance of considering super-sample effects in cosmological analyses. We will explore these effects in greater depth and seek further validation in the subsequent discussion chapter.

8.2 Effects of Noise

To assess the impact of observational noise, we have introduced five different shape noise levels into the simulations. Due to the significant influence of noise on higher-order statistics, the bispectrum has been excluded from this part of the analysis.

Figures [8.13](#) and [8.14](#) illustrate how the average ratios of covariance matrices and correlation matrices change with varying shape noise levels. Except for the angular power spectrum, the non-Correlation statistics exhibit stable covariance ratios across different noise levels.

Figures [8.17](#) and [8.18](#) demonstrate how the ratios of covariance matrices for the angular power spectrum and the non-correlation statistics change with different shape noise levels. The results indicate that the angular power spectrum and minima are particularly sensitive to the shape noise level, exhibiting significant variations in their covariance matrices. In contrast, other non-correlation statistics remain more robust against changes in the shape noise level, maintaining relatively stable off-diagonal elements in their covariance matrices.

8.3 Effects of Smoothing Scale

To evaluate the impact of smoothing on the statistical measures, we have applied four different smoothing scales to the simulations. Smoothing affects the resolution of the convergence maps and can influence the detection of small-scale structures.

Figures [8.15](#) and [8.16](#) show how the average ratios of covariance matrices and correlation matrices change with varying smoothing scales. The ratios become more unstable due to the smoothing effect

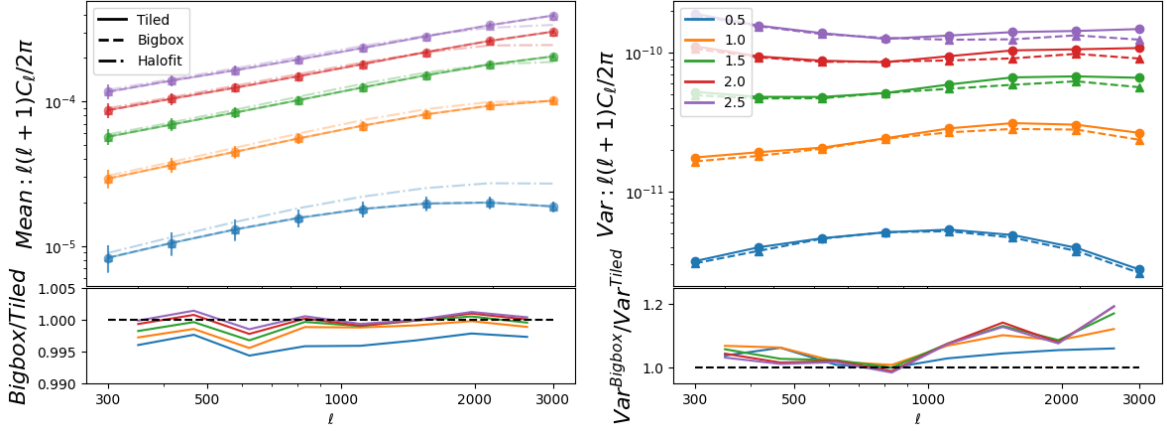


Figure 8.1: Comparison of the mean values of the angular power spectrum ($C_{\ell}^{\kappa\kappa}$) for different source redshifts ($z_s = 0.5, 1.0, 1.5, 2.0, 2.5$) obtained from the BIGBOX (solid lines) and TILED (dashed lines) simulations. The lower subplots show the ratio of the TILED to BIGBOX mean values, with a reference line at unity to facilitate the assessment of agreement between the two simulations.

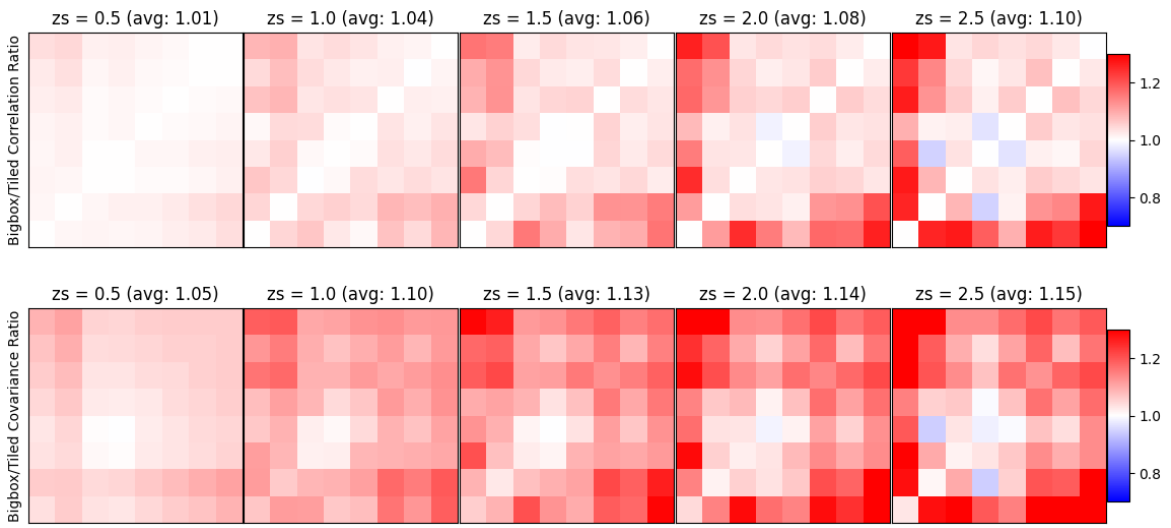


Figure 8.2: Comparison of the covariance matrices and correlation matrices of the angular power spectrum ($C_{\ell}^{\kappa\kappa}$) between the BIGBOX and TILED simulations for various source redshifts ($z_s = 0.5, 1.0, 1.5, 2.0, 2.5$). The displayed ratios represent the element-wise division of the covariance and correlation matrices from the TILED simulations by those from the BIGBOX simulations. The ‘avg’ denotes the average ratio of the considered matrix elements.

washing out small-scale structures.

Figure 8.19 illustrates the effects of smoothing scale on non-Correlation statistical measures. As the smoothing scale increases, the finer structures in the convergence maps are blurred, leading to changes in the statistical properties. The blank bins that previously contained little or no signal begin to be filled due to the spread of signals from neighboring bins, while the overall signal intensity is redistributed.

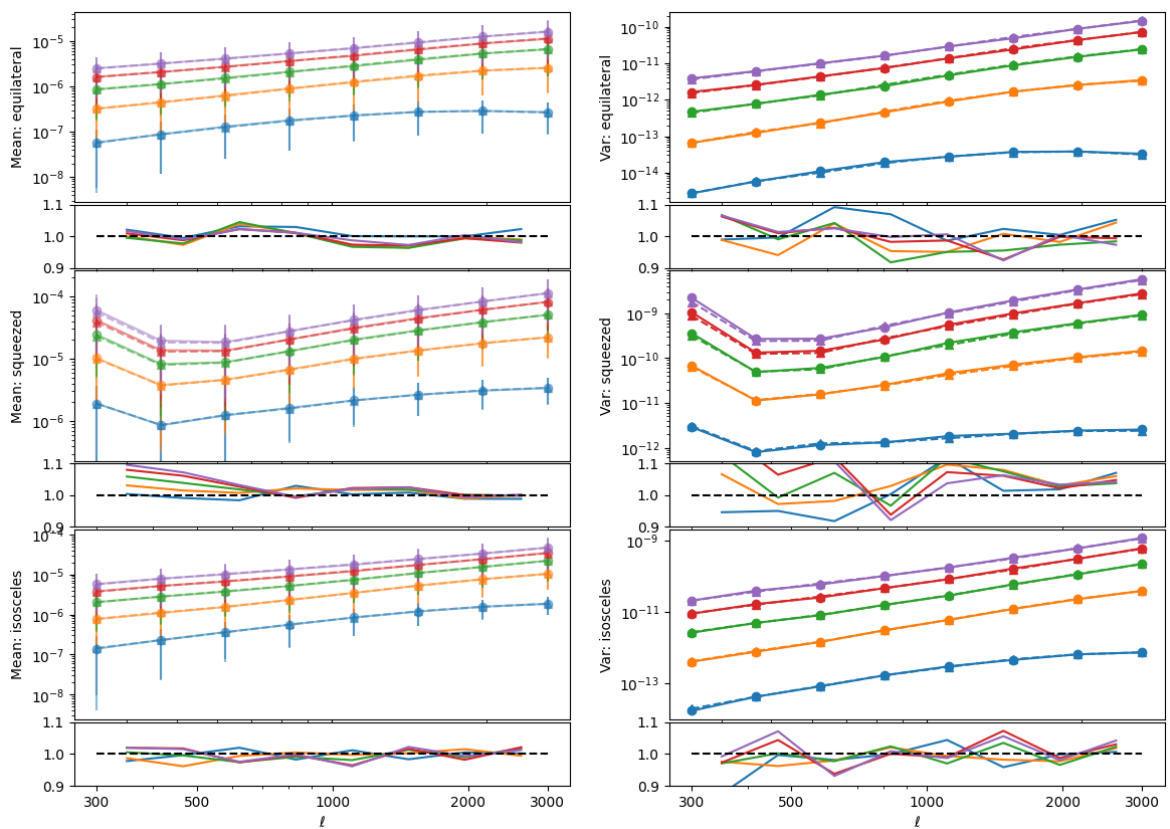


Figure 8.3: Same as Figure 8.1, but for the bispectrum.

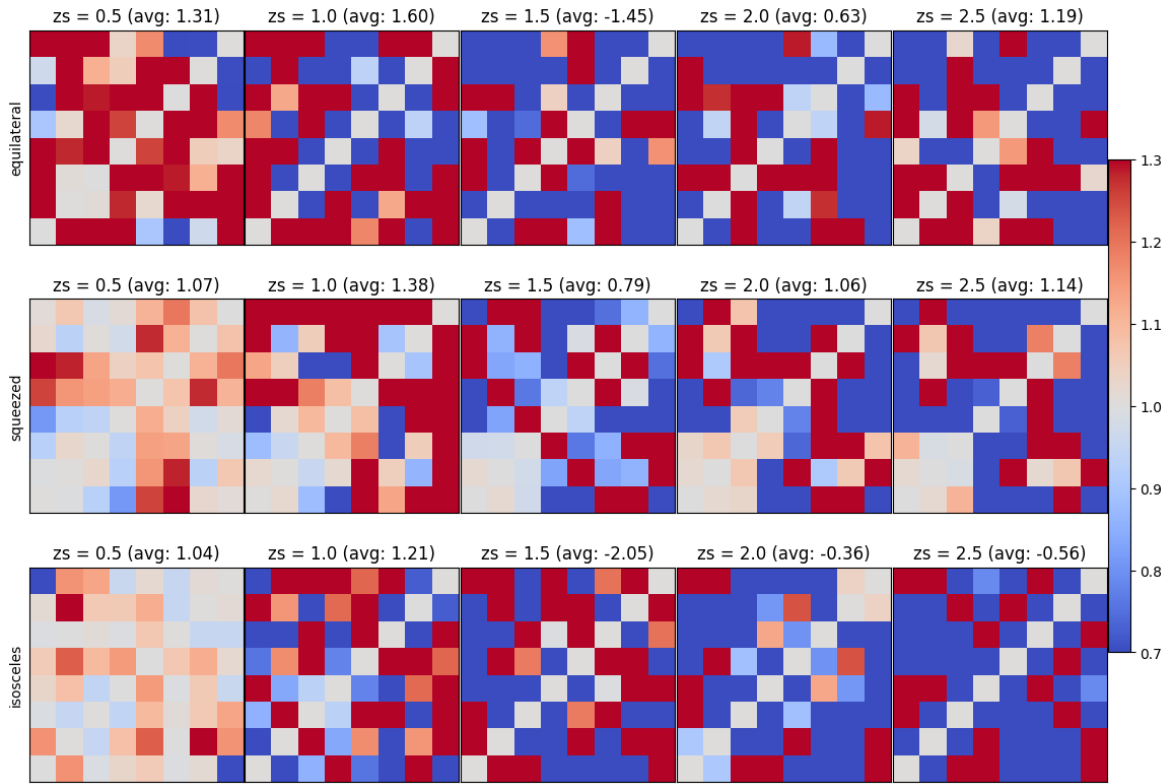
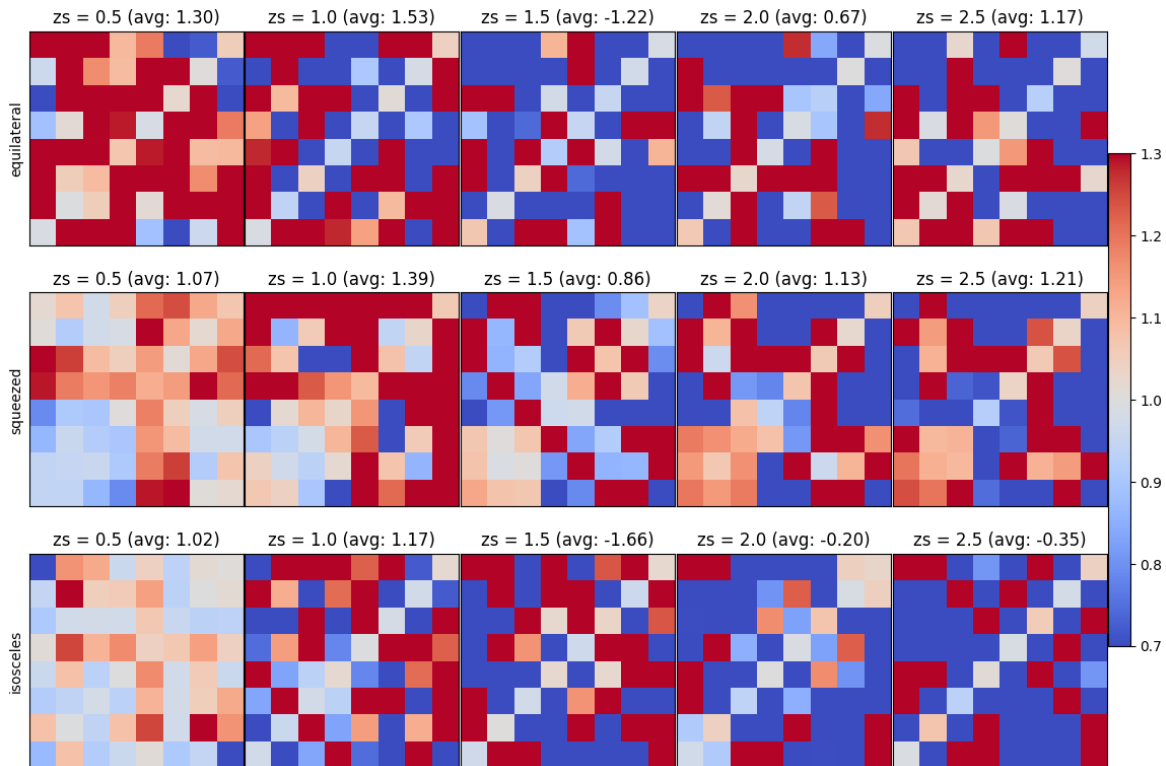


Figure 8.4: Similar to Figure 8.2, but for the correlation (upper) and covariance (lower) of bispectrum. The noisy nature of the bispectrum covariance makes it challenging to discern clear trends between the simulations.



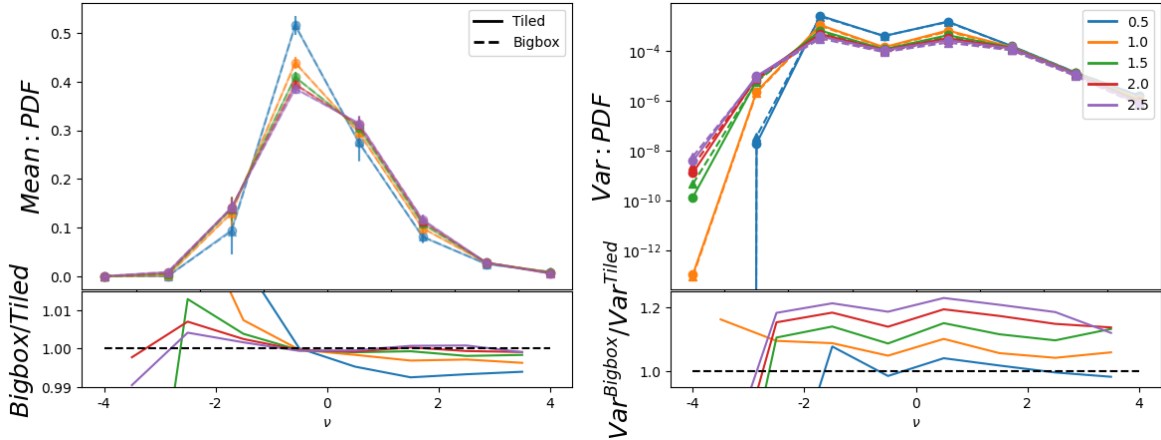


Figure 8.5: Same as Figure 8.1, but for the probability density function (PDF) of the convergence field. The comparison highlights the agreement in mean PDF values between the simulations across different redshifts.

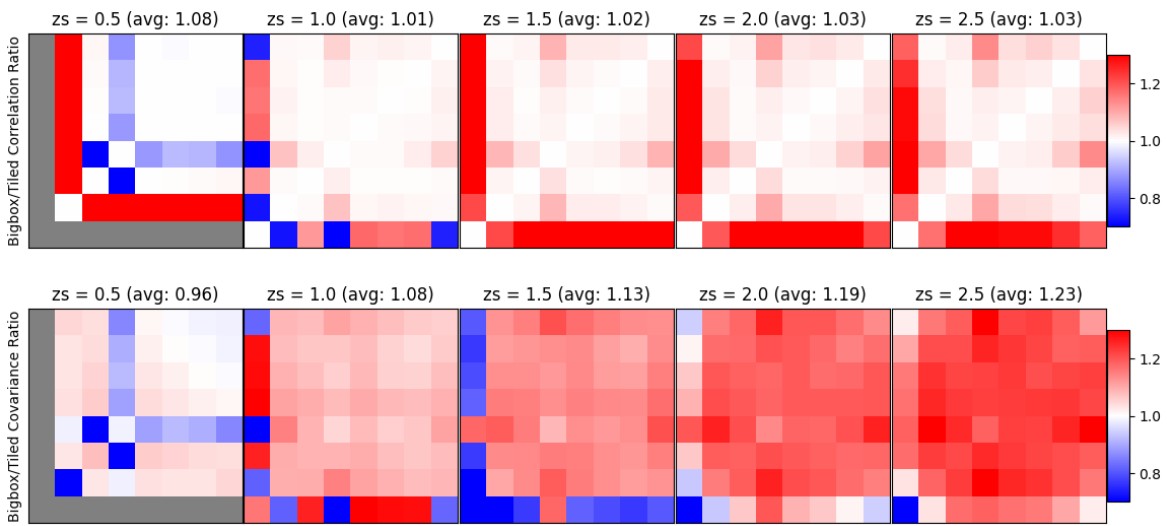


Figure 8.6: Same as Figure 8.2, but for the covariance matrices of the PDF. The covariance ratios indicate higher covariance in the BIGBOX simulations, particularly at higher redshifts.

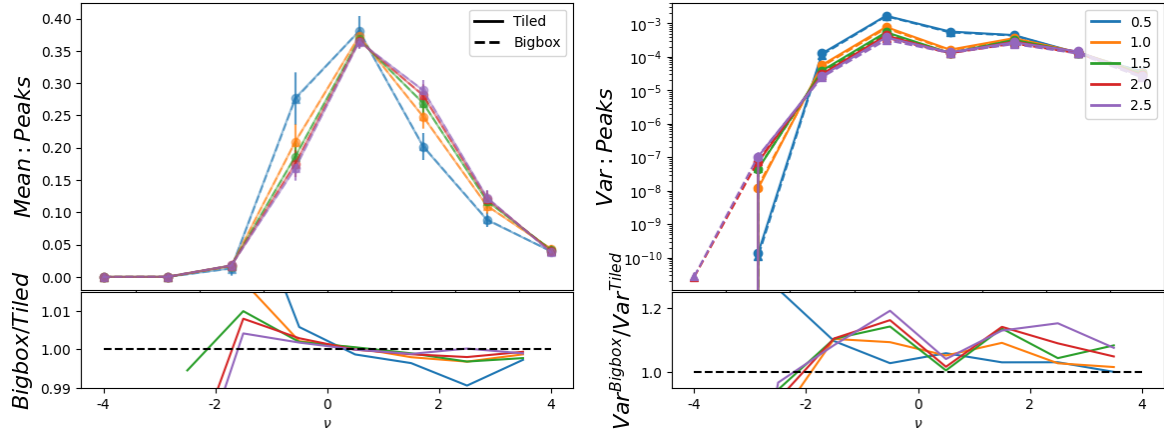


Figure 8.7: Same as Figure 8.1, but for peak counts in the convergence maps. The analysis reveals deviations at low ν values due to resolution limitations affecting low-density regions.

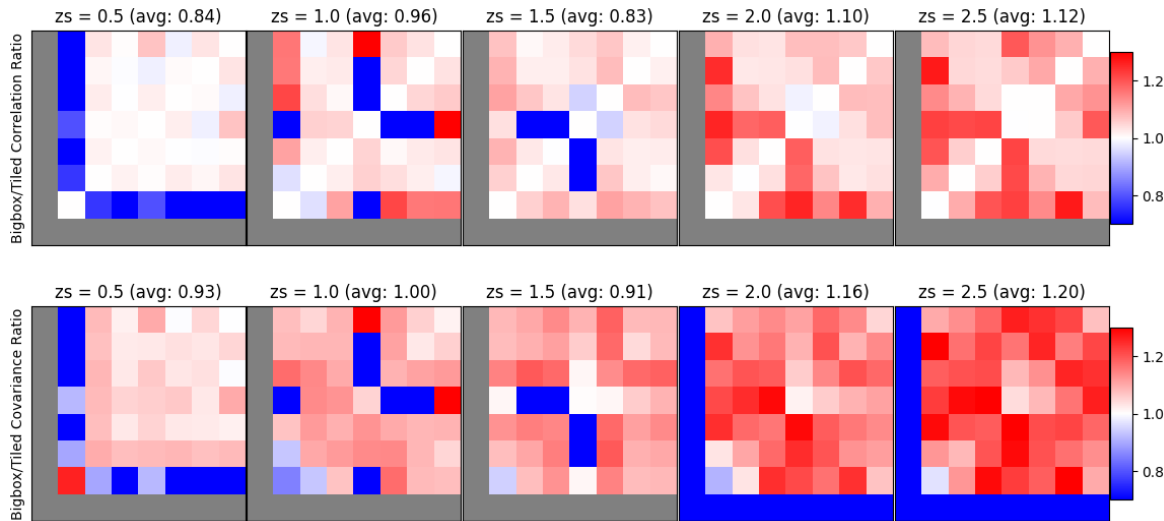


Figure 8.8: Same as Figure 8.2, but for the covariance matrices of peak counts. The covariance ratios suggest increased covariance in the BIGBOX simulations, with pronounced effects at higher redshifts.

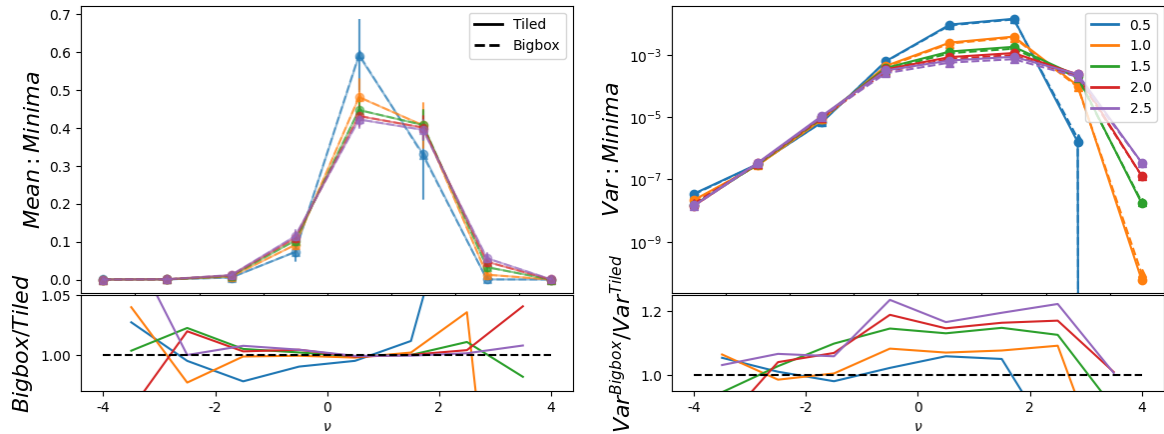


Figure 8.9: Same as Figure 8.1, but for minima in the convergence maps. The comparison underscores the simulation's limitations at resolving low-density minima accurately.

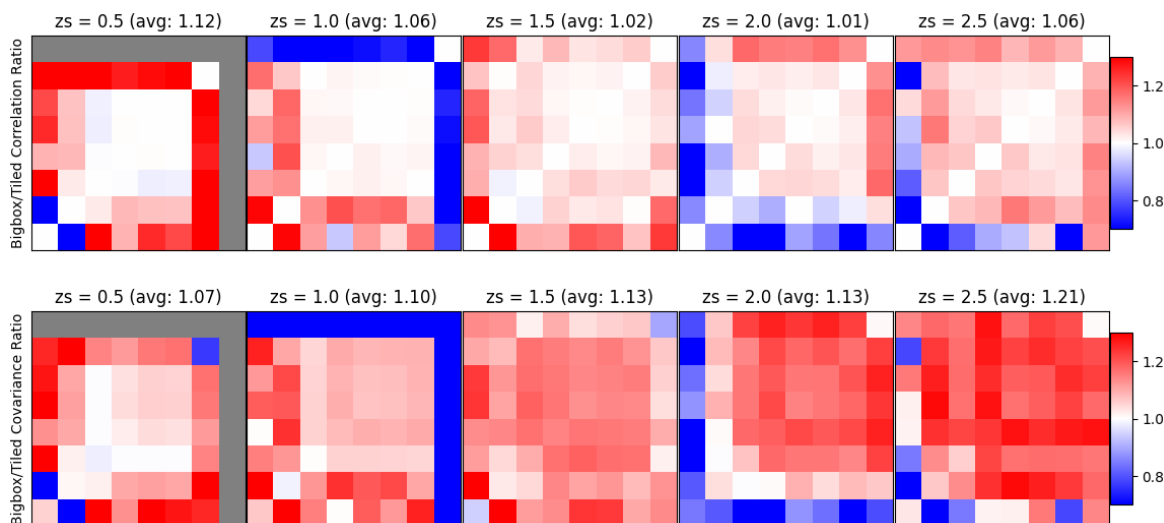


Figure 8.10: Same as Figure 8.2, but for the covariance matrices of minima. The covariance ratios reflect higher values in the BIGBOX simulations, consistent with other statistical measures.

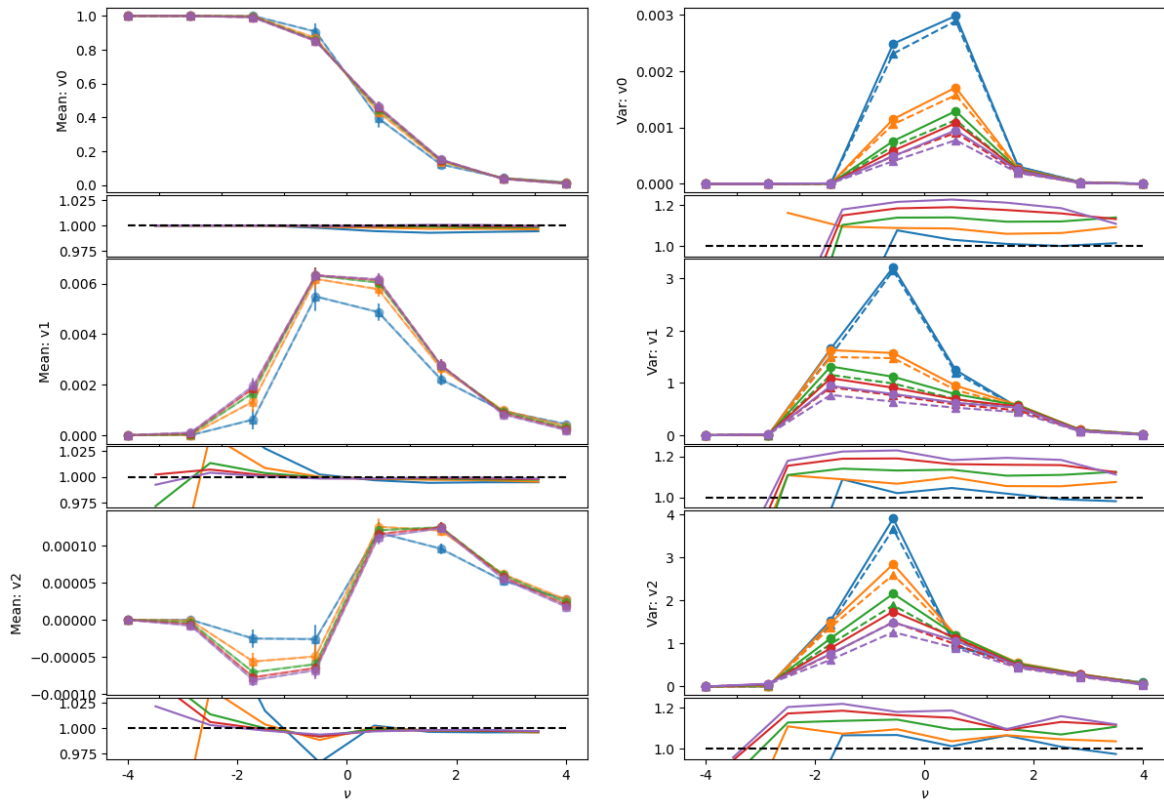


Figure 8.11: Same as Figure 8.1, but for Minkowski Functionals (area V_0 , perimeter V_1 , and genus V_2). The agreement in mean values between simulations is generally good, with some discrepancies at extreme density thresholds.

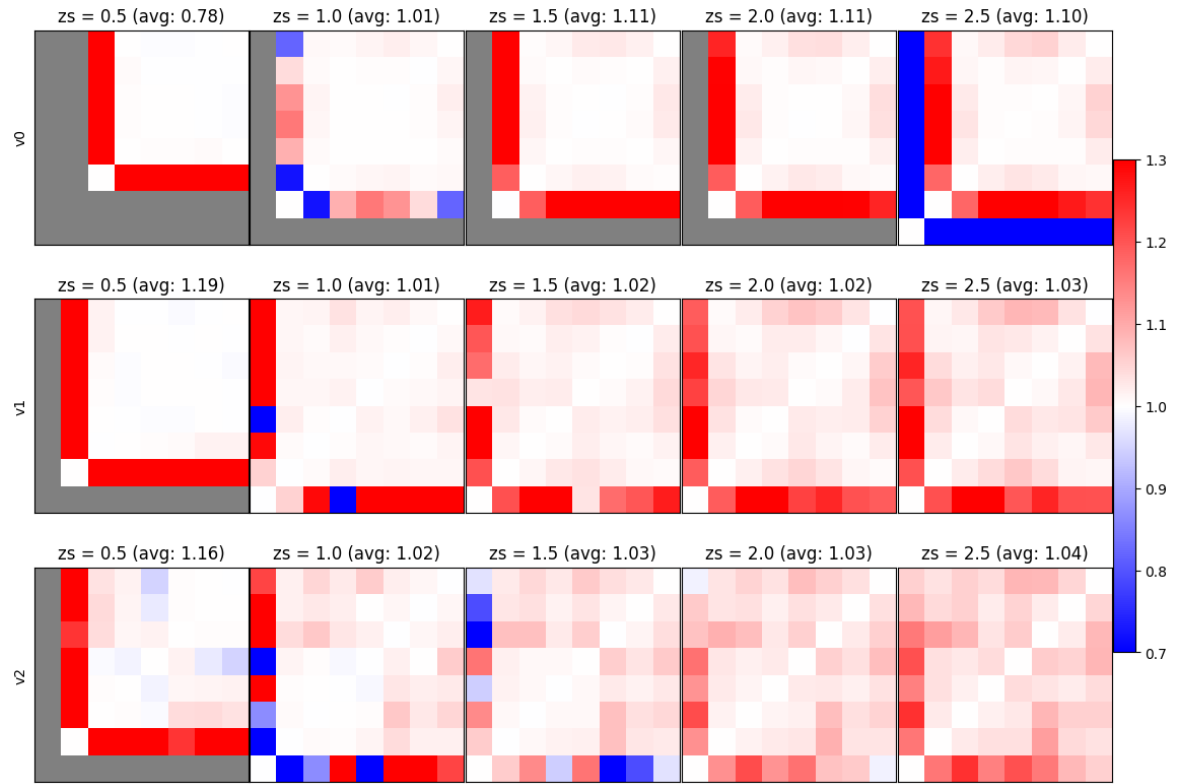
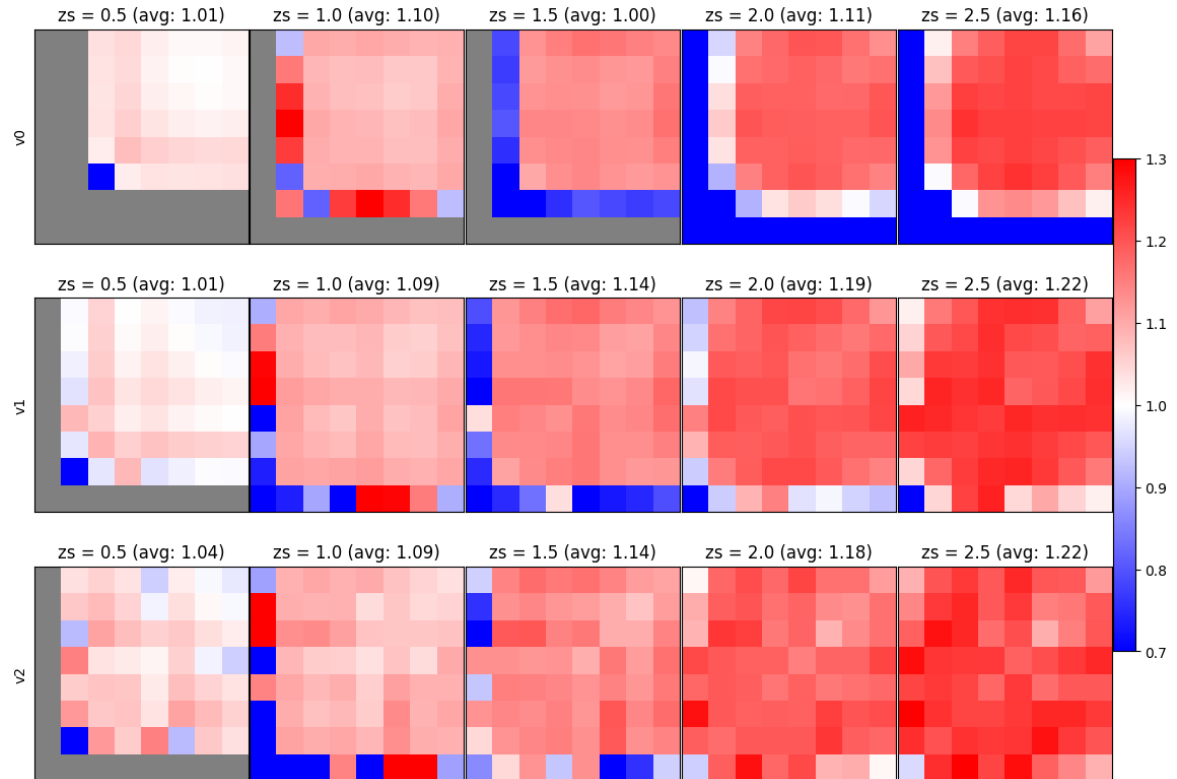


Figure 8.12: Similar to Figure 8.2, but for the correlation (upper) and covariance (lower) of Minkowski Functionals.



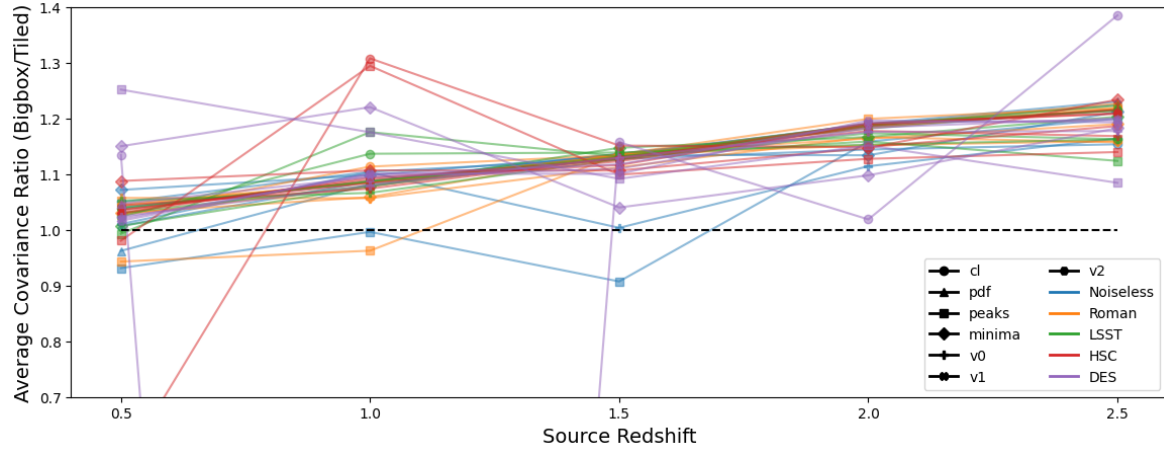


Figure 8.13: Average ratio of covariance matrices of statistical measures between the BIGBOX and TILED simulations for different shape noise levels (see Table 1.1). The increasing trend indicates does not affected by the noise level.

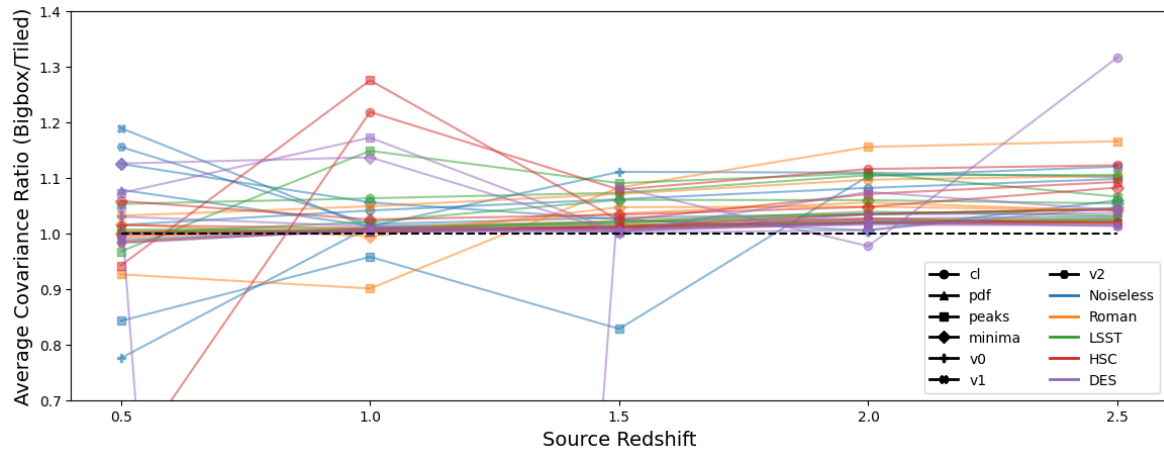


Figure 8.14: Same as Figure 8.13, but for the correlation matrices. The off-diagonal elements compared to the diagonal elements do not show a clear trend with noise levels.

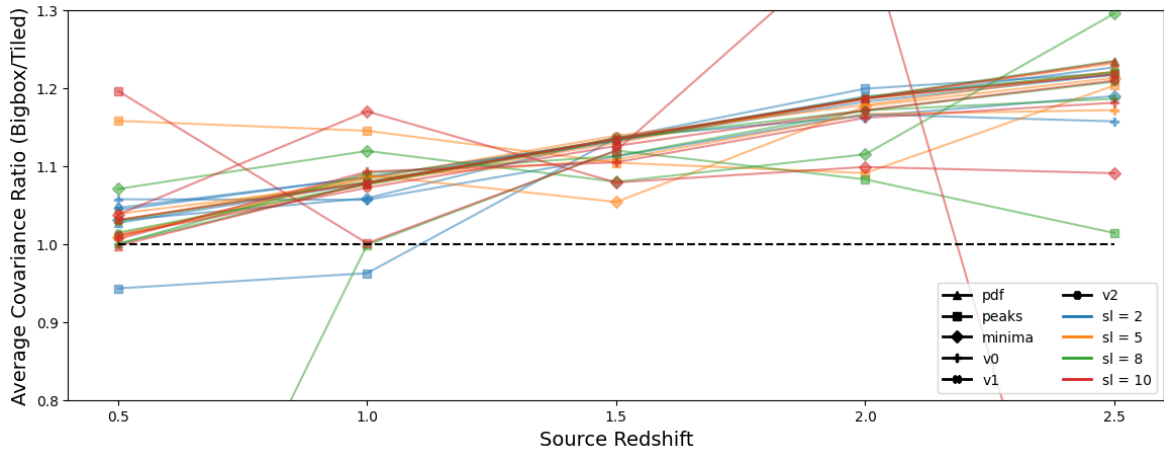


Figure 8.15: Average ratio of covariance matrices of statistical measures between the BIGBOX and TILED simulations for different smoothing scales. Larger smoothing scales lead to increased discrepancies in covariance estimates due to the loss of small-scale information.

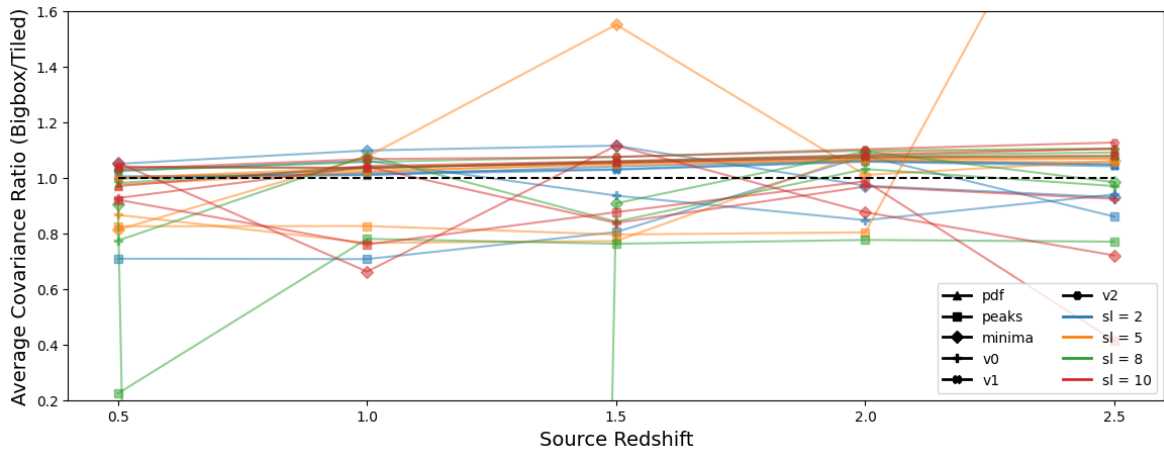


Figure 8.16: Same as Figure 8.15, but for the correlation matrices. The instability at larger smoothing scales reflects the challenges in capturing correlations at reduced resolutions.

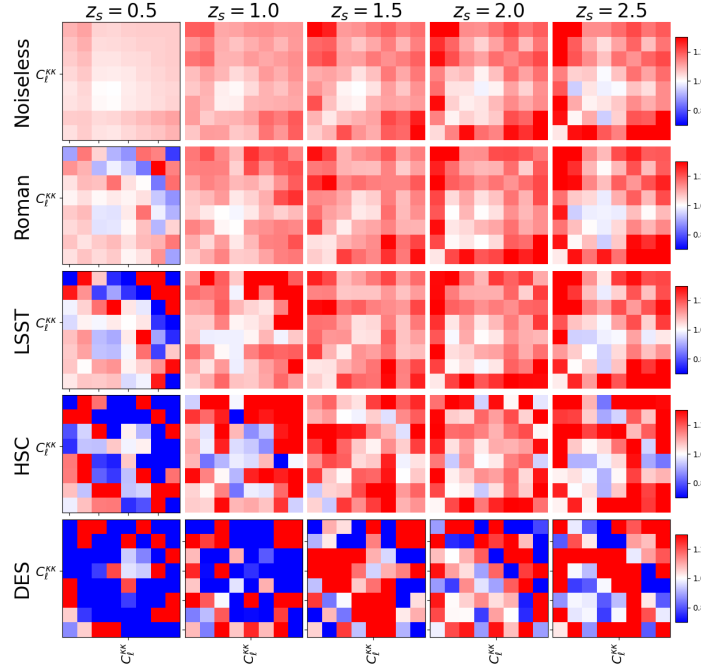


Figure 8.17: Ratio of covariance matrices of the angular power spectrum ($C_\ell^{\kappa\kappa}$) between the BIGBOX and TILED simulations for different shape noise levels (see Table 1.1). The sensitivity of the power spectrum to noise is evident from the fluctuating covariance ratios with higher noise levels.

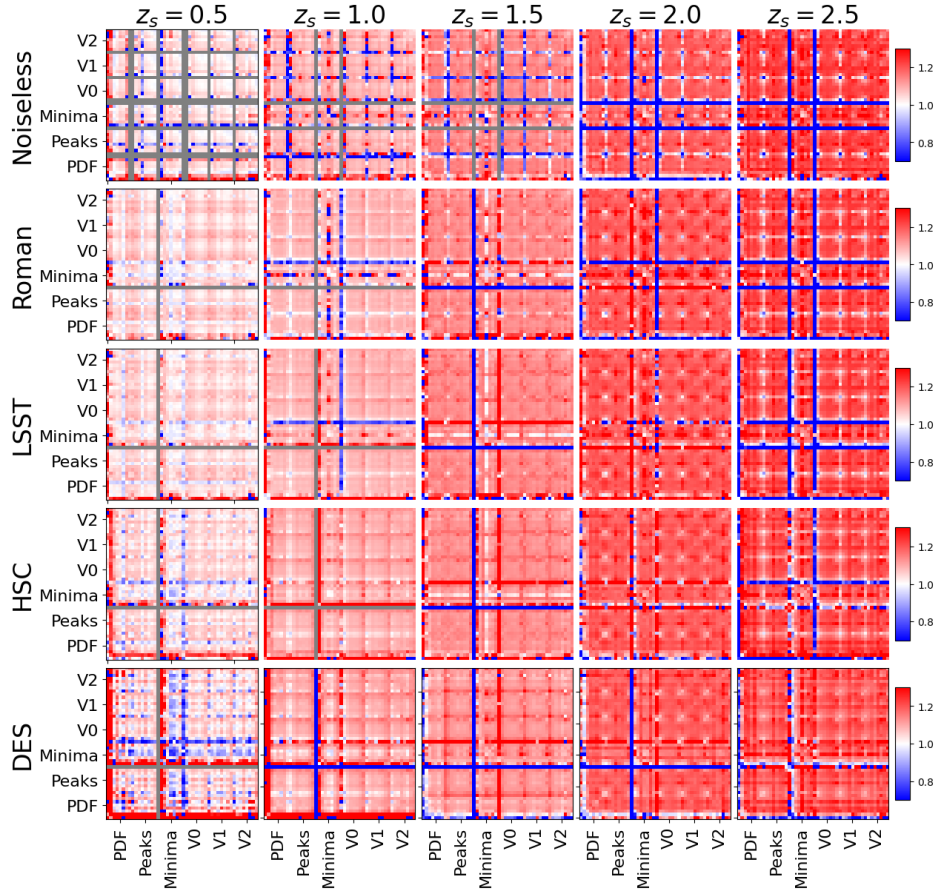


Figure 8.18: Same as Figure 8.17, but for the non-Gaussian statistical measures. The robustness of these measures against noise variations is reflected in the relatively stable covariance ratios.

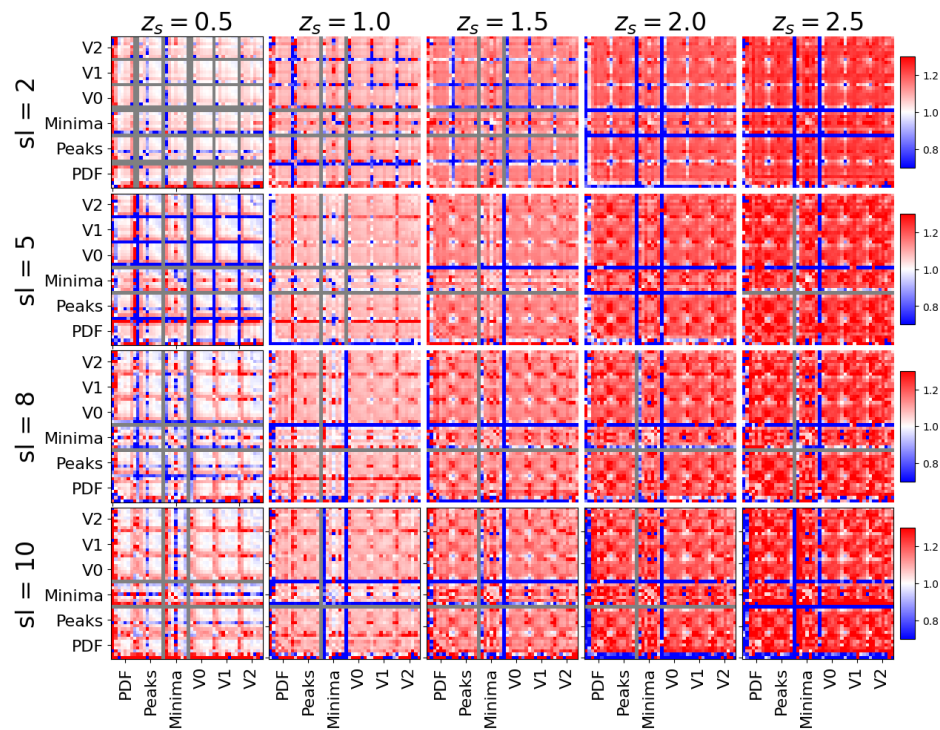


Figure 8.19: Same as Figure 8.18, but showing the impact of different smoothing scales on the covariance matrices of non-Gaussian statistical measures. The results emphasize how increased smoothing affects the detection and characterization of small-scale features.

Chapter 9

Discussion

Contents

9.1	Source of Systematics	90
9.2	flat-sky vs. full-sky	91

9.1 Source of Systematics

In this section, we will discuss the possible sources of systematics that could affect the covariance matrix.

9.1.1 Box Replication Effect

The box replication effect arises from replication of the simulation box in order to increase the volume of the simulation. In our setup, patches around special directions suffer the most from the box replication effect. To roughly assess the effect, we can compare the covariance matrices made from the patches of those directions and the rest of the patches.

Here, we defined the directions where are suspected to be affected by the box replication effect by the following criteria:

- data points around equator: $|\theta_i - \frac{\pi}{2}| \leq R_{\text{patch}}$
- data points around the edges of octant: $|\phi_i - \frac{k\pi}{2}| \leq R_{\text{patch}}$ for $k = 0, 1, 2, 3$

where (θ_i, ϕ_i) denotes the center of the patch i , and $R_{\text{patch}} = 5\sqrt{2} \text{ deg}$ is the half diagonal length of the patch.

We found that the patches including the point $(\theta_i, \phi_i) = (\pi/2, 0)$ have a significantly variated mean and variance, even compared to the rest of suspects. Therefore, we simply discarded this point as it will bias the result.

Finally, we obtain 70 patches from each realization, and 1400 patches for TILED simulations and 770 patches for BIGBOX simulations in total.

Figure 9.1 and Figure 9.2 show the average ratios of the covariance matrices and correlation matrices between BIGBOX and TILED simulations. Regardless the noisy behavior of bispectrum, the ratio are much closer to unity for the suspected patches. This implies that the box replication effect is significantly enhance the covariance matrix.

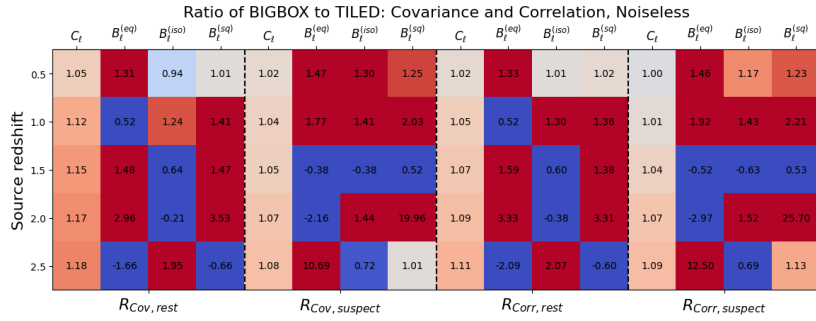


Figure 9.1: The ratios of covariance matrices and correlation matrices of power spectrum and bispectrum between the patches around special directions and the rest of the patches.

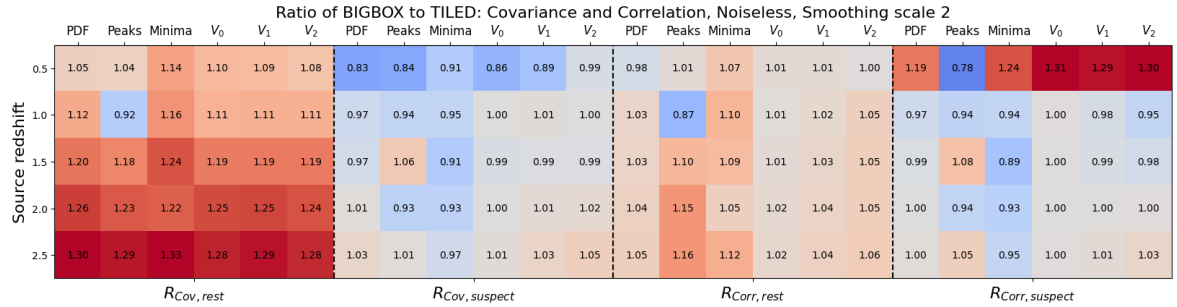


Figure 9.2: The same as Figure 9.1, but for PDF, peak/minima counts and Minkowski functionals. The box replication effect significantly enhances the covariance matrix.

Figure 9.3 and 9.4 show the comparison of the ratios of mean and variance of each Statistics. Clearly, the suspected patches have biased mean values. The variance ratios are closer to unity, which means that the variance of the suspected patches is larger than the rest of the patches.

9.2 flat-sky vs. full-sky

The flat-sky approximation is a good approximation for small patches on the sky. However, the flat-sky approximation breaks down for large patches. In this section, we conduct a test for angular power spectrum, PDF, and peak/minima counts to see how the flat-sky approximation affects the statistics.

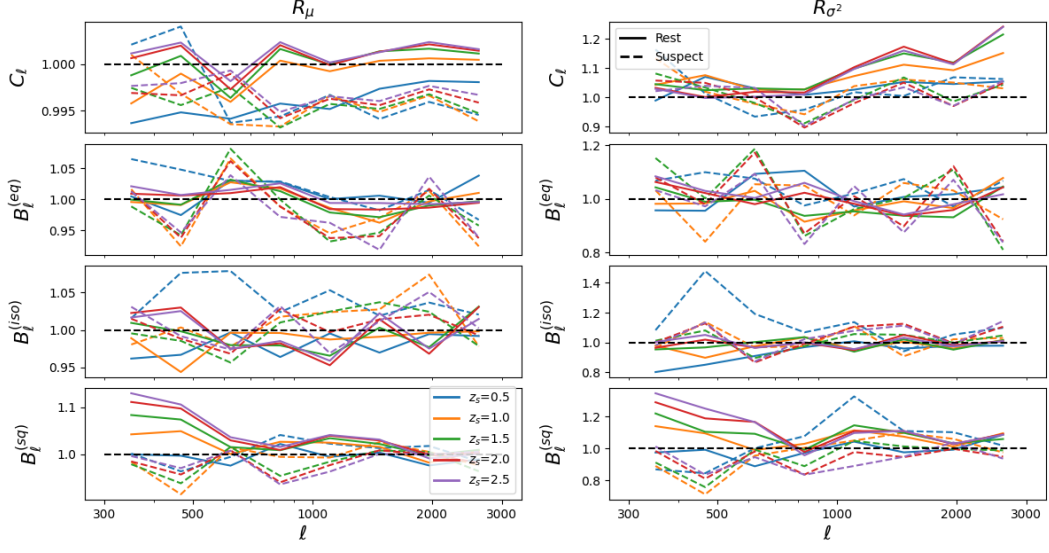


Figure 9.3: The ratios of mean and variance of power spectrum and bispectrum between the patches around special directions and the rest of the patches. The mean of suspected patches are biased and the variance is larger.

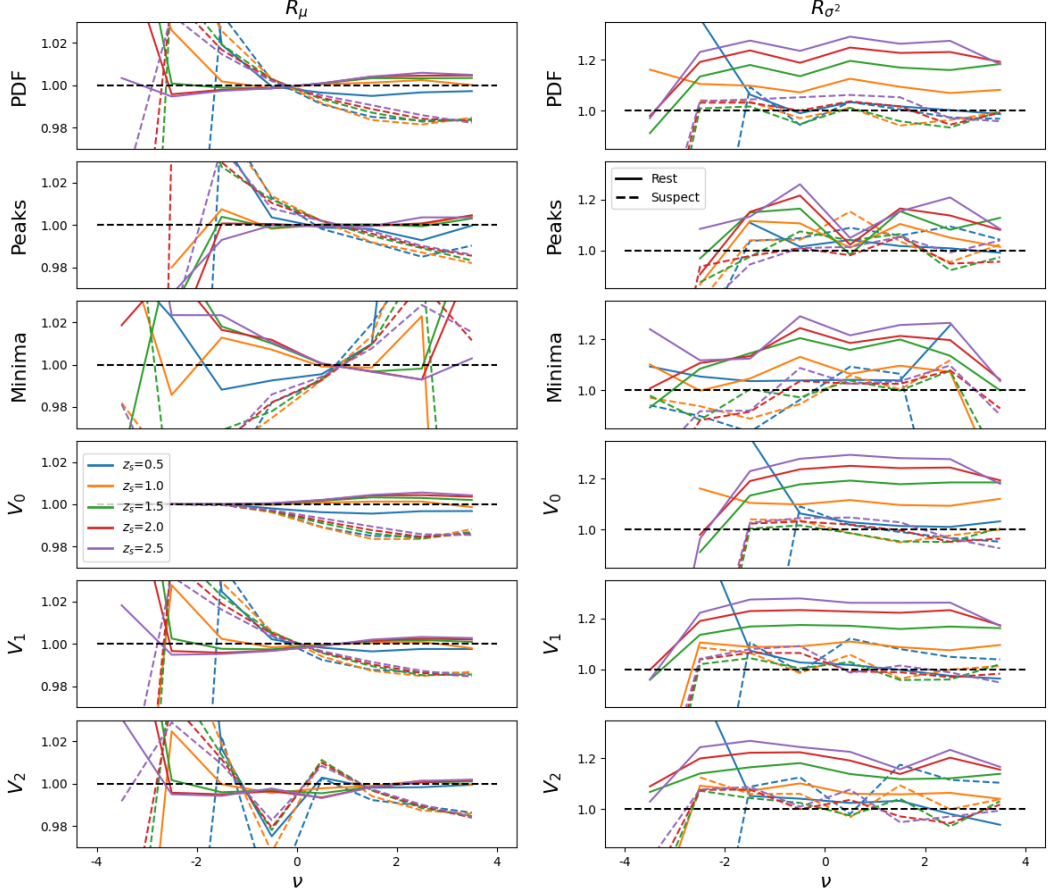


Figure 9.4: The same as Figure 9.3, but for PDF, peak/minima counts and Minkowski functionals. The suspected patches tend to have more extreme values and larger variance.

Chapter 10

Conclusions and Future Work

We conduct a high-resolved large-scale simulations study on the effect of super-sample effects on the covariance matrix of higher-order statistics. We compare two sets of simulations: BIGBOX simulation and TILED simulation. The BIGBOX simulations are simulations with large box size containing large-scale modes, while the TILED simulations are simulations with small box size replicated to cover the same volume of the BIGBOX simulations and without large-scale mode included. We compared the mean value, covariance matrices and correlation matrices of higher-order statistics: bispectrum, PDF, peak/minima counts and Minkowski Functionals. Additionally, we measure those statistics with different noise levels and smoothing scales. We then compare the results from the BIGBOX simulations and the TILED simulations to see how the super-sample effect affects the covariance matrix of higher-order statistics. Finally, we discuss the implications of the super-sample effect on the covariance matrix of higher-order statistics and how to mitigate the effect in the future analysis.

The main results of this study are:

- The super-sample effect affects the covariance matrix of higher-order statistics at the level of 10% to 20% in covariance matrix, and only few percent in correlation matrix. This means that the super-sample effect increases the overall correlation between different convergence values. Note that the box replication effect causes underestimation of the covariance matrix. Therefore, the value we found is the upper limit of the super-sample effect.
- The super-sample effect is universal for all higher-order statistics we tested and for all noise levels and smoothing scales. This means that the super-sample effect is not specific to any particular statistics or any particular noise level or smoothing scale.

For future work, we suggest the following:

Bibliography

- Abbott B. P., et al., 2016, [Phys. Rev. Lett.](#), **116**, 061102
- Abbott T. M. C., et al., 2018, [ApJS](#), **239**, 18
- Abbott T. M. C., et al., 2021, [ApJS](#), **255**, 20
- Abbott T. M. C., et al., 2022, [Phys. Rev. D](#), **105**, 023520
- Ahmad Q. R., et al., 2001, [Phys. Rev. Lett.](#), **87**, 071301
- Aihara H., et al., 2018, [PASJ](#), **70**, S4
- Albrecht A., et al., 2006, [arXiv e-prints](#), pp astro-ph/0609591
- Alpher R. A., Herman R., 1948, [Nature](#), **162**, 774
- Amon A., et al., 2022, [Phys. Rev. D](#), **105**, 023514
- Armijo J., Marques G. A., Novaes C. P., Thiele L., Cowell J. A., Grandón D., Shirasaki M., Liu J., 2024, [arXiv e-prints](#), p. arXiv:2410.00401
- Asgari M., et al., 2021, [A&A](#), **645**, A104
- Bardeen J. M., Bond J. R., Kaiser N., Szalay A. S., 1986, [ApJ](#), **304**, 15
- Barnes J., Hut P., 1986, [Nature](#), **324**, 446
- Barreira A., Schmidt F., 2017, [J. Cosmology Astropart. Phys.](#), **2017**, 051
- Barreira A., Krause E., Schmidt F., 2018, [J. Cosmology Astropart. Phys.](#), **2018**, 015
- Bartelmann M., 2010, [Classical and Quantum Gravity](#), **27**, 233001
- Bartelmann M., Schneider P., 2001, [Phys. Rep.](#), **340**, 291
- Bayer A. E., Liu J., Terasawa R., Barreira A., Zhong Y., Feng Y., 2023, [Phys. Rev. D](#), **108**, 043521
- Bayer A. E., Zhong Y., Li Z., DeRose J., Feng Y., Liu J., 2024, [arXiv e-prints](#), p. arXiv:2407.17462

- Bennett C. L., et al., 2003, [ApJS](#), **148**, 97
- Berger M. J., Colella P., 1989, [Journal of Computational Physics](#), **82**, 64
- Bernardeau F., Colombi S., Gaztañaga E., Scoccimarro R., 2002, [Phys. Rep.](#), **367**, 1
- Blas D., Lesgourges J., Tram T., 2011, [J. Cosmology Astropart. Phys.](#), **2011**, 034
- Bond J. R., Efstathiou G., 1987, [MNRAS](#), **226**, 655
- Born M., 1926, [Zeitschrift fur Physik](#), **38**, 803
- Boyle A., Uhlemann C., Friedrich O., Barthelemy A., Codis S., Bernardeau F., Giocoli C., Baldi M., 2021, [MNRAS](#), **505**, 2886
- Carroll S. M., Press W. H., Turner E. L., 1992, [ARA&A](#), **30**, 499
- Chan K. C., Moradinezhad Dizgah A., Noreña J., 2018, [Phys. Rev. D](#), **97**, 043532
- Chen Z., Yu Y., 2024, [MNRAS](#), **534**, 1205
- Cooley J. W., Tukey J. W., 1965, [Mathematics of Computation](#), **19**, 297
- Crocce M., Castander F. J., Gaztañaga E., Fosalba P., Carretero J., 2015, [MNRAS](#), **453**, 1513
- DESI Collaboration et al., 2016, [arXiv e-prints](#), p. arXiv:1611.00036
- Dalal R., et al., 2023, [Phys. Rev. D](#), **108**, 123519
- Das S., Bode P., 2008, [ApJ](#), **682**, 1
- Dawson K. S., et al., 2013, [AJ](#), **145**, 10
- DeRose J., et al., 2019, [ApJ](#), **875**, 69
- Di Valentino E., et al., 2021, [Classical and Quantum Gravity](#), **38**, 153001
- Dietrich J. P., Hartlap J., 2010, [MNRAS](#), **402**, 1049
- Dodelson S., 2003, [Modern Cosmology](#)
- Dodelson S., Zhang P., 2005, [Phys. Rev. D](#), **72**, 083001
- Dubinski J., 1996, [New Astronomy](#), **1**, 133
- Efstathiou G., Davis M., White S. D. M., Frenk C. S., 1985, [ApJS](#), **57**, 241
- Einasto J., 1965, [Trudy Astrofizicheskogo Instituta Alma-Ata](#), **5**, 87

Einstein A., 1915, Sitzungsberichte der Königlich Preussischen Akademie der Wissenschaften, pp 844–847

Eisenstein D. J., et al., 2005, [ApJ, 633, 560](#)

Euclid Collaboration et al., 2019, [A&A, 627, A59](#)

Euclid Collaboration et al., 2023, [A&A, 675, A120](#)

Euclid Collaboration et al., 2024, [arXiv e-prints, p. arXiv:2405.13495](#)

Falco E. E., Gorenstein M. V., Shapiro I. I., 1985, [ApJ, 289, L1](#)

Feldman H. A., Kaiser N., Peacock J. A., 1994, [ApJ, 426, 23](#)

Feng Y., Chu M.-Y., Seljak U., McDonald P., 2016, [MNRAS, 463, 2273](#)

Ferlito F., et al., 2023, [MNRAS, 524, 5591](#)

Flaugher B., et al., 2015, [AJ, 150, 150](#)

Fluri J., Kacprzak T., Sgier R., Refregier A., Amara A., 2018, [J. Cosmology Astropart. Phys., 2018, 051](#)

Fluri J., Kacprzak T., Lucchi A., Refregier A., Amara A., Hofmann T., Schneider A., 2019, [Phys. Rev. D, 100, 063514](#)

Fluri J., Kacprzak T., Lucchi A., Schneider A., Refregier A., Hofmann T., 2022, [Phys. Rev. D, 105, 083518](#)

Fosalba P., Crocce M., Gaztañaga E., Castander F. J., 2015, [MNRAS, 448, 2987](#)

Freedman W. L., et al., 2001, [ApJ, 553, 47](#)

Friedmann A., 1922, [Zeitschrift fur Physik, 10, 377](#)

Fu L., et al., 2014, [MNRAS, 441, 2725](#)

Fukuda Y., et al., 1998, [Phys. Rev. Lett., 81, 1562](#)

Gaia Collaboration et al., 2016, [A&A, 595, A2](#)

Gamow G., 1948, [Nature, 162, 680](#)

García-García C., Ruiz-Zapatero J., Alonso D., Bellini E., Ferreira P. G., Mueller E.-M., Nicola A., Ruiz-Lapuente P., 2021, [J. Cosmology Astropart. Phys., 2021, 030](#)

Gatti M., et al., 2020, [MNRAS, 498, 4060](#)

- Grewal N., Zuntz J., Tröster T., Amon A., 2022, *The Open Journal of Astrophysics*, **5**, 13
- Gunn J. E., Gott J. Richard I., 1972, *ApJ*, **176**, 1
- Guth A. H., 1981, *Phys. Rev. D*, **23**, 347
- Górski K. M., Hivon E., Banday A. J., Wandelt B. D., Hansen F. K., Reinecke M., Bartelmann M., 2005, *The Astrophysical Journal*, **622**, 759
- Hikage C., et al., 2019, *PASJ*, **71**, 43
- Hilbert S., Hartlap J., White S. D. M., Schneider P., 2009, *A&A*, **499**, 31
- Hockney R. W., Eastwood J. W., 1981, *Computer Simulation Using Particles*. CRC Press
- Hogg D. W., 1999, *arXiv e-prints*, pp astro-ph/9905116
- Hubble E. P., 1925, *The Observatory*, **48**, 139
- Hubble E. P., 1929, *ApJ*, **69**, 103
- Ivezić Ž., et al., 2019, *ApJ*, **873**, 111
- Jain B., Van Waerbeke L., 2000, *ApJ*, **530**, L1
- Jeans J. H., 1902, *Philosophical Transactions of the Royal Society of London Series A*, **199**, 1
- Kacprzak T., et al., 2016, *MNRAS*, **463**, 3653
- Kaiser N., Squires G., 1993, *ApJ*, **404**, 441
- Kilbinger M., 2015, *Reports on Progress in Physics*, **78**, 086901
- Kilbinger M., Schneider P., 2005, *A&A*, **442**, 69
- Kollmeier J., et al., 2019, in *Bulletin of the American Astronomical Society*. p. 274
- Kratochvil J. M., Lim E. A., Wang S., Haiman Z., May M., Huffenberger K., 2012, *Phys. Rev. D*, **85**, 103513
- LSST Dark Energy Science Collaboration 2012, *arXiv e-prints*, p. arXiv:1211.0310
- LSST Science Collaboration et al., 2009, *arXiv e-prints*, p. arXiv:0912.0201
- Lacasa F., Grain J., 2019, *A&A*, **624**, A61
- Lacasa F., Rosenfeld R., 2016, *J. Cosmology Astropart. Phys.*, **2016**, 005
- Lacasa F., Lima M., Aguena M., 2018, *A&A*, **611**, A83

Leclercq F., 2020, Evolution of cosmological simulations over the last 50 years, [http://
florent-leclercq.eu/blog.php?page=2](http://florent-leclercq.eu/blog.php?page=2)

Lemaître G., 1931, *MNRAS*, **91**, 483

Lewis A., Challinor A., Lasenby A., 2000, *ApJ*, **538**, 473

Li Y., Hu W., Takada M., 2014, *Phys. Rev. D*, **89**, 083519

Limber D. N., 1954, *ApJ*, **119**, 655

Linde A. D., 1982, *Physics Letters B*, **108**, 389

Linke L., Heydenreich S., Burger P. A., Schneider P., 2023, *A&A*, **672**, A185

Liu J., Bird S., Zorrilla Matilla J. M., Hill J. C., Haiman Z., Madhavacheril M. S., Petri A., Spergel D. N., 2018, *J. Cosmology Astropart. Phys.*, **2018**, 049

Mandelbaum R., 2018, *ARA&A*, **56**, 393

Mandelbaum R., Slosar A., Baldauf T., Seljak U., Hirata C. M., Nakajima R., Reyes R., Smith R. E., 2013, *MNRAS*, **432**, 1544

Marques G. A., Liu J., Zorrilla Matilla J. M., Haiman Z., Bernui A., Novaes C. P., 2019, *J. Cosmology
Astropart. Phys.*, **2019**, 019

Marques G. A., et al., 2024, *MNRAS*, **528**, 4513

Martinet N., et al., 2018, *MNRAS*, **474**, 712

Matsubara T., 2010, *Phys. Rev. D*, **81**, 083505

Maturi M., Angrick C., Pace F., Bartelmann M., 2010, *A&A*, **519**, A23

Miyazaki S., et al., 2018, *PASJ*, **70**, S1

Mo H. J., White S. D. M., 1996, *MNRAS*, **282**, 347

Navarro J. F., Frenk C. S., White S. D. M., 1996, *ApJ*, **462**, 563

Navarro J. F., Frenk C. S., White S. D. M., 1997, *ApJ*, **490**, 493

Nelson D., et al., 2019, *Computational Astrophysics and Cosmology*, **6**, 2

Oguri M., Hamana T., 2011, *MNRAS*, **414**, 1851

Omori Y., 2024, *MNRAS*, **530**, 5030

- Peebles P. J. E., 1968, [ApJ](#), **153**, 1
- Peebles P. J. E., Yu J. T., 1970, [ApJ](#), **162**, 815
- Penzias A. A., Wilson R. W., 1965, [ApJ](#), **142**, 419
- Perlmutter S., et al., 1999, [ApJ](#), **517**, 565
- Petri A., 2016, [Astronomy and Computing](#), **17**, 73
- Petri A., Liu J., Haiman Z., May M., Hui L., Kratochvil J. M., 2015, [Phys. Rev. D](#), **91**, 103511
- Planck Collaboration et al., 2014, [A&A](#), **571**, A15
- Planck Collaboration et al., 2016, [A&A](#), **594**, A13
- Planck Collaboration et al., 2020, [A&A](#), **641**, A6
- Powell J., Caudill L., Young O., 2023, [American Journal of Physics](#), **91**, 478
- Press W. H., Schechter P., 1974, [ApJ](#), **187**, 425
- Riess A. G., et al., 1998, [AJ](#), **116**, 1009
- Riess A. G., Casertano S., Yuan W., Macri L. M., Scolnic D., 2019, [ApJ](#), **876**, 85
- Riess A. G., et al., 2022, [ApJ](#), **934**, L7
- Rubin V. C., Ford W. Kent J., 1970, [ApJ](#), **159**, 379
- Rubin V. C., Ford W. K. J., Thonnard N., 1980, [ApJ](#), **238**, 471
- Schneider P., Seitz C., 1995, [A&A](#), **294**, 411
- Schneider P., Ehlers J., Falco E. E., 1992, Gravitational Lenses, doi:10.1007/978-3-662-03758-4.
- Scoccimarro R., Couchman H. M. P., Frieman J. A., 1999, [ApJ](#), **517**, 531
- Sehgal N., Bode P., Das S., Hernandez-Monteagudo C., Huffenberger K., Lin Y.-T., Ostriker J. P., Trac H., 2010, [ApJ](#), **709**, 920
- Sheth R. K., Tormen G., 1999, [MNRAS](#), **308**, 119
- Sheth R. K., Mo H. J., Tormen G., 2001, [MNRAS](#), **323**, 1
- Shirasaki M., Hamana T., Yoshida N., 2015, [MNRAS](#), **453**, 3043
- Shirasaki M., Hamana T., Takada M., Takahashi R., Miyatake H., 2019, [MNRAS](#), **486**, 52
- Smith R. E., et al., 2003, [MNRAS](#), **341**, 1311

- Smoot G. F., et al., 1992, [ApJ](#), **396**, L1
- Spergel D., et al., 2015, [arXiv e-prints](#), p. arXiv:1503.03757
- Stein G., Alvarez M. A., Bond J. R., van Engelen A., Battaglia N., 2020, [J. Cosmology Astropart. Phys.](#), **2020**, 012
- Sunyaev R. A., Zeldovich Y. B., 1970, [Ap&SS](#), **7**, 3
- Swinbank R., James Purser R., 2006, [Quarterly Journal of the Royal Meteorological Society](#), **132**, 1769
- Takada M., Hu W., 2013, [Phys. Rev. D](#), **87**, 123504
- Takada M., Jain B., 2004, [MNRAS](#), **348**, 897
- Takahashi R., Sato M., Nishimichi T., Taruya A., Oguri M., 2012, [ApJ](#), **761**, 152
- Takahashi R., Hamana T., Shirasaki M., Namikawa T., Nishimichi T., Osato K., Shiroyama K., 2017, [ApJ](#), **850**, 24
- Takahashi R., Nishimichi T., Namikawa T., Taruya A., Kayo I., Osato K., Kobayashi Y., Shirasaki M., 2020, [ApJ](#), **895**, 113
- Tegmark M., 1997, [Phys. Rev. Lett.](#), **79**, 3806
- Teyssier R., et al., 2009, [A&A](#), **497**, 335
- The Dark Energy Survey Collaboration 2005, [arXiv e-prints](#), pp astro-ph/0510346
- Thiele L., Hill J. C., Smith K. M., 2020, [Phys. Rev. D](#), **102**, 123545
- Thiele L., Marques G. A., Liu J., Shirasaki M., 2023, [arXiv e-prints](#), p. arXiv:2304.05928
- Uhlemann C., Friedrich O., Boyle A., Gough A., Barthelemy A., Bernardeau F., Codis S., 2023, [The Open Journal of Astrophysics](#), **6**, 1
- Valageas P., Nishimichi T., 2011, [A&A](#), **532**, A4
- Weinberg S., 1972, Gravitation and Cosmology: Principles and Applications of the General Theory of Relativity
- Weinberg S., 2008, Cosmology
- Wick G. C., 1950, [Phys. Rev.](#), **80**, 268
- Wu H.-Y., Weinberg D. H., Salcedo A. N., Wibking B. D., Zu Y., 2019, [MNRAS](#), **490**, 2606

Zel'dovich Y. B., 1970, A&A, [5, 84](#)

Zeldovich Y. B., Sunyaev R. A., 1969, [Ap&SS, 4, 301](#)

Zonca A., Singer L., Lenz D., Reinecke M., Rosset C., Hivon E., Gorski K., 2019, [Journal of Open Source Software, 4, 1298](#)

Zürcher D., Fluri J., Sgier R., Kacprzak T., Refregier A., 2021, [J. Cosmology Astropart. Phys., 2021, 028](#)

de Jong J. T. A., et al., 2013, The Messenger, [154, 44](#)